

Dynamic contrast-enhanced (DCE) imaging for tumor delineation in prostate cancer

Cover design and layout: Jan Korporaal
Print: Drukkerij Wilco BV, Amersfoort, the Netherlands
ISBN: 978-90-393-5597-8
Copyright: Chapter 3 - Wiley-Liss, Inc. 2011
Chapter 4 - Radiological Society of North America 2010
Chapter 5 - Lippincott Williams & Wilkins, Inc. 2011
Chapter 6 - Elsevier Ireland Ltd. 2009

The research described in this thesis was carried out at the Department of Radiotherapy, University Medical Center Utrecht, Utrecht, the Netherlands.

Dynamic contrast-enhanced (DCE) imaging for tumor delineation in prostate cancer

**Dynamische contrastmiddel-versterkte (DCE) beeldvorming
voor tumorintekening bij prostaatkanker**

(met een samenvatting in het Nederlands)

**Dynamische kontrastmittelgestützte (DCE) Bildgebung
zur Tumoreinzeichnung des Prostatakarzinoms**

(mit einer Zusammenfassung in deutscher Sprache)

Proefschrift

ter verkrijging van de graad van doctor aan de Universiteit Utrecht
op gezag van de rector magnificus, prof. dr. G.J. van der Zwaan,
ingevolge het besluit van het college voor promoties
in het openbaar te verdedigen op

donderdag 8 september 2011 des middags te 12.45 uur

door

Johannes Georg Korporaal

geboren op 11 oktober 1982 te Ede

Promotor: Prof. dr. ir. J.J.W. Lagendijk

Co-promotoren: Dr. U.A. van der Heide
Dr. M. van Vulpen

The project was financially supported by the Dutch Cancer Society (grant UU2007-3893).

Financial support for publication of this thesis was kindly provided by Philips Healthcare, Elekta B.V., Nucletron B.V., Bayer B.V. HealthCare and Röntgen Stichting Utrecht.

Für meinen Großvater,

*der mir die Liebe zur Natur beigebracht und
mein Interesse für die Wissenschaft geweckt hat.*

Contents

Chapter 1 **11**

General introduction

1.1	Prostate cancer	12
1.2	Radiation therapy	12
1.3	Multi-parametric imaging for prostate cancer	13
1.4	Dynamic contrast-enhanced (DCE) imaging	14
1.5	DCE-MRI versus DCE-CT	14
1.6	Outline of the thesis	16

Chapter 2 **19**

Uncertainties in the arterial input function (AIF) in dynamic contrast-enhanced (DCE) imaging of the pelvis: when to use a population-averaged or an exam-specific AIF?

	Abstract	19
2.1	Introduction	20
2.2	Materials and methods	21
2.3	Results	25
2.4	Discussion	27
2.5	Supplement 1 Population-averaged AIF	30

Chapter 3 **35**

Phase-based arterial input function (AIF) measurements in the femoral arteries for quantification of dynamic contrast-enhanced (DCE) MRI and comparison with DCE-CT

	Abstract	35
3.1	Introduction	36
3.2	Materials and methods	37
3.3	Results	41
3.4	Discussion	45

Chapter 4 **49**

Dynamic contrast-enhanced CT for prostate cancer: the relation between image noise, voxel size and repeatability

	Abstract	49
4.1	Introduction	50
4.2	Materials and methods	50
4.3	Results	54
4.4	Discussion	58

Chapter 5 **63**

Tracer kinetic model selection for dynamic contrast-enhanced CT imaging of prostate cancer

	Abstract	63
5.1	Introduction	64
5.2	Materials and methods	65
5.3	Results	69
5.4	Discussion	73

Chapter 6 **77**

The use of probability maps to deal with the uncertainties in prostate cancer delineation

	Abstract	77
6.1	Introduction	78
6.2	Materials and methods	78
6.3	Results	81
6.4	Discussion	83

Chapter 7 **87**

General discussion

	The importance of the arterial input function (AIF)	88
7.1	Choices in tracer kinetic model (TKM) analysis	90
7.2	Image-guided radiation therapy	91
7.3	CT versus MRI	91
7.4	Future perspectives	93
7.5		

Chapter 8 **95**
References

Chapter 9 **107**
Summary - Samenvatting - Zusammenfassung

9.1	Summary	108
9.2	Samenvatting	110
9.3	Zusammenfassung	112

Chapter 10 **115**

List of publications

10.1	Scientific articles	116
10.2	Proceedings and abstracts	117

Chapter 11 **119**
Dankwoord

Chapter 12 **123**
Curriculum vitae

1

Chapter 1

General introduction

1.1 Prostate cancer

The prostate gland is part of the male reproductive system and is located just underneath the bladder. It excretes prostatic fluid, which is one of the three elements of the semen. With ageing, benign or malignant changes may occur in the prostate tissue. Prostate cancer is such a malignant disease and the most frequently detected cancer type in men [1, 2]. In the USA and in the Netherlands, prostate cancer accounts for respectively 27.6% and 20.7% of all newly detected cancer cases in men [1, 2]. It can be considered an “old-men’s disease”, with about 70% of the prostate cancer patients being 65 years or older [3].

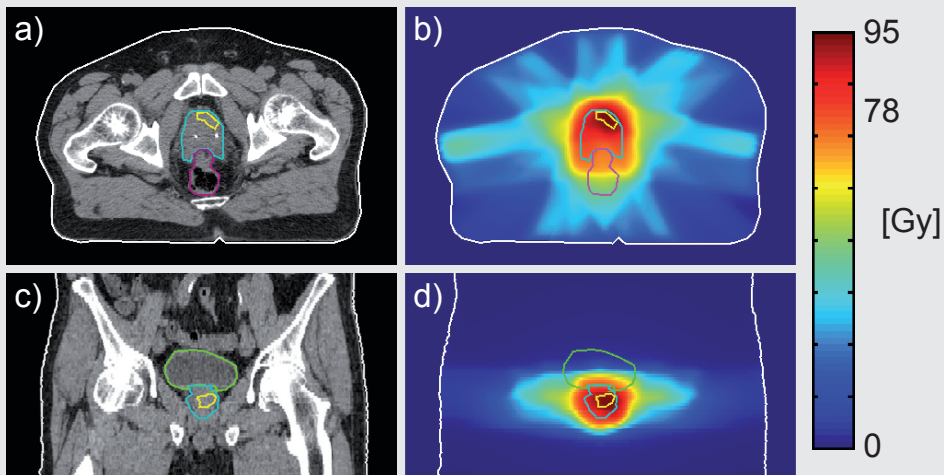
1.2 Radiation therapy

If a prostate cancer patient is eligible for curative treatment, radiation therapy is one of the main treatment options. It can be subdivided in two forms: external beam radiation therapy (EBRT) and brachytherapy. With brachytherapy, a number of radioactive seeds are temporarily or permanently placed in the prostate. In this way, the tumor is irradiated from inside the patient. Brachytherapy is predominantly performed in patients with small tumors that did not grow outside the prostate.

EBRT is the only treatment option for patients with a bad physical condition, a large tumor or a tumor that has spread outside the prostate. With EBRT, a patient is placed on a treatment table and radiation is delivered to the prostate through the skin, with a number of radiation beams that are generated by a linear accelerator. Intensity modulated radiation therapy (IMRT) is an advanced form of EBRT, which gives the least possible radiation dose to the healthy surrounding tissues, while maintaining a good dose coverage in the prostate [4].

Although the tumor is mostly limited to a part of the prostate, traditionally the entire prostate is regarded as the gross tumor volume (GTV) [5-7]. The clinical target volume (CTV) is the volume that has to be irradiated and is often taken equal to the GTV, possibly with a small additional margin. A number of randomized trials have shown that these IMRT treatments with homogeneous doses of about 78 Gy are not sufficient to obtain full tumor control [8-10]. In addition, a tumor often recurs at the original location of the primary tumor [11, 12]. So, there is a need for increasing the dose to the tumor, to obtain better tumor control. However, further increasing the dose to the entire prostate is limited by the dose constraints of the surrounding organs at risk (OAR).

With focal therapies, like dose escalation with a micro-boost [13-16], a higher radiation dose can be given to the tumor, while keeping the doses to the OAR within the dose constraints (Figure 1.1). At the UMC Utrecht, in 2010 a multicenter randomized phase-III trial has started to investigate whether this strategy with an additional micro-boost to the tumor of up to 95 Gy will result in an improved biochemical control five years after treatment [17]. For this purpose, imaging of the tumor within the prostate becomes important, since the size and location of the tumor within the prostate should be known for planning of the micro-boost.

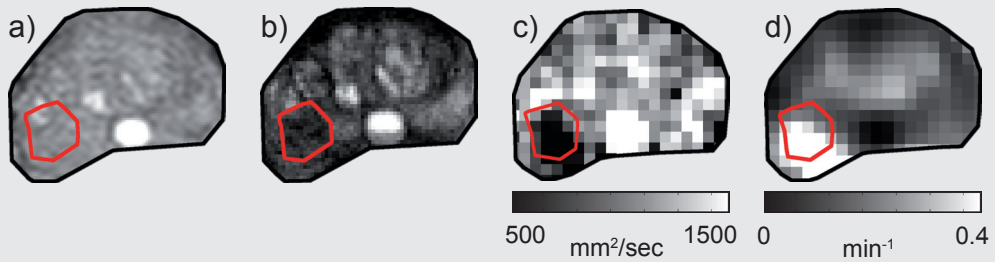
Figure 1.1

Example of a CT scan (a,c) and an IMRT dose plan with micro-boost (b,d) of a 73-year old prostate cancer patient (T3a). The micro-boost is given to the GTV (yellow) inside the prostate (blue), with the bladder (green) and rectum (purple) as nearby OAR.

1.3 Multi-parametric imaging for prostate cancer

The prostate can be imaged with a number of imaging modalities, like magnetic resonance imaging (MRI), computed tomography (CT) and ultrasound [18]. All these modalities can give anatomical and functional information, which are both needed for the planning of an IMRT treatment with a micro-boost. With a CT scan, the patient contour and the anatomy of the soft tissues and bony structures are obtained and commonly used for the optimization of the dose calculation of the IMRT radiation beams. However, the soft tissue contrast on CT is moderate. So, MRI is the preferred modality to delineate the prostate and nearby organs like the rectum and bladder [19]. Subsequently, these delineations can be coregistered with the CT scan to facilitate radiation treatment planning.

When it comes to distinguishing between healthy and cancerous prostate tissue, not only anatomical but also functional information is needed, reflecting the underlying physiology and tissue characteristics. In this respect, MRI is the most flexible imaging modality, offering a wide range of image contrast mechanisms (Figure 1.2). For example, on a T_2 -weighted MR scan, tumor tissue appears as hypointense regions [20, 21] and the cell density of the prostate tissue can be assessed with a diffusion weighted (DWI) scan [22-24]. Furthermore, a dynamic contrast-enhanced (DCE) exam gives information about the microvascular status of the prostate [25-27], whereas MR spectroscopy (MRS) is valuable for determination of the chemical composition of the prostate [28, 29]. The combination of all these different MR contrast is called multi-parametric imaging and is becoming the standard for tumor detection in the prostate [30]. This thesis focuses on one of these techniques, specifically the DCE imaging technique.

Figure 1.2

Transverse views of the prostate, showing different MR contrasts in a 67-year old prostate cancer patient (T_3a). The high-resolution balanced turbo field echo (bTFE) sequence (a) is used to delineate the outer contour of the prostate. The tumor (red) is visible as a hypointense region in the T_2 -weighted scan (b). In the diffusion weighted image (c) the ADC values are decreased in the tumor and in the DCE exam, the tumor shows up with increased K^{trans} values (d).

1.4 Dynamic contrast-enhanced (DCE) imaging

The formation of new blood vessels or neovascularization is one of the physiological processes that is characteristic for tumor growth [31, 32]. Tumor cells initiate the formation of this new vasculature from pre-existing vessels, often resulting in an irregular vascular bed of leaky vessels. With dynamic contrast-enhanced (DCE) imaging, these abnormalities in tissue perfusion can be measured.

After intravenous administration of a contrast agent, the prostate is imaged sequentially during a certain time period, typically between 2 and 5 minutes. After traversing the lungs and the heart, the contrast agent will reach the prostate tissue and leak out from the small capillaries into the extravascular extracellular space (EES) (Figure 1.3). This extravasation and accumulation of contrast agent in the prostate will lead to a signal enhancement in the images.

The contrast agent will show different leakage behavior in healthy and cancerous prostate tissue, depending on the number of vessels and the permeability of the vessels. These differences in physiology are reflected by differences in the time-enhancement curves in the voxels of the prostate tissue. By relating these time-enhancement curves to the contrast bolus passage in a nearby artery, called the arterial input function (AIF), an estimate of the blood flow and vessel permeability can be obtained [25, 26]. This quantification process is generally performed with tracer kinetic models (TKMs), which treat the time-enhancement curves of the prostate as the impulse response of the prostate tissue to the AIF.

1.5 DCE-MRI versus DCE-CT

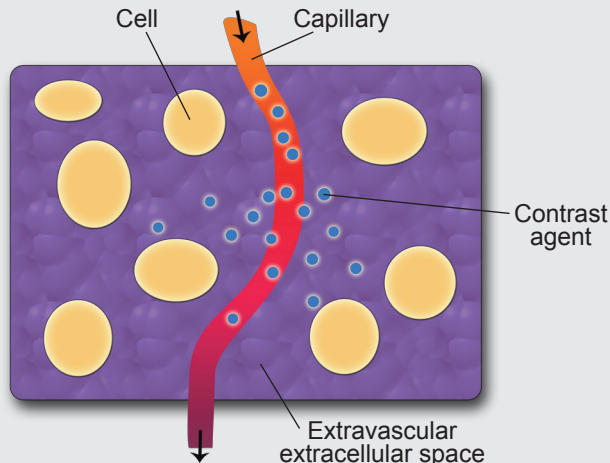
Magnetic resonance imaging (MRI) is a suited imaging technique to perform DCE measurements of the prostate. It has a high spatial and temporal resolution, which are both required for reliable DCE measurements. Therefore, DCE-MRI can be used for treatment monitoring and follow-up, since no radiation is involved with MRI

exams. However, artifacts may be present during the data acquisition, making the quantification of DCE-MRI exams challenging. For example, signal saturation [33], inflow artifacts [34-36] and B_1 -field inhomogeneities [34, 37] hinder the measurement of a reliable AIF from the magnitude signal. In addition, the effect of the paramagnetic contrast agent on the surrounding water molecules is measured, rather than the concentration of the contrast agent itself [38-40]. This may introduce bias and uncertainties in the TKM parameters that reflect the physiological tissue properties.

In contrast, DCE-CT exams do not suffer from these MR artifacts and a linear relationship exists between the contrast agent concentration and the enhancement. However, DCE-CT exams suffer from a lower signal-to-noise ratio (SNR) in the prostate tissue compared to DCE-MRI, and a considerable amount of radiation dose is involved with DCE-CT exams. Although modern multi-slice CT scanners have a number of dose reduction techniques, the amount of the radiation dose does not justify wide-spread diagnostic imaging, treatment monitoring and follow-up measurements with DCE-CT. All patients that participated in the DCE-CT studies described in this thesis were imaged prior to an IMRT treatment of at least 77 Gy to the entire prostate. In these patients the radiation dose of the DCE-CT exams is negligible compared to the dose delivered in the subsequent radiation therapy treatment that resulted in a skin dose of up to 10 Gy.

Because of the aforementioned artifacts that may obscure reliable and robust DCE-MRI measurements, we turn to DCE-CT to be able to discriminate between DCE-MR artifacts and physiological processes.

Figure 1.3



Schematic overview of the underlying physiology in a voxel (purple). After injection, the contrast agent is delivered to the prostate tissue via the blood vessels. Depending on the vessel permeability and the blood flow, a certain amount of contrast agent leaks out of the capillaries into the extravascular extracellular space (EES). The contrast agent cannot enter the cells and will accumulate in and wash out from the EES.

1.6 Outline of the thesis

Chapter 2 deals with the use of a population-averaged AIF instead of an exam-specific AIF for DCE-MRI exams. For a well-founded choice between the two, on the one hand information is required about the inter- and intra-patient variations that are neglected with the use of a population-averaged AIF. On the other hand, the reliability of measuring an exam-specific AIF must be established. We used the data from a DCE-CT repeatability study (Chapter 4), to assess the variations in the AIF between patients, between exams, between the left and right femoral arteries and between slices.

As an alternative to the magnitude signal, the AIF can also be measured from the DCE-MRI phase signal (AIF_{PHASE}). Although some phantom and simulation studies have been performed by others, validation of AIF_{PHASE} measurements in humans is lacking. In chapter 3, we compared AIF_{PHASE} measurements with the AIF as measured on CT (AIF_{CT}) and calculated the corresponding K^{trans} maps in 12 prostate cancer patients to assess additionally the interchangeability of DCE-MRI and DCE-CT exams.

For reliable identification of small lesions within the prostate, it is crucial that they are consistently detected when the examination and analysis are repeated. The smallest detectable lesion size, however, depends on the spatial resolution. Therefore, we evaluated in Chapter 4 the relationship between image noise, voxel size, and voxel-wise repeatability of a DCE-CT examination for prostate cancer. In this way, an estimate of the daily variations in prostate perfusion within single patients was obtained.

A number of different TKMs, with varying degrees of complexity, have been used to quantify the vascular properties of the prostate. The three most commonly used TKMs for quantification of DCE data from the prostate are the Tofts, extended Tofts, and adiabatic approximation to the tissue homogeneity (AATH) model. In chapter 5, we investigated which of these three TKMs is the optimal model for quantification of DCE-CT data, under what conditions and how large the differences are. The best model was determined for each voxel, based on the corrected Akaike's Information Criterion, taking into account both the goodness-of-fit and the number of model parameters.

Chapter 6 deals with the clinical application of DCE exams, namely the radiation treatment planning of a micro-boost. Delineating a prostate tumor essentially comes down to a voxelwise decision whether a voxel contains tumor or not. There are however two problems that make an accurate tumor delineation difficult. First, the sensitivity and specificity of the DCE technique are not perfect. Second, by definition no detailed spatial verification of imaging with pathology can be obtained from patients scheduled for radiation therapy. In the clinical practice of radiation therapy treatment planning this means that there will never be a ground truth when delineating a prostate tumor. We propose a method to incorporate the uncertainty that a voxel contains tumor into the tumor delineation process.

A general discussion and future perspectives on the use of DCE-MRI and DCE-CT exams for tumor delineation in prostate cancer are finally presented in Chapter 7.

2

Chapter 2

Uncertainties in the arterial input function (AIF) in dynamic contrast-enhanced (DCE) imaging of the pelvis: when to use a population-averaged or an exam-specific AIF?

Abstract

For the quantification of dynamic contrast-enhanced (DCE) data with a tracer kinetic model, an arterial input function (AIF) is required. For a well-founded choice between an exam-specific AIF or a population-averaged AIF, on the one hand information is required about the inter- and intra-patient variations that are neglected when using a population-averaged AIF. On the other hand, the reliability of measuring an exam-specific AIF must be established. We performed a DCE-CT repeatability study in 28 prostate cancer patients, to assess the physiological variations in the AIF between patients, between exams, between the left and right femoral arteries and between slices. Furthermore, tracer kinetic model parameters were calculated with an exam-specific and a population-averaged AIF and the percentage errors in the transfer constant (K^{trans}) in the prostate were calculated. Inter- and intra-patient variations in AIF characteristics range from 9.5–15.1%, whereas the intra-exam variations between the left and right femoral arteries range from 1.6–6.8%. In prostate, the use of a population-averaged AIF causes a median difference in K^{trans} of 12.8% compared to the use of an exam-specific AIF. Thus, the use of a population-averaged AIF is advantageous when the measurement precision of an exam-specific AIF is considerably worse than 15%.

A version of this chapter has been submitted to Physics in Medicine and Biology as:

Uncertainties in the arterial input function (AIF) in dynamic contrast-enhanced (DCE) imaging of the pelvis: when to use a population-averaged or an exam-specific AIF?

J.G. Korporaal, C.A.T. van den Berg, M.J.P. van Osch, M. van Vulpen, and U.A. van der Heide

2.1 Introduction

The dynamic contrast-enhanced (DCE) imaging methodology gives information about the blood flow and vessel permeability in an organ of interest and is used with both CT and MRI as imaging modalities. In DCE-MRI exams of the prostate, large differences have been reported in the parameter range of transfer constant K^{trans} in healthy (0.06-0.60 min^{-1}) and cancerous (0.47-1.26 min^{-1}) prostate tissue [29, 41-43]. Differences in methodology between institutions and quantification problems inherent to the acquisition contribute to this inconsistency in K^{trans} values. This makes it difficult to perform multicenter studies and to compare DCE-MRI findings between studies. For other imaging techniques, e.g. diffusion weighted MR imaging (DWI), researchers have proposed a consensus approach to address this issue [44]. Although in particular the Tofts model has contributed to the agreement about nomenclature and definitions in tracer kinetic modeling [25], there is still insufficient consensus about the standardization of DCE-MRI imaging protocols.

One of the major problems in both acquisition and analysis of DCE-MRI data is the accurate measurement of an arterial input function (AIF), which is needed for absolute quantification [25, 45]. For organs in the pelvis like the prostate, rectum and cervix, the AIF is typically measured in the femoral arteries. Measuring an AIF with DCE-MRI can be challenging, due to a non-linear relationship between the signal and the contrast agent concentration [46] and artifacts like T_2^* -effects at higher concentrations [33, 47], B_1 -field inhomogeneities [34, 37] and inflow effects [34-36].

To avoid these problems, the use of a population-averaged AIF has been proposed [48, 49]. However, contradictory recommendations have been reported, with some studies in favor of a population-averaged AIF [49-53] and others in favor of an exam-specific AIF [48, 54-56]. To circumvent the problem of explicitly finding an AIF, reference signals can be used from which an AIF can be inferred [57, 58]. However, these methods rely on quite specific assumptions about the reference signals.

In this study, we investigate when a population-averaged or an exam-specific arterial input function (AIF) should be used. For a well-founded choice between the two, on the one hand information is required about the inter- and intra-patient variations that are neglected with the use of a population-averaged AIF. On the other hand, the reliability of measuring an exam-specific AIF must be established. As the choice for an AIF will influence the tracer kinetic model parameters, we also investigated the effects of AIF choice on K^{trans} values in the cancerous prostate.

Because of the challenges described above, DCE-MRI is not the most suitable technique to study the physiological variations in the AIF. Assuming that the time characteristics of the concentration changes in the femoral arteries are independent of the particular small molecular tracer used, we can turn to DCE-CT for this purpose. For CT, a linear relation exists between the contrast agent concentration and the signal enhancement in Hounsfield units (H.U.). Therefore we used DCE-CT, to obtain information about physiological variations in the AIF in the femoral arteries without

substantial measurement artifacts that may obscure the underlying processes. The aim of this study was to identify when a population-averaged or an exam-specific arterial input function (AIF) should be used in dynamic contrast-enhanced (DCE) imaging of the pelvis.

2.2 Materials and methods

Patients

The prospective study was approved by the local medical ethical research board and all patients gave written informed consent. We analyzed the AIFs from a previously published DCE-CT repeatability study for prostate cancer [59]. In that study, the repeatability of tracer kinetic model parameters was investigated as a function of image resolution. In brief, thirty patients with biopsy proven prostate cancer (T1c-T4, G1-3, Nx/o, Mx/o) underwent two DCE-CT exams on two different days within one week prior to radiotherapy. Only patients that did not have a contraindication for the CT contrast agent or fiducial markers in the prostate were included in this study. The intra-patient variations could not be established for one patient due to technical failure of the CT scanner during one of the imaging sessions. One further patient was excluded from the analysis because of a medical history with severe cardiac dysrhythmia, atrial fibrillation and coronary artery disease. The remaining 28 patients had a mean age of 69.0 (range 56–80) years, a mean body weight of 81.1 (range 59–107) kg, a mean Gleason score of 7 (range 6–9), and a mean pretreatment prostate-specific antigen level of 15.8 (range 4.3–59.0) ng/mL.

Imaging protocol

DCE-CT imaging was performed on a 64-slice CT scanner (Philips Brilliance, 120kV, 200mAs, reconstruction with moderately smoothing filter B, reconstructed to 32 slices, voxel size 0.68 x 0.68 x 1.25 mm). The imaged volume of 4 cm thickness was at the level of the prostate, thereby including the femoral arteries within the field of view. In each patient 60 ml iopromide (ULTRAVIST 300, Schering AG, Berlin, Germany) was injected with a power injector (6 ml/s), followed by a saline flush (40 ml, 6 ml/s). An exam consisted of acquisitions at 42 time points within a time window of 5 minutes. The first 24 acquisitions were taken at 2.4 s intervals, the next 12 at a 10 s interval and the last 6 at 20 s intervals. The increase in time interval was done to reduce the radiation burden after the first minute.

The effective biological dose was 1.3 mSv per time point, resulting in a total dose of about 54.6 mSv per exam. While this is a high dose for a diagnostic exam, it is negligible compared to the dose delivered in the subsequent radiation therapy treatment. A treatment dose of 77 Gy was given in the prostate with the intensity-modulated (IMRT) technique, which results in a skin dose of about 10 Gy.

AIF measurement

To remove motion artifacts within a DCE-CT exam, a local soft tissue registration was performed on the femoral arteries using a rigid image registration algorithm [60]. The AIF was determined per slice within a mask around the femoral arteries, taking

only the voxels with the 30% highest enhancement into account. To correct for hematocrit in the tracer kinetic modeling, each AIF was multiplied by a factor of 1.18, based on a hematocrit of 0.38 and a small to large vessel ratio of 0.7 [45, 61]. The AIF in an entire artery was defined as the average of all slices. The exam-specific AIF was defined as the average of the AIF for the left and right femoral artery. A population-averaged AIF was generated from the AIFs of the first DCE-CT exams of the entire patient group.

For each AIF the peak height, full width at half maximum (FWHM), area under the curve (AUC) of the first pass peak (AUC_{FPP}) and signal intensity 180 seconds after the peak (SI_{180}) were calculated.

To assess the contribution of image noise to the intra-exam variations, we calculated the noise level in each slice, each artery and each exam. This was done by dividing the single voxel noise level of 33.5 H.U. [59] by the square root of the number of voxels in which the AIF was measured [62]. We compared the noise levels with the observed variations in SI_{180} , because 180 seconds after the peak the AIF signal is very stable and sampling errors do not play a role.

The calculation of a CT-based population-averaged AIF, including all inter- and intra-patient uncertainties, is of potential interest for the quantification of DCE-MRI exams with similar injection times. We therefore converted our population-averaged AIF from H.U. to the modality-independent unit mM/mmol, as described earlier [63]. If we consider that the CT and MR contrast agents both have a low molecular weight (< 1 kDa), we can assume that the time characteristics of the concentration changes in the femoral arteries are independent of the particular small molecular tracer used. Since the height (mM) of an AIF is proportional to the amount (mmole) of contrast agent injected [64-66], we obtain a single modality-independent and dose normalized unit (mM/mmmole) by dividing the concentration of an AIF by the amount of contrast agent injected. For the conversion from H.U. to mM we used a conversion factor of 10.799 H.U. per mM [63].

ROI analysis

We evaluated the errors in the K^{trans} values in the prostate caused by a population-averaged AIF, because this model parameter is most useful for tumor detection in the prostate [27, 29, 41, 42]. We performed a region of interest (ROI) analysis based on the same delineations as in the previously published DCE-CT repeatability study for prostate cancer [59]. In short, on a T_2 -weighted MR scan hypointense regions suspected of tumor tissue (ROI_{susp}) were delineated in the peripheral zone (PZ) with the aid of all available clinical information including biopsy results. Furthermore, in each patient a ROI was delineated in a contralateral PZ region that was not suspected of disease. Each ROI was co-registered to the corresponding DCE-CT exam, and a mean enhancement curve was calculated from the first DCE-CT exam of the repeatability study. Tracer kinetic model parameters were calculated with both the exam-specific and population-averaged AIF, by using the Tofts model with blood

plasma component, as described in more detail earlier [59]. In the fitting algorithm possible differences in the contrast agent arrival time between the exam-specific and population-averaged AIF were corrected.

Statistical analysis

All statistical analyses were performed with Matlab (The MathWorks, Inc., 2008, version 7.7.0.471, Natick, MA, USA). Results were considered statistically significant at $p < 0.05$.

We tested for differences in AIF characteristics between the two exams with a paired Student's t-test, to ascertain that there was no bias between both exams. We calculated the inter-patient variations from the first DCE-CT exam of each patient, resulting in a mean, standard deviation (SD) and coefficient of variation (CV) for each AIF characteristic.

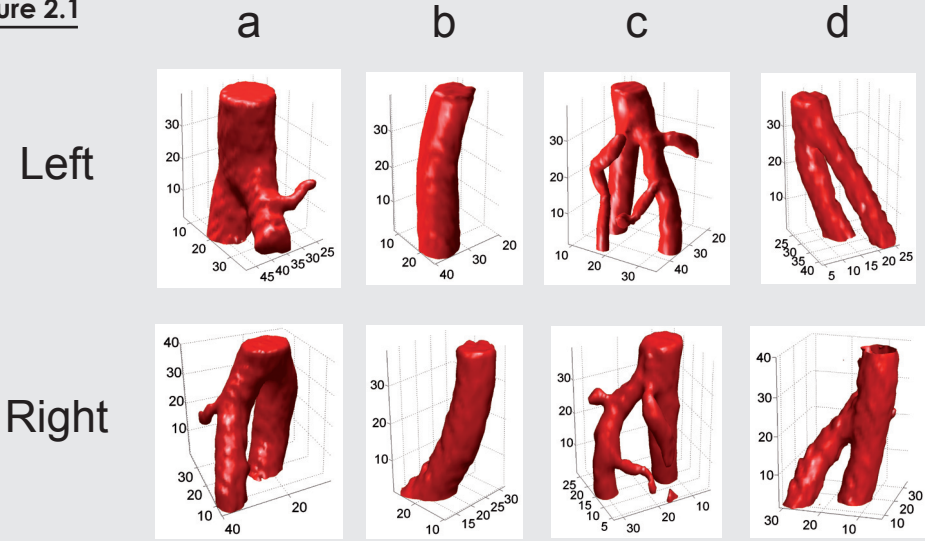
Because the same amount of contrast agent was injected in each patient, we determined Pearson's correlations between the AIF characteristics and body weight [64-66]. Where a significant correlation was found, we removed the trend from the data and calculated the weight-corrected SD and CV.

The intra-exam variations between slices and arteries, and the day-to-day variations in the exam-specific AIFs were quantified with the within-subject standard deviation (WSD) [67, 68]. The within-subject coefficient of variation (wcv) is also presented, being the WSD as fraction of the mean.

Differences may exist in the AIF characteristics above and below a bifurcation in the femoral arteries. We therefore calculated the mean AIF characteristics above and below a bifurcation and tested for differences with a paired Student's t-test.

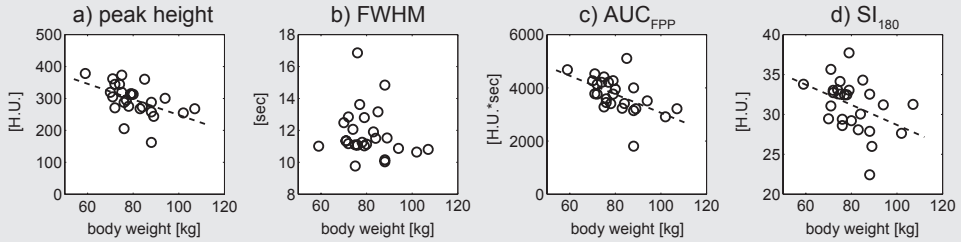
Finally, the Wilcoxon signed rank test was used to test for equal medians in the paired K^{trans} distributions as calculated with the patient-specific and population-averaged AIF. Pearson's correlations were calculated between the percentage errors in K^{trans} in the PZ and ROI_{susp} to investigate the effect of AIF choice on different prostate regions. Furthermore, Pearson's correlations were calculated between the percentage errors in K^{trans} and the percentage errors in the peak height, FWHM, AUC_{FPP} and SI_{180} of the exam-specific AIFs as compared to the population-averaged AIF.

Figure 2.1



Four examples (a-d) of three-dimensional DCE-CT masks of the left and right femoral arteries in patients of 77, 69, 63 and 63 years respectively. There is considerable variation in anatomy in the imaged volume. The image axes are in mm.

Figure 2.2



Inter-patient variations in AIF characteristics from the first DCE-CT exam plotted as a function of body weight. For the peak height, AUC_{FPP} and SI_{180} , a significant correlation was found with the body weight. The dashed trend line was used to calculate the weight-corrected CV in Table 2.1.

Table 2.1 Inter-patient variations of the AIF

(N=28)	Mean	Uncorrected for weight		Corrected for weight	
		SD	CV	SD	CV
Peak height [H.U.]	296.1	50.3	17.0%	43.4	14.7%
FWHM [sec]	11.8	1.5	13.1%	-	-
AUC_{FPP} [H.U.*sec]	3740	672	18.0%	567	15.1%
SI_{180} [H.U.]	31.1	3.2	10.4%	3.0	9.5%

2.3 Results

Figure 2.1 shows for four patients the three-dimensional DCE-CT masks in which the AIF was measured. At this level of the femoral arteries a considerable variation in anatomy exists between patients. The noise level is on average 3.6 ± 1.0 H.U. within a slice, 0.6 ± 0.1 H.U. within an artery and 0.5 ± 0.1 H.U. within one exam.

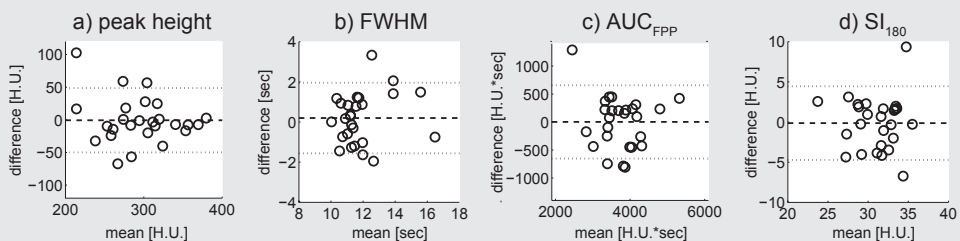
The inter-patient variations in AIF characteristics are shown in Figure 2.2 as a function of body weight. A significant correlation with the body weight was found for the peak height ($r = -0.504$, $p = 0.0086$), AUC_{FPP} ($r = -0.538$, $p = 0.0045$) and SI_{180} ($r = -0.405$, $p = 0.040$), but not for the FWHM ($r = -0.148$, $p = 0.470$). After correcting for body weight the cv of the peak height, AUC_{FPP} and SI_{180} reduced to 14.7%, 15.1% and 9.5% respectively (Table 2.1).

Between the first and second DCE-CT exam no significant differences were found in peak height ($p = 0.925$), FWHM ($p = 0.431$), AUC_{FPP} ($p = 0.982$) and SI_{180} ($p = 0.837$), as shown in the Bland-Altman plots in Figure 2.3. The wcv varies from 7.5 to 8.9% (Table 2.2), reflecting the day-to-day intra-patient variations.

As an example of intra-exam and intra-patient variations, in Figure 2.4 the AIFs from a 77-year old patient are shown. Very similar AIFs are found in both exams, in both arteries, and between slices. For the entire patient group the wcv between the left and right artery is between 1.3 and 6.6% (Table 2.3), indicating very small differences in AIF between the left and right artery. The variations between slices are larger with a wcv between 2.0 and 13.5% (Table 2.3).

The absolute wsd of SI_{180} between slices (4.1 H.U.) is roughly equal to the average noise level within a slice (3.6 H.U.), whereas the wsd of SI_{180} between the left and right artery (2.0 H.U.) is slightly larger than the average noise level within an artery (0.6 H.U.). When comparing the AIF characteristics above and below a bifurcation, no significant differences were found in peak height ($p = 0.564$), FWHM ($p = 0.630$), AUC_{FPP} ($p = 0.659$) and SI_{180} ($p = 0.745$).

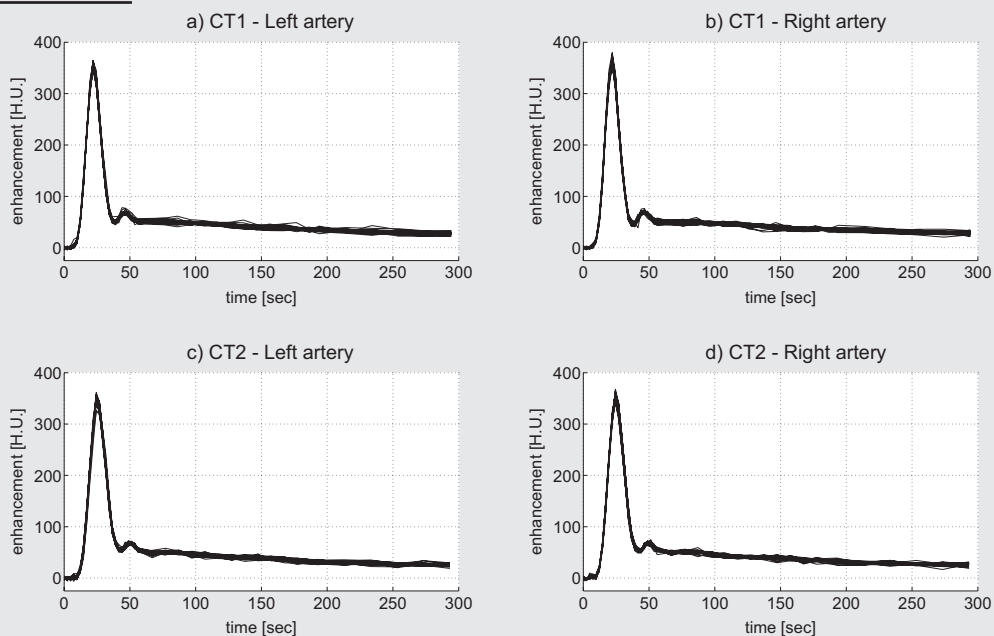
Figure 2.3



*Bland-Altman plots of the AIF characteristics from the repeated DCE-CT exams, showing intra-patient variations in peak height, FWHM, AUC_{FPP} and SI_{180} . The dashed line is the mean of the differences and the dotted lines are at the mean \pm 1.96 * wSD, representing the range of the difference between a subject's measurement and the true value for 95% of observations.*

Table 2.2 Intra-patient variations of the AIF between repeated DCE-CT exams

(N=28)	Mean	wSD	wCV
Peak height [H.U.]	295.7	25.1	8.5%
FWHM [sec]	11.9	0.9	7.6%
AUC_{FPP} [H.U.*sec]	3741	334	8.9%
SI₁₈₀ [H.U.]	31.1	2.3	7.5%

Figure 2.4

*Intra-exam variations in the AIFs from a 77-year old patient in the left and right femoral arteries for the first and second DCE-CT exam. In each subfigure the AIFs from all slices are overlaid. The average peak height, FWHM, AUC_{FPP} and SI₁₈₀ of the first exam are 305.5 H.U., 13.2 sec, 5108 H.U.*sec and 28.4 H.U. respectively, and 299.6 H.U., 14.6 sec, 5531 H.U.*sec and 24.6 H.U. for the second exam.*

Table 2.3 Intra-exam variations of the AIF

	Mean	Between the left and right artery (N=56)		Between slices (N=112)	
		wSD	wCV	wSD	wCV
Peak height [H.U.]	298.0	4.6	1.6%	8.5	2.8%
FWHM [sec]	11.9	0.2	1.3%	0.2	2.0%
AUC_{FPP} [H.U.*sec]	3751	48	1.3%	107	2.8%
SI₁₈₀ [H.U.]	30.5	2.0	6.6%	4.1	13.5%

Figure 2.5 shows our population-averaged AIF as calculated from the group of 28 prostate cancer patients (see Supplement 1 for data points). A small second-pass peak is visible, after which the AIF becomes stable. Most inter-patient variations are seen on the peak of the AIF as reflected in Table 2.1. On the tail of the AIF, the inter-patient variations are very small compared to the peak.

The median K^{trans} values in the PZ (Figure 2.6a) and ROI_{susp} (Figure 2.6b) were not significantly different when calculated with the population-averaged AIF as compared to an exam-specific AIF ($p = 0.784$ for PZ, $p = 0.429$ for ROI_{susp}). However, for individual patients median deviations in K^{trans} are 11.3% (range 0.8 to 31.4% without outliers), and 14.3% (range 0.9 to 30.6% without outliers), for the PZ and ROI_{susp} respectively, when calculated with a population-averaged AIF (Figure 2.6c). Except for the FWHM, the deviations in AIF characteristics strongly correlated with the errors in K^{trans} in the PZ and ROI_{susp} ($-0.71 < r < -0.94$, $p < 0.0001$). This indicates that the more dissimilar the population-averaged AIF is compared to the exam-specific AIF, the larger the error in K^{trans} will be. Also, a very strong Pearson correlation exists between the deviations in the K^{trans} values in the PZ and ROI_{susp} ($r = 0.9897$, $p < 0.001$). This shows that the impact of a population-averaged AIF on the K^{trans} map in a single patient is mainly a homogeneous scaling of the values.

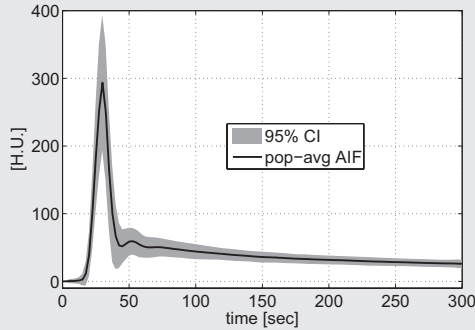
2.4 Discussion

For the quantitative analysis of DCE data with a tracer kinetic model an AIF is required. The reliable measurement of an exam specific AIF can be challenging, in particular in DCE-MRI [33-37, 46, 47]. The use of a population-averaged AIF can be a good alternative to an exam specific AIF, if the latter cannot be measured with sufficient accuracy. In order to make a well-founded choice for one or the other, we investigated when a population-averaged or an exam-specific arterial input function (AIF) should be used.

With an exam-specific AIF the intra-exam variations between the left and right femoral arteries vary between wCV values of 1.3 and 6.6%. These variations include measurement errors and differences in anatomical location and can therefore be considered to provide an upper limit of the AIF measurement precision of our DCE-CT protocol. An exam-specific AIF is very stable over time, with day-to-day variations between 7.5 and 8.9%. The use of a population-averaged AIF will neglect both intra-patient and inter-patient variations, resulting in a CV between 9.5 and 15.1%.

As expected, the inter-patient variations in peak height, AUC_{FPP} and SI_{180} showed a significant correlation with body weight due to the fixed amount of contrast agent that was injected in each patient. This finding is consistent with theory [66] and with other studies that also found an inverse relationship between body weight and the amplitude of the enhancement [69, 70].

We found inter-patient variations in AIF characteristics between 9.5 and 15.1%. In a DCE-CT study by Kim *et al* [70], inter-patient variations in the AIF in the

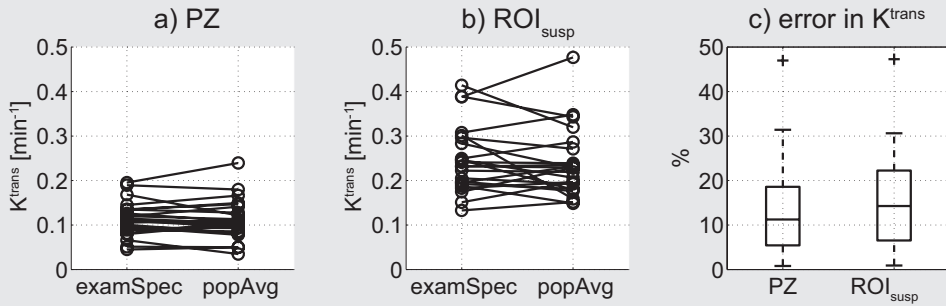
Figure 2.5

The population-averaged AIF is shown with the 95% confidence intervals (CI) of the inter-patient variations. It has a peak height of 293.6 H.U., a FWHM of 11.8 sec, an AUC_{EPP} of 3860 H.U.*sec and an SI_{180} of 31.2 H.U., as defined in Supplement 1. The 95% CI is based on the 28 single AIFs and therefore includes both the random and the weight-dependent variations between patients (Figure 2.2 and Table 2.1).

femoral arteries were reported between 15,5 and 51% in the tail and peak of the AIF respectively. The larger variations in the peak height compared to our study are most probably caused by a longer injection time, on average 26.6 sec, compared to our injection protocol of 10 sec. Parker *et al* quantified the inter-patient variations in AIFs with DCE-MRI in a similar patient group and measurement location and found CV values of about 50% in the peak height and 25% in the tail of the AIF [49]. They concluded that the reproducibility of tracer kinetic model parameters became better with a population-averaged AIF. These findings suggest a larger measurement error on DCE-MRI and a worse reproducibility for DCE-CT protocols with longer injection times compared to our data. Mendichovszky *et al* also reported higher CV values of up to 37.1% in the human abdominal aorta as measured with DCE-MRI [71]. Because in that study the signal intensities were not converted to concentration-time curves, a detailed comparison with our results is difficult.

Within one patient the measurement of the AIF in two subsequent DCE-CT exams is highly repeatable, with a wcv less than 8,9% for all AIF characteristics. Apart from the intra-exam variations, these values represent true day-to-day variations within patients, since no intervention took place between the two DCE-CT exams and the contrast injection was performed with a power injector. Few studies report repeatability values of the AIF characteristics. Mendichovszky *et al* found that Spearman's correlation coefficients for all parameters, except FWHM, were low (0.66-0.82) using MR signal intensities [71]. Other DCE-MRI repeatability studies mention the repeatability of the tracer kinetic model parameters, rather than the repeatability of the AIF [55, 72-74].

With a population-averaged AIF, variations in AIF characteristics of up to about 15% are neglected, resulting in errors in K^{trans} in the prostate of up to 30% for individual patients. A number of other studies also evaluated the consequences of the choice for a particular AIF on the observed errors or repeatability of tracer kinetic model

Figure 2.6

For individual patients, the absolute K^{trans} values in the prostate can vary considerable between an exam-specific (examSpec) and a population-averaged (popAvg) AIF in a) the healthy considered peripheral zone (PZ) and b) regions suspected for tumor (ROI_{susp}). The percentage errors in the K^{trans} values of individual patients when calculated with a population-averaged AIF are shown in c).

parameters [49, 50, 52-55, 70, 75]. In the DCE-CT study by Kim *et al* [70], the variations in AIF between 15,5 and 51% resulted in errors in K^{trans} of 13,5%, which is very similar to our results. Kershaw *et al* showed that the errors in the tracer kinetic model parameters of the adiabatic approximation to the tissue homogeneity (AATH) model are roughly linear with the error in the peak height of the AIF [75].

A limitation of this study is the way in which we calculated the percentage errors in K^{trans} when using a population-averaged AIF. We report these errors relative to the K^{trans} values as calculated with the exam-specific AIF. This implicitly assumes that the exam-specific AIF is the golden standard. This is a reasonable assumption, as the measurement precision of the exam-specific AIFs is very high, reflected by the very small wcv between the left and right arteries.

Because of the technical challenges involved in measuring the physiological variations in the AIF directly on MRI, we used CT as a benchmark. It is common practice to inject a weight-dependent amount of contrast agent for DCE-MRI exams, whereas in this study a fixed amount of contrast agent was used. Although this may lead to small differences in the AIF itself [63], we believe that the inter-patient, intra-patient and intra-exam variations as seen on DCE-CT are also representative for the physiological variations in the AIFs in DCE-MRI exams in the pelvis in case of similar injection times and similar patient groups. The modality-independent CT-based AIF presented in this study can then be used to calculate a population-averaged AIF for DCE-MRI analysis of the pelvis, in case of a similar injection time and patient group. When having an average patient weight of 80 kg and a 1M MR contrast agent at 0.1 ml/kg, 8 mmol of contrast agent will be injected in the ‘average’ patient. The modality-independent AIF, as defined in Supplement 1, can then be easily multiplied by a factor of 8 mmol to obtain a population-averaged AIF in mM. This approach is supported by the good correspondence found in the over-all AIF shape in a comparative study between CT-based AIFs and AIFs from the DCE-MRI phase signal

in a different group of prostate cancer patients [63]. Although some simulation studies on injection protocols have been performed [76, 77], the dependency of an AIF on the exact injection protocol remains unclear and comparative studies between measured DCE-CT and DCE-MRI AIFs are scarce.

In conclusion, for longitudinal and multi-center studies of quantitative DCE imaging, the use of a population-averaged AIF is advantageous when the measurement precision of an exam-specific AIF is considerably worse than 15%. Furthermore, the measurement of the AIF on DCE-CT is highly repeatable and hardly dependent on the anatomy at the level of the femoral arteries. With the data presented in this study, a founded decision on the use of an exam-specific or a population-averaged AIF can be made, that minimizes the errors in the measurement of tracer kinetic model parameters.

2.5 Supplement 1 || Population-averaged AIF

Time [sec]	AIF [H.U.]	std [H.U.]	AIF (mM/mmol)	std (mM/mmol)
0,0	0,00	0,00	0,0000	0,0000
2,5	0,13	0,24	0,0003	0,0005
5,0	0,40	1,43	0,0008	0,0028
7,5	0,52	1,63	0,0010	0,0032
10,0	0,73	1,87	0,0014	0,0037
12,5	1,38	2,50	0,0027	0,0049
15,0	2,77	4,23	0,0054	0,0083
17,5	11,33	8,72	0,0222	0,0171
20,0	39,90	16,11	0,0782	0,0315
22,5	102,96	27,82	0,2017	0,0545
25,0	182,36	39,84	0,3572	0,0780
27,5	253,60	48,66	0,4967	0,0953
30,0	293,60	50,07	0,5750	0,0981
32,5	249,67	50,66	0,4890	0,0992
35,0	163,83	44,24	0,3209	0,0866
37,5	99,91	35,61	0,1957	0,0697
40,0	66,43	24,02	0,1301	0,0470
42,5	53,07	16,63	0,1039	0,0326
45,0	51,82	12,56	0,1015	0,0246
47,5	55,32	11,41	0,1084	0,0224
50,0	58,74	10,30	0,1150	0,0202
52,5	59,45	9,78	0,1164	0,0192

Uncertainties in the arterial input function

Time [sec]	AIF [H.U.]	std [H.U.]	AIF (mM/mmol)	std (mM/mmol)
55,0	57,80	9,72	0,1132	0,0190
57,5	54,81	9,44	0,1074	0,0185
60,0	52,27	8,44	0,1024	0,0165
62,5	50,73	7,83	0,0994	0,0153
65,0	50,25	7,61	0,0984	0,0149
67,5	50,40	7,47	0,0987	0,0146
70,0	50,60	7,23	0,0991	0,0142
72,5	50,60	6,88	0,0991	0,0135
75,0	50,20	6,62	0,0983	0,0130
77,5	49,57	6,44	0,0971	0,0126
80,0	48,89	6,34	0,0958	0,0124
82,5	48,22	6,20	0,0944	0,0121
85,0	47,61	6,04	0,0932	0,0118
87,5	47,03	5,92	0,0921	0,0116
90,0	46,46	5,82	0,0910	0,0114
92,5	45,84	5,77	0,0898	0,0113
95,0	45,24	5,72	0,0886	0,0112
97,5	44,67	5,64	0,0875	0,0110
100,0	44,12	5,56	0,0864	0,0109
102,5	43,62	5,40	0,0854	0,0106
105,0	43,18	5,23	0,0846	0,0102
107,5	42,77	5,09	0,0838	0,0100
110,0	42,36	4,95	0,0830	0,0097
112,5	41,95	4,76	0,0822	0,0093
115,0	41,51	4,59	0,0813	0,0090
117,5	41,07	4,45	0,0804	0,0087
120,0	40,64	4,34	0,0796	0,0085
122,5	40,16	4,34	0,0787	0,0085
125,0	39,72	4,33	0,0778	0,0085
127,5	39,29	4,29	0,0770	0,0084
130,0	38,86	4,27	0,0761	0,0084
132,5	38,51	4,19	0,0754	0,0082
135,0	38,17	4,10	0,0748	0,0080
137,5	37,82	4,00	0,0741	0,0078
140,0	37,46	3,95	0,0734	0,0077
142,5	37,03	3,99	0,0725	0,0078
145,0	36,63	4,01	0,0717	0,0079
147,5	36,30	4,02	0,0711	0,0079
150,0	36,00	4,05	0,0705	0,0079

Supplement 1 || Continued

Time [sec]	AIF [H.U.]	std [H.U.]	AIF (mM/mmol)	std (mM/mmol)
152,5	35,81	3,97	0,0701	0,0078
155,0	35,62	3,87	0,0698	0,0076
157,5	35,44	3,79	0,0694	0,0074
160,0	35,25	3,73	0,0690	0,0073
162,5	35,00	3,71	0,0686	0,0073
165,0	34,75	3,71	0,0681	0,0073
167,5	34,43	3,66	0,0674	0,0072
170,0	34,11	3,59	0,0668	0,0070
172,5	33,83	3,48	0,0663	0,0068
175,0	33,58	3,40	0,0658	0,0067
177,5	33,41	3,40	0,0654	0,0067
180,0	33,24	3,41	0,0651	0,0067
182,5	33,03	3,49	0,0647	0,0068
185,0	32,84	3,47	0,0643	0,0068
187,5	32,61	3,40	0,0639	0,0067
190,0	32,41	3,35	0,0635	0,0066
192,5	32,22	3,33	0,0631	0,0065
195,0	32,06	3,29	0,0628	0,0064
197,5	31,91	3,28	0,0625	0,0064
200,0	31,77	3,25	0,0622	0,0064
202,5	31,63	3,23	0,0619	0,0063
205,0	31,47	3,20	0,0616	0,0063
207,5	31,34	3,18	0,0614	0,0062
210,0	31,19	3,16	0,0611	0,0062
212,5	31,02	3,16	0,0608	0,0062
215,0	30,83	3,15	0,0604	0,0062
217,5	30,64	3,14	0,0600	0,0061
220,0	30,45	3,14	0,0596	0,0061
222,5	30,27	3,15	0,0593	0,0062
225,0	30,08	3,15	0,0589	0,0062
227,5	29,87	3,15	0,0585	0,0062
230,0	29,68	3,14	0,0581	0,0062
232,5	29,52	3,10	0,0578	0,0061
235,0	29,37	3,07	0,0575	0,0060
237,5	29,24	3,04	0,0573	0,0060
240,0	29,10	3,01	0,0570	0,0059

Time [sec]	AIF [H.U.]	std [H.U.]	AIF (mM/mmol)	std (mM/mmol)
242,5	28,96	2,97	0,0567	0,0058
245,0	28,83	2,94	0,0565	0,0058
247,5	28,70	2,91	0,0562	0,0057
250,0	28,59	2,89	0,0560	0,0057
252,5	28,45	2,85	0,0557	0,0056
255,0	28,31	2,81	0,0555	0,0055
257,5	28,17	2,79	0,0552	0,0055
260,0	28,02	2,78	0,0549	0,0054
262,5	27,88	2,78	0,0546	0,0054
265,0	27,74	2,79	0,0543	0,0055
267,5	27,59	2,80	0,0540	0,0055
270,0	27,43	2,82	0,0537	0,0055
272,5	27,28	2,83	0,0534	0,0055
275,0	27,14	2,81	0,0532	0,0055
277,5	27,01	2,78	0,0529	0,0055
280,0	26,88	2,74	0,0526	0,0054
282,5	26,76	2,70	0,0524	0,0053
285,0	26,62	2,72	0,0521	0,0053
287,5	26,58	2,78	0,0521	0,0054
290,0	26,50	2,76	0,0519	0,0054
292,5	26,47	2,92	0,0518	0,0057
295,0	26,42	2,97	0,0518	0,0058
297,5	26,11	3,19	0,0511	0,0063
300,0	26,11	2,84	0,0511	0,0056

3

Chapter 3

Phase-based arterial input function (AIF) measurements in the femoral arteries for quantification of dynamic contrast-enhanced (DCE) MRI and comparison with DCE-CT

Abstract

Dynamic contrast-enhanced (DCE) MRI is useful for diagnosis, treatment monitoring and follow-up of prostate cancer. However, large differences have been reported in the parameter range of the transfer constant K^{trans} , making longitudinal studies and comparison of DCE-MRI findings between studies difficult. Large part of this inconsistency in K^{trans} values can be attributed to problems with the accurate measurement of the arterial input function (AIF) from the magnitude signal (AIF_{MAGN}). Phase-based AIF measurements ($\text{AIF}_{\text{PHASE}}$) have been proposed as a more robust alternative to AIF_{MAGN} measurements. This study compares $\text{AIF}_{\text{PHASE}}$ measurements with AIFs measured with DCE-CT (AIF_{CT}), and the corresponding K^{trans} maps in 12 prostate cancer patients. The shape of $\text{AIF}_{\text{PHASE}}$ and AIF_{CT} are similar, although differences in the peak height and peak width exist as a result of differences in injection protocol. No significant differences in K^{trans} values were found between the DCE-MRI and DCE-CT exams, with median K^{trans} values of 0.10 and 0.08 min^{-1} for healthy peripheral zone tissue and 0.44 and 0.36 min^{-1} for regions suspected of tumor respectively. Therefore, robust quantification of K^{trans} values from DCE-MRI exams in the cancerous prostate is feasible with the use of $\text{AIF}_{\text{PHASE}}$.

A version of this chapter has been published as:

Phase-based arterial input function (AIF) measurements in the femoral arteries for quantification of dynamic contrast-enhanced (DCE) MRI and comparison with DCE-CT. J.G. Korpelaar, C.A.T. van den Berg, M.J.P. van Osch, G. Groenendaal, M. van Vulpen, and U.A. van der Heide
Magnetic Resonance in Medicine 2011; in press, DOI 10.1002/mrm.22905

3.1 Introduction

The use of dynamic contrast-enhanced (DCE) MR imaging in the diagnosis [27-29, 41, 42, 78], treatment monitoring [79-82] and follow-up [83-86] of prostate cancer has increased over the last years. Nevertheless, large differences have been reported in the parameter range of the transfer constant K^{trans} in healthy (0.06-0.60 min^{-1}) and cancerous (0.47-1.26 min^{-1}) prostate tissue [29, 41-43]. Differences in methodology between institutions and quantification problems inherent to the acquisition contribute to this inconsistency in K^{trans} values. This makes it difficult to perform longitudinal studies and to compare DCE-MRI findings between studies and research groups.

The measurement of an accurate arterial input function (AIF) is needed for reliable analysis of DCE-MRI data with a tracer kinetic model. However, measuring an AIF directly from the MR magnitude signal (AIF_{MAGN}) can be challenging. First, the magnitude signal from a T_1 -weighted spoiled gradient echo pulse sequence has a non-linear relationship with the contrast agent concentration [46]. Second, a reliable AIF_{MAGN} measurement in the femoral arteries is difficult because of T_2^* -effects at higher concentrations [33], B_1 -field inhomogeneities [37, 87] and inflow-artifacts [35, 36, 87].

As an alternative to the magnitude signal, the AIF can also be measured from the phase signal ($\text{AIF}_{\text{PHASE}}$), as reported by Akbudak *et al* [88, 89]. Advantageous are the linear relationship between phase shift and contrast agent concentration, the accurate prediction of shape factors [90, 91] and the insensitivity to the previously mentioned artifacts that influence AIF_{MAGN} measurements. Although the principle of measuring $\text{AIF}_{\text{PHASE}}$ is the same for T_1 -weighted DCE-MRI and T_2^* -weighted dynamic susceptibility contrast (DSC) MRI, the use of $\text{AIF}_{\text{PHASE}}$ has been more prominent in DSC-MRI literature, e.g. [64, 65, 92-94]. Regarding T_1 -weighted DCE-MRI, other groups showed recently that the measurement of $\text{AIF}_{\text{PHASE}}$ is highly feasible in human brain [95] and that subject-to-subject variations in K^{trans} in healthy muscle tissue are smaller when calculated with $\text{AIF}_{\text{PHASE}}$ rather than AIF_{MAGN} [96].

In this study, we perform $\text{AIF}_{\text{PHASE}}$ measurements in twelve prostate cancer patients and compare these with the AIFs measured with DCE-CT (AIF_{CT}) in the same patients. We chose dynamic contrast-enhanced CT (DCE-CT) for the comparison with $\text{AIF}_{\text{PHASE}}$, since CT does not suffer from the MR artifacts and a linear relationship exists between Hounsfield units (H.U.) and contrast agent concentration. Furthermore, we calculated K^{trans} maps of the prostate for all patients with the use of $\text{AIF}_{\text{PHASE}}$ and compared it to the corresponding K^{trans} maps from the DCE-CT exams.

3.2 Materials and methods

Calibration

To evaluate the accuracy of measuring the concentration of the contrast agent by the DCE-MRI phase signal, a concentration range in an aqueous solution of manganese(II) chloride (native $T_1 \sim 900$ ms) was varied from 0 to 5 mM gadobutrol (1.0 M Gadovist, Schering AG, Berlin, Germany). The tubes (length 100 mm, inner/outer diameter 13.5/16.0 mm) were positioned parallel to the main magnetic field of the MR scanner. In a similar way, a calibration of the DCE-CT signal enhancement as a function of contrast agent concentration was performed in tubes (length 91 mm, inner/outer diameter 22.0/25.0 mm) in which the concentration was varied from 0 to 12 mM iopromide (Ultravist 300, Schering AG, Berlin, Germany) in water. Both phantoms were scanned with the same imaging protocols as the subjects.

Subjects

In an ongoing prospective clinical trial of radiotherapy dose painting, patients receive a DCE-MRI and DCE-CT exam for tumor delineation. The study was approved by the local medical ethical research board, and all patients gave written informed consent. Scans were performed prior to radiation treatment, a median of 8.5 (range 0-15) days apart. In total 12 consecutive patients were selected for this analysis. They were diagnosed with local prostate cancer (Nx/o, Mx/o), had a mean age of 68 (range 56-84) years and a mean body weight of 77 (range 55-90) kg. T-stage varied from T1c-T4, the mean Gleason score was 7 (range 6-9) and the mean prostate-specific antigen (PSA) level was 21.2 (range 6.7-77.0) ng/mL. The patients had no contraindication for the CT contrast agent, the MRI contrast agent and the MRI exam.

Imaging protocol

All MRI acquisitions were performed on a 3 Tesla MR scanner (Achieva, Philips Healthcare, Best, The Netherlands). The DCE-MRI exam consisted of a T_1 -weighted 3D spoiled gradient echo sequence (20 transverse slices, slice thickness 5.0 mm, TR/TE 4.0/1.7 ms, acquisition matrix 160x160, FOV 40 cm, flip angle 8°). A total of 120 scans were obtained at a 2.4 s time interval. In each patient 0.1 ml/kg gadobutrol (1.0 M Gadovist, Schering AG, Berlin, Germany) was injected with a power injector (1ml/s or 2ml/s), followed by a saline flush. Furthermore, a T_2 -weighted scan was acquired with a fast spin-echo sequence for tumor delineation purposes (20 transverse slices, slice thickness 3.0 mm, TR/TE 6.717/0.120 s, acquisition matrix 256x254, FOV 20 cm).

The DCE-CT exam (120kV, 200mAs) consisted of acquisitions at 42 time points within a time window of 5 minutes. The first 24 acquisitions were taken at 2.4 s intervals, the next 12 at a 10 s interval and the last 6 at 20 s intervals. The increase in time interval was done to minimize the radiation burden. In each patient the injection of the iodine contrast agent (Ultravist 300, Schering AG, Berlin, Germany) with a power injector (60 ml, 6 ml/s) was followed by a saline flush. Patients were scanned with a 256-slice CT scanner (Brilliance iCT, Philips Healthcare, Best, The Netherlands) with 105 reconstructed slices of 0.35 x 0.35 x 0.64 mm voxels. The computed tomography dose index (CTDI) was 13.3 mGy per time point, resulting in a total dose of 0.56 Gy

per exam. While this is a high dose for a diagnostic exam, it is negligible compared to the dose delivered in the subsequent radiation therapy treatment. To all patients a treatment dose of at least 77 Gy was given in the prostate with the intensity-modulated (IMRT) technique, which results in a skin dose of about 10 Gy.

AIF measurement

AIF_{PHASE} was measured from the phase evolution over time in each femoral artery. For each voxel in the imaged volume, a map of the maximum phase enhancement over time was calculated. Based on this map, AIF voxels were manually selected in straight vessel segments of the femoral arteries. AIF_{PHASE} was calculated for each artery by averaging the phase enhancement over time in the manually selected voxels. The average phase signal ($\Delta\phi$) at a certain time point was converted from radians to concentration gadobutrol, C , using the following equation [89]:

$$\Delta\phi = \gamma \frac{\Delta\mathbf{B} \cdot \mathbf{H}_0}{\|\mathbf{H}_0\|} TE = \omega_0 \cdot \chi_M \cdot F \cdot C \cdot TE \quad [3.1],$$

with γ the gyromagnetic ratio, $\Delta\mathbf{B}$ the change in the magnetic field, \mathbf{H}_0 the static external magnetic field vector, TE the echo time of the DCE-MRI sequence and ω_0 the resonance frequency ($8.03 \cdot 10^8$ rad/s at 3T). The molar susceptibility of the contrast agent, χ_M , was calculated from the Langevin equation [89], yielding a value of 339 ppm/M at 293 K for the phantom measurement and 320 ppm/M at 310 K in vivo. The geometry factor of the susceptibility compartment, F , was calculated based on an exact equation for infinite cylinders, aligned under an angle θ with the main magnetic field (B_0) [89, 91]:

$$F = \frac{1}{3} - \frac{1}{2} \sin^2 \theta \quad [3.2].$$

The angle with B_0 was calculated by performing an orthogonal regression using principal components analysis on the centers of gravity of the voxels in the slices in which the AIF was determined. Each AIF_{PHASE} was corrected for drift of the B_0 -field, by subtracting the phase signal from a region in the most nearby Sartorius, Pectineus or Iliopsoas muscle in the same slice.

In view of the high amount of contrast agent that is administered during the DCE-MRI exam, it is expected that T_2^* -effects will affect the accurate measurement of AIF_{MAGN} . Nevertheless, for comparison with AIF_{PHASE} we determined AIF_{MAGN} by averaging the magnitude signal from the same voxels in which AIF_{PHASE} was measured. The magnitude signal was converted to concentration with a method published by Schabel *et al* [46], with a value of $4.5 \text{ L} \times \text{mmol}^{-1} \times \text{s}^{-1}$ for the r_1 -relaxivity of gadobutrol [97] and a fixed pre-contrast T_1 -value for blood of 1.66 seconds [98].

AIF_{CT} measurements were performed within a mask that incorporated a small region around the femoral arteries. AIF_{CT} was calculated for each slice, by subtracting the pre-contrast value from the peak CT value over time for each voxel within the mask. Only the voxels with a resulting value of 70% or more of the maximum enhancement in that slice were averaged to obtain an AIF for that slice. Finally, all slices were averaged, to obtain AIF_{CT} for both the left and right femoral artery. Each AIF_{CT} was converted from H.U. into concentration iopromide with the calibration results of the phantom measurement.

In tissues, the exchange rate of the contrast agents from the intravascular to the extracellular extravascular space (EES) is determined by the concentration difference between these compartments. Since both the MRI and CT contrast agents are dissolved in the blood plasma and not in the red blood cells, each AIF needs to be corrected for the volume of the red blood cells in full blood, which is the hematocrit value. Therefore, each AIF was multiplied by a factor of 1.18, based on a hematocrit of 0.38 and a small to large vessel ratio of 0.7 [45, 61].

Comparison of AIF_{PHASE} with AIF_{CT}

Two different contrast agents are used for the DCE-MRI and DCE-CT exam. If we consider that both are low molecular weight contrast agents (< 1 kDa), we can assume that the time characteristics of the concentration changes in the femoral arteries are independent of the particular small molecular tracer used.

In order to compare AIF_{PHASE} with AIF_{CT} , both AIFs should have the same units. Although both AIFs are in mM, the contrast agent itself and the administered amount relative to the body weight are different and make a direct comparison difficult. However, the height (mM) of an AIF is proportional to the amount (mmole) of contrast agent injected [64-66]. By dividing the concentrations of the AIFs by the amount of contrast agent injected, we obtain a single modality-independent and dose normalized unit (mM/mmole) for both AIFs. The shape and height of the dose-normalized AIF_{CT} and AIF_{PHASE} were compared with the means of four parameters, i.e. the area under the curve of the first pass peak (AUC_{FPP}), the peak height, the full width at half maximum (FWHM), and the signal intensity 180 seconds after the peak (SI_{180}). AUC_{FPP} was calculated independently for AIF_{PHASE} and AIF_{CT} and defined as the integral between two manually determined time points that marked the start and end of the first pass peak.

Tracer kinetic model analysis

The DCE-MRI signal enhancement in the prostate was converted to concentration using the variable flip angle method [99-101], with a value of $4.5 \text{ L} \times \text{mmol}^{-1} \times \text{s}^{-1}$ for the r_1 -relaxivity of gadobutrol [97]. Noise in the DCE-CT enhancement curves of the prostate was reduced, by smoothing the data with a kernel of 0.15cc, which is a good trade-off between spatial resolution and image noise [59]. To avoid systematic bias in the K^{trans} maps, the DCE-MRI enhancement curves were smoothed identically. Parameter maps of the extended Tofts model (with blood plasma component) were

calculated from the DCE-MRI and DCE-CT exams of each patient, with AIF_{PHASE} and AIF_{CT} respectively. Fitting was performed using an in-house developed computer program, written in the C++ programming language, as described in [59].

On both K^{trans} maps, two corresponding regions of interest (ROI) were delineated in the peripheral zone (PZ) of the prostate. First, a region suspected of tumor tissue (ROI_{susp}) was identified, based on elevated DCE-MRI K^{trans} values and a hypointense region on the T_2 -weighted MR scan. In the DCE-CT K^{trans} map, ROI_{susp} was placed in the corresponding lesion. Second, in the DCE-MRI and DCE-CT K^{trans} maps, corresponding ROIs were placed in a contralateral PZ region with low K^{trans} values, that were not suspected of disease. All ROIs had a standardized volume of 0.3 cm^3 , and from every ROI a mean enhancement curve was derived from which tracer kinetic model parameters were calculated and compared.

Statistical analysis

All statistical analyses were performed with Matlab (The MathWorks, Inc., 2008, version 7.7.0.471, Natick, MA, USA). Results were considered statistically significant at $p < 0.05$.

To quantify the linear relationship between phase shift and contrast agent concentration in the MR phantom, a linear regression was performed and the Pearson correlation coefficient was calculated. For the CT phantom, the same analysis was performed to quantify the linear relationship between signal attenuation and contrast agent concentration. For the MR phantom we additionally tested with a Student's t-test the null-hypothesis whether the slope of the regression line was equal to 1, which would mean that the measured concentrations, based on the theoretical value of the susceptibility, are identical to the real concentrations in the phantom.

We calculated the mean and standard deviation of AUC_{FPP} , peak height, FWHM and SI_{180} of the dose-normalized AIF_{PHASE} and AIF_{CT} and tested for differences with a paired Student's t-test.

A common measure for quantifying reproducibility, is the within-subject standard deviation (WSD), which equals the square root of the group-averaged variance of the multiple measurements per subject [68]. We use the WSD as a measure for the AIF measurement consistency within one patient between the left and right femoral arteries. The WSD is also presented as a fraction of the mean parameter value, being the within-subject coefficient of variation (wcv).

To test for equal medians in the K^{trans} values from the ROI analysis, a paired Wilcoxon signed rank test was used. The reproducibility of K^{trans} values between DCE-MRI and DCE-CT was quantified by calculating the WSD. Additionally, Pearson correlation coefficients were calculated between the differences in K^{trans} and the differences in AUC_{FPP} , peak height, FWHM and SI_{180} between AIF_{PHASE} and AIF_{CT} , to investigate whether differences in K^{trans} are caused by differences in the AIF.

3.3 Results

Calibration

The DCE-MRI phantom measurement (Figure 3.1a) resulted in a Pearson correlation coefficient of 0.9986 ($p < 1 \cdot 10^{-9}$) and can be described by:

$$\text{gadobutrol}_{\text{measured}} [\text{mM}] = 0.954 \times \text{gadobutrol}_{\text{real}} [\text{mM}] + 0.003 \quad [3.3],$$

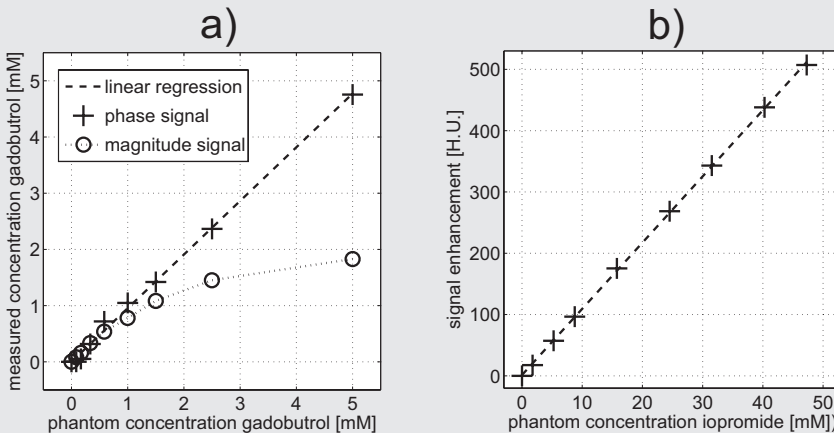
with 95% confidence intervals on the slope and intercept of $[0.909 - 0.999]$ and $[-0.086 - 0.092]$ respectively. The phase signal shows a linear relationship with the concentration gadobutrol, whereas the magnitude signal suffers from signal saturation (Figure 3.1a). The slope of the regression line was slightly but significantly different from the identity line ($p = 0.023$). Therefore, we adjusted the $\text{AIF}_{\text{PHASE}}$ measurements in the patient examinations with Equation 3.3.

The DCE-CT phantom measurement (Figure 3.1b) resulted in a Pearson correlation coefficient of 0.9998 ($p < 1 \cdot 10^{-12}$) and can be described by:

$$\text{enhancement} [\text{H.U.}] = 10.799 \times \text{iopromide} [\text{mM}] + 1.405 \quad [3.4],$$

with 95% confidence intervals on the slope and intercept of $[10.391 - 11.207]$ and $[-8.964 - 11.773]$ respectively. Equation 3.4 was used to convert each AIF_{CT} measured in H.U. into the corresponding concentration iopromide.

Figure 3.1

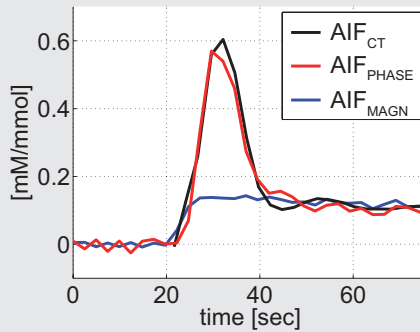


In a), the results of the DCE-MRI phantom measurement are shown for both the phase and the magnitude signal. The phase signal shows a linear relationship with the concentration gadobutrol, whereas the magnitude signal shows saturation. In b), the calibration curve for the DCE-CT is shown, with the measured data points displayed as black plus signs and the linear regression as black dashed line.

Comparison of AIF_{PHASE} with AIF_{CT}

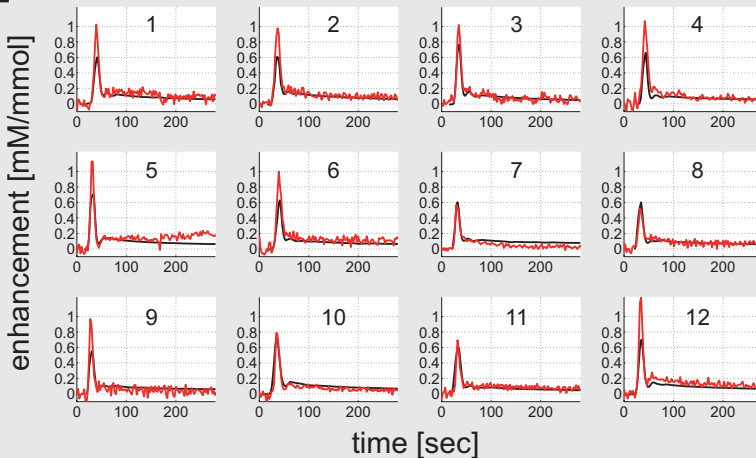
In Figure 3.2, for one patient the AIF_{CT} and AIF_{PHASE} are shown as well as the AIF_{MAGN} . As expected, AIF_{MAGN} has an anomalous shape and incorrect height due to the saturation of the signal. This pattern was observed in all patients. In contrast, a large similarity in the shape between AIF_{PHASE} and AIF_{CT} was found (Figure 3.3). The noise level in AIF_{PHASE} is higher than in AIF_{CT} . After quantitative comparison of the AIFs, significant differences were found in AUC_{FPP} peak height and FWHM between AIF_{PHASE} and AIF_{CT} (Table 3.1). AIF_{PHASE} exhibits a somewhat narrower and higher first pass peak compared to AIF_{CT} (Table 3.1), possibly reflecting differences in injection protocol. No significant differences were found in st_{180} , indicating that the two contrast agents are distributed homogeneously throughout the blood and leakage space in a similar way.

Figure 3.2



An example of the first pass peak of the dose normalized AIF_{PHASE} , AIF_{CT} and AIF_{MAGN} for patient 7 from Figure 3.3. AIF_{MAGN} shows an anomalous shape and incorrect height and is in this figure scaled to the tail of AIF_{CT} for illustrative purposes.

Figure 3.3



Dose normalized AIF_{PHASE} (red) and AIF_{CT} (black) for all patients. In all patients, the shape and height of AIF_{PHASE} are very similar to AIF_{CT} . Patient 5 moved during the DCE-MRI exam after about 150 seconds, leading to an apparent increase in enhancement.

The measurement consistency of AIF_{PHASE} between the left and right femoral arteries yields a wCV that is larger than the wCV of AIF_{CT} (Table 3.2). Although the wSD values for SI_{180} are the same as for the peak height (Table 3.2), the corresponding wCV values are about ten times higher for SI_{180} compared to the peak height. This is because the mean peak height is about ten times larger than SI_{180} for both AIF_{PHASE} and AIF_{CT} (Table 3.1).

Tracer kinetic model analysis

Figure 3.4 shows from three patients the K^{trans} maps in corresponding slices from the DCE-CT exam and the DCE-MRI exam when calculated with AIF_{PHASE} . Similar K^{trans} patterns are found in all patients. Quantitative analysis of the K^{trans} values calculated from the delineated ROIs (Table 3.3) shows no significant differences between the DCE-MRI and DCE-CT exams for the healthy considered PZ tissue ($p = 0.233$) and ROI_{susp} ($p = 0.092$). The Bland-Altman plot in Figure 3.5 confirms that no systematic differences exist between K^{trans} values from the DCE-MRI and DCE-CT exams, with corresponding wSD values for the PZ and ROI_{susp} of 0.03 and 0.10 min^{-1} respectively. No significant correlations ($-0.11 < r < 0.26$, all $p > 0.420$) were found between the differences in K^{trans} and differences in AUC_{FPP} , peak height, FWHM and SI_{180} between AIF_{PHASE} and AIF_{CT} . This indicates that the differences in AIF_{PHASE} and AIF_{CT} as shown in Table 3.1 and Figure 3.3 are not the underlying cause of the differences in K^{trans} between DCE-MRI and DCE-CT. In conclusion, robust quantification of K^{trans} values from DCE-MRI exams in the cancerous prostate is feasible with the use of AIF_{PHASE} when compared to DCE-CT.

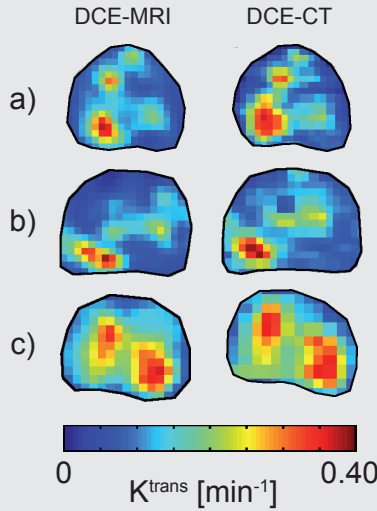
Table 3.1 AIF characteristics for AIF_{PHASE} and AIF_{CT}

(N=12)	AIF_{PHASE} [mean \pm std]	AIF_{CT} [mean \pm std]	paired Student's t-test
AUC_{FPP} [mM/mmol*sec]	9.7 \pm 2.5	8.0 \pm 1.1	$p = 0.048$
Peak height [mM/mmol]	0.92 \pm 0.22	0.65 \pm 0.07	$p = 0.001$
FWHM [sec]	9.9 \pm 1.4	11.7 \pm 0.9	$p = 0.006$
SI_{180} [mM/mmol]	0.08 \pm 0.04	0.07 \pm 0.01	$p = 0.630$

Table 3.2 AIF measurement consistency between the left and right artery

(N=12)	AIF_{PHASE}		AIF_{CT}	
	wSD	wCV	wSD	wCV
AUC_{FPP} [mM/mmol*sec]	1.6	16.2%	0.2	3.3%
Peak height [mM/mmol]	0.06	7.0%	0.02	2.6%
FWHM [sec]	0.9	8.6%	0.3	2.9%
SI_{180} [mM/mmol]	0.06	76.6%	0.01	19.0%

Figure 3.4

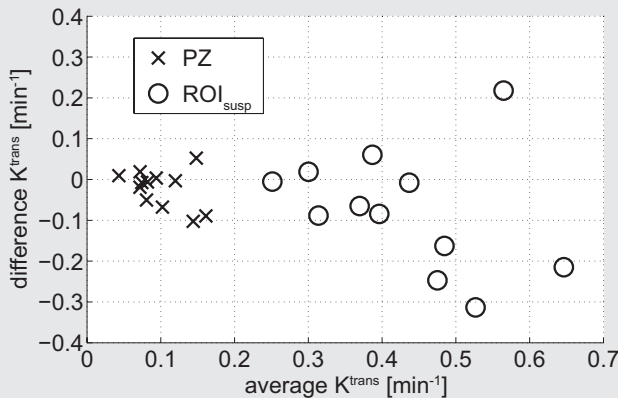


Examples of transversal slices of K^{trans} maps, corresponding to patient 1 (a), 11 (b) and 12 (c) from Figure 3.3. All patients show similar patterns and K^{trans} values between the DCE-CT and the DCE-MRI exam when calculated with AIF_{PHASE} . To enable unbiased visual comparison, the DCE-CT maps were downsampled to the resolution of the DCE-MRI maps.

Table 3.3 Median K^{trans} values (with range) in the prostate

(N=12)	DCE-MRI [min^{-1}]	DCE-CT [min^{-1}]	Paired Wilcoxon signed rank test
PZ	0.10 (0.04 - 0.21)	0.08 (0.05 - 0.17)	$p = 0.380$
ROI_{susp}	0.44 (0.25 - 0.75)	0.36 (0.25 - 0.67)	$p = 0.176$

Figure 3.5



Bland-Altman plot of the K^{trans} values in ROI_{susp} and the PZ from the DCE-MRI and DCE-CT exam. The wSD values for the PZ and ROI_{susp} are 0.03 and 0.10 min^{-1} respectively.

3.4 Discussion

Measurement of an arterial input function (AIF) from DCE-MRI magnitude images can be quite challenging, especially at higher field strength and at high amounts of contrast agent. The use of a pre-bolus [102] is one approach to avoid signal saturation, while maintaining a high signal-to-noise ratio in the tissue of interest. Inflow effects can be avoided by selecting a slice for AIF measurement distal from the inflow side of the imaged volume [87]. To minimize the effects of an imperfect slice excitation profile, the outer slices should also be avoided.

An alternative method to avoid these artifacts is to measure the AIF from the DCE-MRI phase signal. The feasibility of this approach was shown earlier in a phantom and in a baboon model [88, 89]. Here, we compared AIF_{PHASE} measurements with AIF_{CT} in a group of 12 prostate cancer patients and found that the shape of AIF_{PHASE} and AIF_{CT} are similar, albeit with some differences in the peak height and peak width. Furthermore, the subsequent analysis with a tracer kinetic model showed no significant differences between the K^{trans} values in healthy and cancerous prostate tissue. This means that with the use of AIF_{PHASE} consistent K^{trans} measurements are feasible when compared with DCE-CT.

In our study, we have not optimized our injection and acquisition protocol to obtain a reliable AIF_{MAGN} . Indeed, we found that the AIF_{MAGN} was very poor due to T_2^* -effects, B_1 -field inhomogeneities and inflow effects. Nevertheless, under those circumstances we could reliably measure the AIF from the phase of the signal. This is reflected by the good qualitative agreement in shape with AIF_{CT} . However, we found differences in the parameters describing the AIF (Table 3.1). For the quantitative comparison of the AIFs, the normalization to the injected amount of contrast agent may have introduced inaccuracies. More importantly, large differences exist between the injection protocols of the DCE-MRI and DCE-CT exams. On CT, 60 ml contrast agent was injected with a speed of 6 ml/s, whereas on MRI 0.1 ml contrast agent per kg bodyweight was injected with 1 or 2 ml/s. Yet, in both protocols the total injection time is shorter than the blood circulation time in the patients. As a result, the shape of the peak is largely influenced by the dispersion of the contrast agent bolus as it travels through the heart and lungs. This explains why the qualitative shape is similar, and why the larger injection time on CT results in a somewhat larger FWHM of the first pass peak. This is consistent with the findings about the relationship between injection time and shape of the AIF in a porcine model and in theoretical simulations [103].

For AIF_{CT} we observed a high consistency between the measurements in the left and right arteries. This suggests that the higher wCV values found with AIF_{PHASE} are not related to actual differences in the concentration of the contrast agent. The higher wCV of AIF_{PHASE} will be caused at least partly by errors introduced through the shape factor in Equation 3.1. We used the approximation that the vessel is an infinitely long cylinder at an angle relative to the main magnetic field. Although this is not an unreasonable assumption for a vessel segment of a length four times its diameter

[104], the accuracy of determining the angle of such a vessel segment is limited. Furthermore, the higher noise levels in AIF_{PHASE} compared to AIF_{CT} (Figure 3.3) will contribute to more inconsistency between the left and right artery. Some studies have investigated the optimization of acquisition protocols for measuring AIF_{PHASE} [64, 65]. However, optimization of the noise levels in the phase signal for the AIF_{PHASE} measurement, may come at the expense of a decrease in the signal-to-noise level of the magnitude signal in the prostate.

In this study we compared the K^{trans} values in healthy and cancerous prostate tissue between DCE-MRI and DCE-CT exams and found no significant differences. Although the peak height of AIF_{PHASE} is on average larger than AIF_{CT} , this does not result in a systematic off-set in the corresponding K^{trans} values. In addition, the differences in AIF characteristics between AIF_{PHASE} and AIF_{CT} show no correlation with the differences in K^{trans} . Because of the differences in injection protocol, not only the AIF but also the corresponding enhancement curves in the prostate will have been slightly different between MRI and CT. These differences in the AIF and the prostate enhancement between CT and MRI will have canceled out during the subsequent quantification with a tracer kinetic model, resulting in similar K^{trans} values for the two injection protocols. So, the AIF_{PHASE} measurements did not result in systematic differences in K^{trans} values when compared to DCE-CT exams.

For the DCE-MRI and DCE-CT exam, we found median K^{trans} values of 0.10 and 0.08 min^{-1} respectively for healthy considered PZ tissue, with a corresponding WSD of 0.03 min^{-1} . This WSD is the same as found in a DCE-CT repeatability study for prostate cancer [59]. For volumes suspected of tumor, we found here median K^{trans} values of 0.44 and 0.36 min^{-1} for DCE-MRI and DCE-CT respectively, with a corresponding WSD of 0.10 min^{-1} . In the DCE-CT repeatability study an increase of WSD with K^{trans} was found to 0.06 min^{-1} at a K^{trans} of 0.4 min^{-1} .

Other groups compared for different tumor sites T_1 -weighted DCE-MRI with DCE-CT. In a group of 38 cervical cancer patients, Yang *et al* [105] used a population-averaged AIF and an AIF from a multiple-reference tissue method (MRTM) to analyze the DCE-MRI exams. They found that for both AIFs the K^{trans} values were significantly different when compared with K^{trans} values derived from DCE-CT exams. According to the researchers, this was most probably due to an erroneous scaling of the population-averaged and MRTM-derived AIF. Kierkels *et al* [47] used AIF_{MAGN} to analyze DCE-MRI exams in a group of rectal cancer patients. When they analyzed an average enhancement curve for each tumor, they found significantly lower values for the K^{trans} values of the DCE-CT exams, but a significant correlation with DCE-MRI. Using a different tracer kinetic model, Bains *et al* [106] compared the blood flow between DCE-MRI and DCE-CT in a group of bladder cancer patients, to determine the maximal effect of water exchange. Although they had large differences in injection protocol, they found that in most cases the discrepancy between DCE-MRI and DCE-CT parameter estimates was insignificant and that water exchange between intra- and extracellular space has a negligible effect on their clinical DCE-MRI.

For longitudinal DCE studies, reliable and robust quantification is required to enable treatment response monitoring and detection of recurrent prostate cancer. Changes in perfusion and permeability of the microvascular properties of the prostate have been reported after radiotherapy and androgen deprivation treatment [80-82]. This should be taken into account when analyzing DCE-MRI exams of suspected recurrent prostate cancer after radiation treatment [83-86].

This study has some limitations. First, large differences exist between the injection protocols of the DCE-MRI and DCE-CT exam, because we chose to use the standard diagnostic protocols that are in clinical use in our institute. Nevertheless, the impact of these differences on the AIFs are small at the level of the femoral arteries. Furthermore, the analyses of the measurement consistency (Table 3.2) and tracer kinetic model parameters (Table 3.3) are not influenced by these differences in injection protocol.

Second, we compared AIF_{PHASE} with AIF_{CT} , but did not carry out a direct validation of the measured concentration in the patients. For this, a comparison with arterial blood samples would be required, but this falls outside the scope of our study.

Third, when calculating K^{trans} values for the DCE-MRI and DCE-CT exams, we assume similar leakage behavior of the contrast agents in the prostate tissue. For DCE-MRI however, water exchange effects may play a role [38, 106], since the water molecules and not the contrast agent are the source of the signal. Nevertheless, we did not find significant differences in the K^{trans} values between DCE-MRI and DCE-CT. This is consistent with the findings of Bains *et al* [106].

Last, the phase drift of the B_0 -field of the scanner during image acquisition is a hardware problem and may lead to wrong AIF_{PHASE} measurements if not corrected for. Since phase drift is prevalent on scanners produced by the three most common vendors [107], efforts should be made to develop strategies to avoid or reduce phase drift during acquisition rather than correcting in the post-processing.

In conclusion, we showed that the measurement of an AIF from the DCE-MRI phase signal has good agreement in shape with an AIF measured with DCE-CT. Also, no differences were found in the K^{trans} values of healthy and cancerous prostate tissue between the DCE-MRI and DCE-CT exams. This shows that a reliable quantification of DCE-MRI data is feasible, when a patient-specific AIF is obtained from the phase signal. This may result in more consistent K^{trans} values between different exams, and possibly different institutes, thereby improving the quality of longitudinal and multi-center studies.

4

Chapter 4

Dynamic contrast-enhanced CT for prostate cancer: the relation between image noise, voxel size and repeatability

Abstract

The aim of this study was to evaluate the relationship between image noise, voxel size and voxelwise repeatability of a dynamic contrast-enhanced (DCE) CT exam for prostate cancer. This prospective study was approved by the local research ethics committee and all patients gave written informed consent. Twenty-nine patients (mean age of 69.1 years, range 56-80 years) with biopsy proven prostate cancer underwent two DCE-CT exams within one week prior to radiotherapy treatment. Parameter maps of transfer constant K^{trans} , the fraction of blood plasma v_p , the fraction of extravascular extracellular space v_e and the flux rate constant between the extravascular extracellular space and plasma k_{ep} were calculated at 15 different image resolutions, with kernel sizes ranging from 0.002 to 2.57 cc. Statistical analysis to quantify the voxelwise repeatability, was performed using a Bland-Altman analysis on all tracer kinetic model parameter maps of each patient. From this analysis, the within-voxel standard deviation (WSD) was calculated as a function of spatial resolution. A kernel size in the range of 0.1 to 0.3 cc yields reliable information. At 0.15 cc, the median WSD of K^{trans} , k_{ep} , v_p and v_e is 0.047 min^{-1} , 0.144 min^{-1} , 0.011 and 0.104 respectively. With increasing kernel size, these values reach stable levels of $\sim 0.02 \text{ min}^{-1}$, $\sim 0.05 \text{ min}^{-1}$, ~ 0.005 and ~ 0.05 respectively. In conclusion, there is a high voxelwise repeatability of the DCE-CT imaging technique for prostate cancer for kernel sizes as small as 0.1 cc. With the relationship between kernel size, image noise and voxelwise repeatability, it becomes possible to estimate for alternative DCE-CT protocols, for example with a reduced dose, at what kernel size a sufficient repeatability can be obtained.

A version of this chapter has been published as:

Dynamic contrast-enhanced CT for prostate cancer: relationship between image noise, voxel size, and repeatability.

J.G. Korpelaar, C.A.T. van den Berg, C.R.L.P.N. Jeukens, G. Groenendaal, M.R. Moman, P. Luijten, M. van Vulpen, and U.A. van der Heide

Radiology 2010; 256(3): 976-84

4.1 Introduction

Dynamic contrast-enhanced (DCE) imaging is frequently used for imaging prostate cancer [27-29, 41, 61, 78, 108]. In order to facilitate an accurate detection of small lesions as well as delineation of the tumor for focal therapies [13-16], high spatial resolution is required. DCE imaging for prostate is primarily performed using MRI [27-29, 41, 78, 108]. However, quantification of DCE-MRI data is difficult because of the complex relation between the signal intensity and the concentration of the contrast agent in tissue [46]. In particular, the determination of the arterial input function (AIF) required for tracer kinetic modeling, can be unreliable [49, 109, 110].

In contrast, the quantification of DCE-CT data is straightforward because of the linear relationship between Hounsfield units (H.U.) and contrast agent concentration. The feasibility to detect prostate tumors has been shown by Henderson *et al* [61]. Although in the past only a limited scan volume in craniocaudal direction was available, with modern multi-slice CT scanners sufficiently large slabs can be imaged at once, making DCE-CT of the entire prostate feasible.

For reliable identification of small lesions within the prostate it is crucial that they are detected consistently when the exam and analysis are repeated. The smallest detectable lesion size however, depends on the spatial resolution. Therefore, the purpose of our study was to evaluate the relationship between image noise, voxel size and voxelwise repeatability of a DCE-CT exam for prostate cancer.

4.2 Materials and methods

Patients

The prospective study was approved by the local medical ethical research board and all patients gave written informed consent prior to imaging. Thirty patients with biopsy proven prostate cancer underwent two DCE-CT exams and one MRI exam on different days within one week prior to radiotherapy. Only patients with localized prostate cancer (T1-3, G1-3, Nx/o, Mx/o) that did not have a contraindication for the CT contrast agent or fiducial markers in the prostate were included in this study. The repeatability could not be established for one patient due to technical failure of the CT scanner during one of the imaging sessions. The remaining 29 patients had a mean age of 69.1 (range 56–80) years, a mean Gleason score of 7 (range 6–9) and a mean pre-treatment PSA of 15.8 (range 4.3–59.0) ng/ml. T-stage varied from T1c to T4. Seven patients started hormonal therapy with a median of 10 (range 3-42) days prior to imaging. In patients with androgen deprivation hormonal therapy decreased perfusion values are reported [80]. Although the androgen deprivation was still active at the time of imaging, we did not exclude these patients from this study since no major fluctuations in blood flow between the two exams due to the hormonal therapy were expected.

Imaging protocol

DCE-CT imaging was performed on a 64-slice CT scanner (Philips Brilliance, 120kV, 200mAs, reconstruction with moderately smoothing filter B, reconstructed to 32 slices, voxel size 0.68 x 0.68 x 1.25 mm). In each patient the injection of iodine contrast agent (Ultravist 300, Schering AG, Berlin, Germany) with a power injector (60 ml, 6 ml/s) was followed by a saline flush (40 ml, 6 ml/s). An exam consisted of acquisitions at 42 time points within a time window of 5 minutes. The first 24 acquisitions were taken at 2.4 s intervals, the next 12 at a 10 s interval and the last 6 at 20 s intervals. The increase in time interval was done to reduce the radiation burden after the first minute.

We chose not to compromise the signal-to-noise ratio in advance. Therefore, the tube current was high compared to a regular diagnostic CT exam. The effective biological dose of the CT protocol was 1.3 mSv per time point, yielding a total dose of 54.6 mSv per exam. While this is a high dose for a diagnostic exam, it is negligible compared to the dose delivered in the subsequent radiation therapy treatment. A treatment dose of 77 Gy was given in the prostate with the intensity-modulated (IMRT) technique, which results in a skin dose of about 10 Gy.

Additional to the two DCE-CT exams an MRI exam at a 3T MR scanner (Achieva, Philips Medical Systems, Best, The Netherlands) was performed for the ROI analysis. The T_1 -weighted spin echo sequence (TR/TE 567/30 ms) and the T_2 -weighted turbo spin echo sequence (TR/TE 8400/120ms) consisted of 25 slices of 3 mm with 4 mm spacing between the slices. Both scans were acquired in the transverse plane, similar to the imaging plane of the DCE-CT scan.

Image processing

To remove motion artifacts within a DCE-CT exam, a local soft tissue registration was performed to register the CT acquisitions from all time points to the first. A rigid image registration algorithm [60] was used, with a correlation-based similarity measure, which is optimal for prostate registration on CT [111]. In two patients large deformations of the prostate occurred due to large differences in rectum volume [112]. Consequently, the rigid registration did not result in an accurate match between corresponding voxels. Because the validation of a non-rigid registration is unreliable, we chose to exclude these patients from the repeatability analysis.

To study the influence of the image resolution on the repeatability, we spatially convolved all volumes after image registration with 15 nearly isotropic 3D block kernels, ranging from 0.002 cc to 2.6 cc. To avoid boundary effects at the border of the prostate, only voxels where the entire 3D kernel lied within the prostate were used for the repeatability analysis. The repeatability was calculated only for the valid voxels of the largest kernel (2.6 cc), to ensure comparison between the same voxels at all resolutions.

The convolution of the images with a block kernel, as described in the previous paragraph, introduces a spatial correlation between adjacent voxels, since the underlying kernels overlap. While this results in parameter maps with small voxels, useful for delineation, it could in theory create a bias in the WSD. As a check, we also calculated the WSD_j (Equation 4.3) using only the voxels with adjacent kernels, avoiding overlap.

Noise analysis

As the repeatability of a DCE-CT exam depends on the image noise, the noise levels were determined for both scans and for each kernel in manually drawn regions of interest (ROI) in the left gluteus maximus (median volume 114 cc, range 82-149 cc). This muscle shows a typical enhancement pattern that remains at a steady level after a moderate increase in signal. For each voxel in the ROI the standard deviation of the signal intensity in Hounsfield units (H.U.) over the last 10 time points (± 140 seconds) was determined and averaged to obtain the average noise. To relate the kernel size to the noise level, the theoretical relation in Equation 4.1 was fitted to the mean noise level of both measurements from all patients to obtain the single voxel noise level in the raw data.

$$\text{noise level [H.U.]} = \frac{\text{single voxel noise level [H.U.]}}{\sqrt{\text{number of voxels}}} \quad [4.1]$$

For five patients noise analysis was not possible because they unintentionally moved in the scanner during image acquisition. As a result, the muscle tissue of the gluteus maximus deformed non-rigidly during image acquisition and no reliable noise level could be determined. These patients could be used for the rest of the study as the deformations of the muscle had no consequences for registration of the prostate.

Tracer kinetic model

The same image registration procedure as described for the prostate was followed for the iliac arteries, before obtaining the arterial input function (AIF). The AIF was derived from the non-convolved dataset, by averaging the AIF measured in the left and right iliac arteries. To correct for differences in large and small vessel hematocrit, the AIF was multiplied by a factor 1.2 as described by Henderson *et al* [61].

For quantitative analysis of the DCE-CT data we used the Generalized Kinetic Model as described by Tofts *et al* [25] with a blood plasma component (Equation 4.2).

$$C_{\text{tissue}}(t) = v_p \cdot AIF(t - \Delta) + K^{\text{trans}} \int_0^{t-\Delta} AIF(\tau) \cdot e^{\frac{-K^{\text{trans}}}{v_e}(t-\tau-\Delta)} d\tau \quad [4.2]$$

For each voxel and at every kernel size the fraction of blood plasma v_p ($0 \leq v_p \leq 1$), the volume transfer constant K^{trans} [min^{-1}], the volume of extravascular extracellular

space per unit volume of tissue v_c ($0 \leq v_c \leq 1$) and the flux rate constant between the extravascular extracellular space and plasma k_{ep} [min^{-1}] ($k_{ep} = K^{\text{trans}}/v_c$) were calculated. The delay (Δ) between the contrast bolus arrival in the artery and the tissue was determined by fitting the data with a range of delay values and choosing the delay with the best fit. Fitting was performed with an in-house developed computer program, written in the C++ programming language, using the C code for Feasible Sequential Quadratic Programming (CFSQP) package [113].

Repeatability analysis

For each patient a Bland-Altman analysis [67] was performed on the corresponding voxels from the two DCE-CT exams. In this way we calculated for each patient the within-voxel standard deviation (wSD) for all parameters and for all kernels. The wSD of a particular parameter P (e.g. K^{trans} or v_p) as defined by Bland and Altman [67], simplifies to the next equation in the case of two measurements:

$$wSD_j = \frac{1}{\sqrt{2}} \sqrt{\frac{1}{N-1} \sum_{i=1}^N (P_i^{CT1} - P_i^{CT2})^2} \quad [4.3]$$

with j being an individual patient, N being the total number of voxels within the prostate, and P_i^{CT1} and P_i^{CT2} being the parameter values of the i^{th} voxel of the first and second exam respectively. For each resolution we determined the median wSD, defined as the median of the wSD _{j} , and its variability (10th and 90th percentile of the wSD _{j}) across patients. Furthermore, we determined for each resolution the repeatability of the parameters as a function of the transfer constant (K^{trans}).

ROI analysis

To appreciate the within-voxel standard deviation (wSD), it is relevant to determine the range of parameter values that occur in prostate tumors and healthy tissue. With this information a wSD can be chosen that is small enough to discriminate between tumor and healthy tissue. Therefore, a ROI analysis was performed with the aid of all available clinical information including biopsy results. ROIs were drawn (M.R.M., three years experience in tumor delineation with multi-parametric prostate imaging) on a T_2 -weighted MR scan in hypointense regions suspected of tumor tissue (ROI_{susp}). With a T_1 -weighted MR scan we ensured that the low intensity of the T_2 -weighted MR scan was not caused by bleedings from the biopsy. To avoid including regions containing benign prostate hyperplasia, we only placed ROI_{susp} in the peripheral zone. Other ROIs were placed in contralateral peripheral zone regions that were not suspected of disease and in the central gland. As a reference, the ROIs of the gluteus maximus were used [73]. To transfer the ROIs that were delineated on MRI to the CT, we registered the MRI data to CT using a rigid image registration algorithm [60], using mutual-information as a similarity measure. For every ROI a mean enhancement curve was calculated and analyzed with the tracer kinetic model (Equation 4.2).

Statistical analysis

All statistical tests were performed with Matlab (The MathWorks, Inc., 2008, version 7.7.0.471, Natick, MA, USA) at the 5% significance level. To test for equal medians in the noise distributions of the paired DCE-CT exams, for every kernel the Wilcoxon signed rank test was used. The Wilcoxon rank sum test was used to investigate differences between the tracer kinetic model parameters of the four ROIs from the ROI analysis, corresponding to peripheral zone, central gland, ROI_{susp} and muscle. The same test was used to investigate the differences between the parameter values from the ROI analysis and the WSD_j of patients receiving hormonal therapy and not.

4.3 Results

Noise analysis

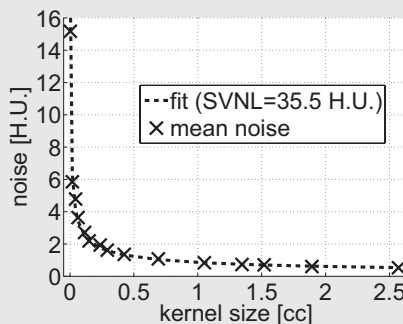
There were no significant differences in the noise distributions between the two exams in the 24 patients in whom noise was assessed. The single voxel noise level was on average 35.5 H.U. (Figure 4.1).

ROI analysis

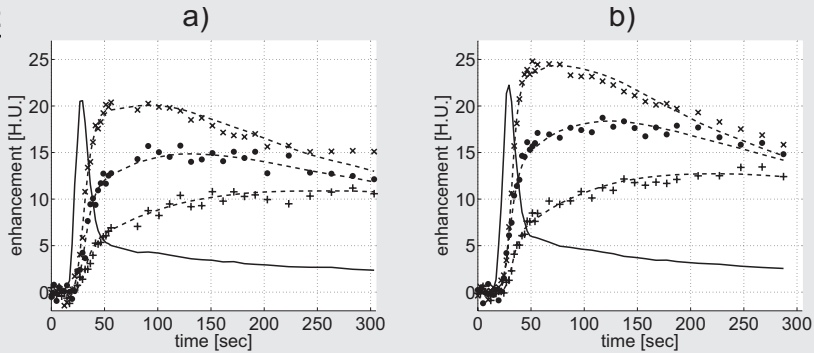
In one patient no clear region suspicious for disease (ROI_{susp}) could be found. In another patient the ROI of the central gland that was delineated on the T_2 -weighted MR scan was outside the imaging slab of the DCE-CT exam. The remaining ROIs that were delineated in the central gland (N=28), peripheral zone (N=29) and ROI_{susp} (N=28) had a median volume of 1.05 (range 0.03-2.38) cc, 0.71 (range 0.19-2.01) cc and 1.29 (range 0.31-3.79) cc respectively. Figure 4.2 shows an example of DCE-CT enhancement curves with the corresponding fits.

The K^{trans} values in ROI_{susp} have a broad range and overlap partly with the peripheral zone and central gland (Table 4.1 and Figure 4.3). Nevertheless, the K^{trans} values were significantly higher in ROI_{susp} compared to the healthy considered central gland ($p < 0.001$) and peripheral zone ($p < 0.001$). Parameter k_{ep} was also significantly higher in ROI_{susp} than in the central gland ($p = 0.004$) and peripheral zone ($p < 0.001$). In muscle tissue K^{trans} and v_e values were significantly lower than in the ROIs in the

Figure 4.1



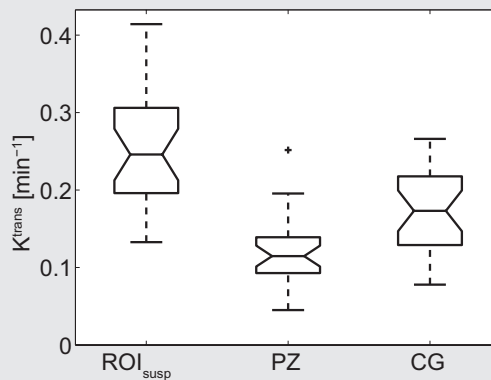
The noise level decreases with increasing kernel size, following the theoretical relationship of Equation 4.1. The single voxel noise level (SVNL) is on average 35.5 H.U. in the 24 patients in whom noise was assessed.

Figure 4.2


Enhancement curves of a 68-year old male from the ROIs in the central gland (+, 1.3 cc), peripheral zone (•, 2.0 cc) and ROI_{susp} (x, 3.3 cc) for the first (a) and second (b) DCE-CT exam. Fits are shown as dashed lines. The K^{trans} values of the second exam are slightly higher than the first exam (central gland 0.23 vs. 0.27 min^{-1} , peripheral zone 0.11 vs. 0.12 min^{-1} and ROI_{susp} 0.39 vs. 0.43 min^{-1}), while the other parameter values were comparable. The AIF (solid line) as shown has been reduced 10-fold as a scaling adjustment.

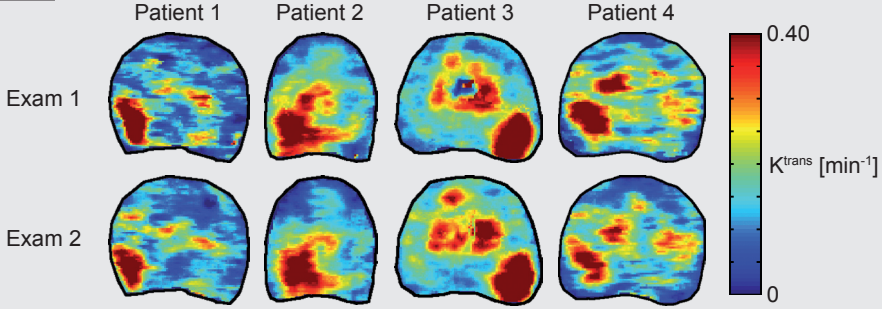
Table 4.1 Median values with 10th and 90th percentiles from the ROI analysis

(N=12)	ROI _{susp}	Peripheral zone	Central gland	Muscle
K^{trans} [min^{-1}]	0.24 (0.16 - 0.38)	0.11 (0.06 - 0.19)	0.17 (0.10 - 0.24)	0.04 (0.03 - 0.08)
k_{ep} [min^{-1}]	0.56 (0.28 - 1.05)	0.28 (0.13 - 0.65)	0.42 (0.16 - 0.60)	0.31 (0.10 - 0.63)
v_p	0.003 (0.000 - 0.025)	0.002 (0.000 - 0.0014)	0.005 (0.000 - 0.018)	0.002 (0.000 - 0.006)
v_e	0.455 (0.295 - 0.730)	0.390 (0.234 - 0.829)	0.435 (0.336 - 0.802)	0.140 (0.109 - 0.265)

Figure 4.3


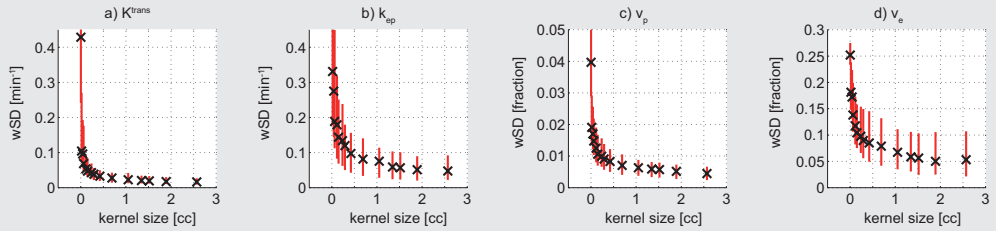
Box plots of the K^{trans} values from the ROI analysis from all patients in the region suspected for tumor (ROI_{susp}), peripheral zone (PZ) and central gland (CG). K^{trans} values were significantly higher in ROI_{susp} compared to the healthy considered peripheral zone ($p < 0.001$) and central gland ($p < 0.001$).

Figure 4.4



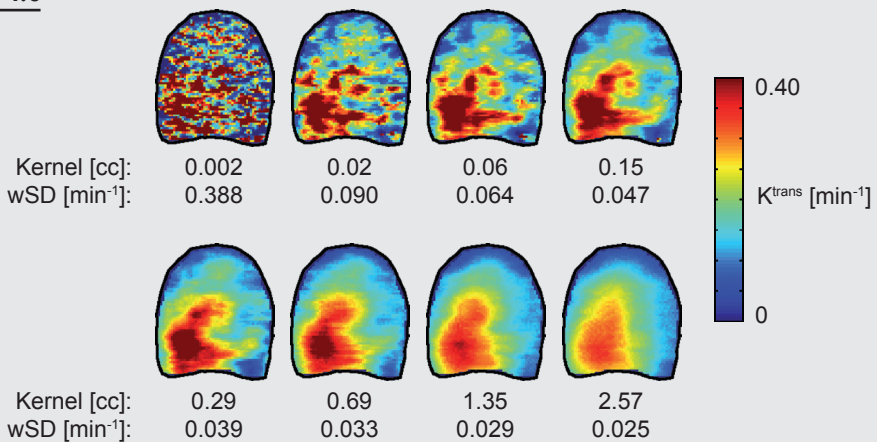
Examples of transverse slices of the 3D K^{trans} maps of the prostate at a kernel size of 0.15 cc for 4 male patients aged 67, 64, 68 and 73 years respectively. Similar K^{trans} patterns can be observed for all patients for both scans. The wSD_j of K^{trans} observed in these four patients at this resolution is 0.088, 0.047, 0.047 and 0.054 min^{-1} for patient 1 to 4 respectively.

Figure 4.5



The median within-voxel standard deviation (wSD , black crosses) is shown as a function of the kernel size with the 10th and 90th percentiles as red bars. The median wSD decreases for all parameters with increasing kernel size, reaching stable values of $\sim 0.02 \text{ min}^{-1}$ for K^{trans} , $\sim 0.05 \text{ min}^{-1}$ for k_{ep} , ~ 0.005 for v_p and ~ 0.05 for v_e .

Figure 4.6



K^{trans} maps from the prostate of a 64-year old male (patient 2 in Figure 4.4) for eight different kernel sizes and the corresponding wSD_j of K^{trans} for that patient.

prostate. Patients receiving hormonal therapy had a significant reduction in K^{trans} in the central gland ($p = 0.004$) compared to patients that did not receive hormonal therapy.

Repeatability analysis

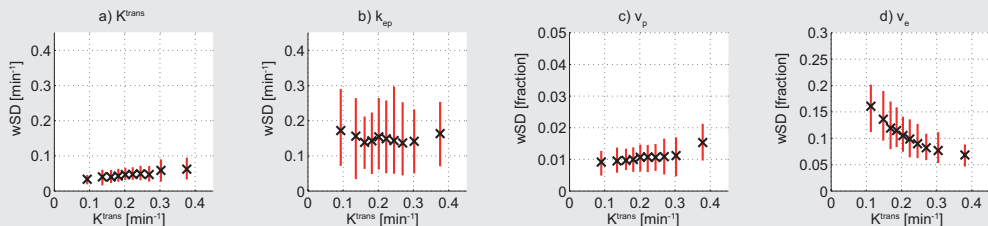
In the 27 patients from which the repeatability results were obtained, the mean prostate volume was 41.5 ± 9.8 cc of which a mean volume of 5.2 ± 2.5 cc was analyzed voxel-by-voxel for determining the wSD. Figure 4.4 shows four examples of transverse K^{trans} maps for both exams at a kernel size of 0.15 cc. High K^{trans} regions can be found in both the peripheral zone and central gland. The patterns of the transfer constant are very similar, but subtle differences can be observed between the two exams.

The median wSD of all parameters decreases with increasing kernel size (Figure 4.5). For kernels larger than about 1 cc the median wSD reaches stable levels of ~ 0.02 (0.01–0.03) min^{-1} for K^{trans} , ~ 0.05 (0.02–0.09) min^{-1} for k_{ep} , ~ 0.005 (0.002–0.007) for v_p and ~ 0.05 (0.02–0.11) for v_e . When comparing the shape of the graphs in Figure 4.5 with Figure 4.1, it can be seen that the median wSD behaves the same as the image noise. There were no significant differences in the wSD of the model parameters between the patients that did and did not receive hormonal therapy (for all kernel sizes $p > 0.056$, $p > 0.56$, $p > 0.072$ and $p > 0.19$ for K^{trans} , k_{ep} , v_p and v_e respectively).

The median wSD values for K^{trans} , k_{ep} , v_p and v_e of the spatially convolved data, as presented in Figure 4.5, give an average overestimation of 0.003 min^{-1} , 0.015 min^{-1} , 0.0005 and 0.010 respectively, compared to the method using adjacent kernels. This suggests that the bias in both approaches is small.

A kernel size between 0.1 and 0.3 cc yields reliable information, by avoiding too high noise levels and too low image resolution (Figure 4.6). At a kernel size of 0.15 cc, which is a reasonable result of the trade-off, the median wSD for K^{trans} , k_{ep} , v_p and v_e

Figure 4.7



The median wSD (black crosses) is shown as a function of the transfer constant (K^{trans}) at a kernel size of 0.15 cc, with the 10th and 90th percentiles as red bars. The median wSD of k_{ep} (b) is independent from K^{trans} , whereas the median wSD of v_e (d) decreases with increasing K^{trans} values. The median wSD of parameters v_p (c) and K^{trans} (a) slightly increases for higher K^{trans} values. However, the median wCV (= median wSD as fraction of mean parameter value) of K^{trans} decreases for increasing K^{trans} values.

are 0.047 (0.032-0.084) min^{-1} , 0.144 (0.069-0.251) min^{-1} , 0.011 (0.007-0.017) and 0.104 (0.075-0.158) respectively. The median WSD of parameter k_{ep} , which is physiologically the reciprocal parameter of K^{trans} , is about three times the median WSD of K^{trans} .

For high K^{trans} regions, the amplitude of the enhancement over time is larger than for low K^{trans} regions (Figure 4.2). As a result, a better signal-to-noise ratio is expected in high K^{trans} regions, which may lead to a better repeatability. Therefore we determined the dependency of the repeatability results on the transfer constant. Figure 4.7 shows that the median WSD of K^{trans} and v_p slightly increases with increasing K^{trans} values. In contrast, v_c tends to be lower at higher K^{trans} values, which was expected. This means that K^{trans} and v_p can be determined less and v_c more accurately in high flow regions. The repeatability of k_{ep} was not influenced by the K^{trans} value.

4.4 Discussion

With a multi-slice CT scanner a dynamic contrast-enhanced (DCE) measurement of the entire prostate was feasible, thereby obtaining information about the blood flow and vessel permeability within the prostate at a high spatial resolution. We quantified the voxelwise repeatability of the DCE-CT imaging technique for prostate cancer and established the relationship between signal-to-noise ratio, voxel size and repeatability. A trade-off must be made between the kernel size and the WSD to obtain an optimal image resolution for tumor delineation. On the one hand preservation of the anatomical shape of the tumor regions is crucial for tumor delineation. On the other hand, a WSD that is small relative to the difference between the mean K^{trans} value found in suspicious regions and in the peripheral zone and central gland is desirable.

The WSD is a measure of the repeatability and includes all uncertainties involved in the DCE-CT analysis. The first component of the WSD is independent from the kernel size and can be derived from the stable level that the WSD reaches at larger kernel sizes. It covers the day-to-day variations in patient anatomy and physiology and methodological aspects like image-registration. The size of this component is $\sim 0.02 \text{ min}^{-1}$ for K^{trans} , $\sim 0.05 \text{ min}^{-1}$ for k_{ep} , ~ 0.005 for v_p and ~ 0.05 for v_c . These values are small compared to the values observed with the ROI analysis except for v_p . This implies that the day-to-day variations in patients are very small, so that lesions in the prostate can be detected consistently. The second component is resolution-dependent and is mainly caused by the effect of image noise on the tracer kinetic model fitting. The single voxel noise level found in this DCE-CT study is similar to the results obtained by Jeukens *et al* [62].

The inter-subject range of K^{trans} values in ROI_{susp} is broader than in the healthy prostate regions analyzed. Compared to that broad range, the median WSD for K^{trans} at kernels of the order of 0.1 to 0.3 cc is small. At this spatial resolution, corresponding to cubic kernel sizes between 4.6 and 6.7 mm, the uncertainty in tumor detection will be mainly determined by the overlap in K^{trans} values and not by the measurement uncertainty.

This range of kernel sizes is similar to the minimal sizes reported for the correlation of prostate DCE-MRI with pathology [28, 114]. Furthermore, for focal radiotherapy it approaches the highest resolution at which dose modulation is practically feasible.

Repeatability studies of DCE-CT for ROIs in colorectal tumors and squamous cell carcinomas yield wcv (= wsd as fraction of mean parameter value) values ranging from 3 to 35% [115, 116], which is comparable to our results. A broader range of ROI-based repeatability values is reported for DCE-MRI. A wcv of 19.4–26.4% [73] is reported for normal tissues and for tumors it ranges from 8.5–57% [72, 117–119], depending on the site and parameter. Regarding the repeatability of DCE-MRI in prostate cancer, our results in terms of wcv are similar for K^{trans} , with a higher wsd for v_e [43, 118, 120]. Contrary to other studies [72, 73, 119], we found that the repeatability of parameter K^{trans} in terms of wcv is the same as v_e .

We found high K^{trans} regions in both the peripheral zone and central gland. In the peripheral zone this is highly indicative of tumor. However, in the central gland a high K^{trans} value may indicate tumor, but can also reflect benign prostate hyperplasia [114]. Henderson *et al* [61] reported results of a DCE-CT study of prostate cancer, analyzing the data with a distributed tracer kinetic model [121]. They found an average blood flow of 0.37 ± 0.12 ml/g/min in regions suspected of tumor tissue, so called hot spots. In cold spots, they found a blood flow of 0.18 ± 0.05 ml/g/min. These values cannot be directly compared with the transfer constant K^{trans} . However, they are in the same range as our values, if we assume that K^{trans} is flow-limited as a result of a high permeability of the vasculature [25]. With DCE-MRI a broad range in K^{trans} values is reported in healthy prostate tissue (0.06 – 0.74 min⁻¹) and in tumor areas (0.47 – 1.26 min⁻¹) [29, 41, 43, 108]. These differences in absolute K^{trans} values may be due to differences in imaging protocol and problems with absolute quantification [46, 49, 109, 110].

In the study by Henderson *et al* [61] the ROIs were directly delineated in the flow maps to depict hot spots. To avoid bias, we used T_2 -weighted MRI scans for ROI delineation, thereby being blinded for the outcomes of the DCE-CT analysis. Furthermore, we calculated one average curve for each ROI_{susp}, thus eliminating heterogeneity within the ROI. This may explain the somewhat lower K^{trans} values we found with our ROI analysis.

The radiation dose of the DCE-CT exams in this study is high, compared to conventional diagnostic CT scans. For lower kVp and mAs settings and a different amount of contrast agent, the wsd can be determined by measuring the noise level for that particular protocol. The data presented in this study can be used for other DCE-CT protocols to estimate the repeatability of tracer kinetic model parameters.

There are some limitations to this study. For the ROI analysis, we used all available information, T_1 - and T_2 -weighted MRI and biopsy results, to define regions suspected of tumor tissue. As the patients included in this study did not receive a

prostatectomy, but were treated with radiotherapy, a voxelwise spatial correlation between imaging and pathology was not feasible. As a result, a gold standard validation of the ROIs is not available. Importantly, this uncertainty has no impact on the relationship between image noise, voxel size and voxelwise repeatability.

Experimental conditions, such as the specific scanner used, may have an impact on the values of the parameters found from tracer kinetic model fitting. The reason we chose CT rather than MRI for this study, is that the quantification of the AIF and contrast enhancement is straightforward. The change in Hounsfield units is linear with the change in concentration of the contrast agent. This linearity can be assumed to be valid for other scanners and scan protocols. Differences in the choice of time points in the acquisition protocol can influence the accuracy with which model parameters are determined, and may lead to a bias [122, 123]. Changes in injection protocol may have a similar impact [77, 123, 124], even though the AIF is explicitly taken into account in the analysis. The differences in accuracy are expected to propagate into the repeatability of the exam.

In conclusion, there is a high voxelwise repeatability of the DCE-CT imaging technique for prostate cancer for kernel sizes as small as 0.1 cc. With the relation between kernel size, image noise and repeatability, it is possible to estimate for alternative DCE-CT protocols, for example with a reduced dose, at what kernel size a sufficient repeatability can be obtained.

5

Chapter 5

Tracer kinetic model selection for dynamic contrast-enhanced CT imaging of prostate cancer

Abstract

The aim of this study was to investigate the conditions under which the Tofts, extended Tofts and adiabatic approximation to the tissue homogeneity (AATH) model are the optimal tracer kinetic models (TKMs) for the quantification of DCE-CT exams in prostate cancer. This prospective study was approved by the local research ethics committee and all patients gave written informed consent. Twenty-nine patients (mean age, 69.1 years; range, 56-80 years) with biopsy proven prostate cancer underwent a DCE-CT exam prior to radiation therapy. TKM parameter maps were calculated for each patient with the Tofts, extended Tofts and AATH model. For each voxel, corrected Akaike's information criterion (AICC) values were calculated, taking into account both the goodness-of-fit and the number of model parameters. We consider the optimal model as the model with the lowest AICC. All three TKMs are the optimal model in part of the prostate. For individual patients, in 25.0 – 88.9% of the prostate voxels the AATH model was the optimal model, in 2.7 – 71.8% the Tofts and in 0.7 – 68.7% the extended Tofts model. The Tofts model is optimal in low flow regions ($<0.1 \text{ min}^{-1}$), the extended Tofts model in regions with high flow ($>0.4 \text{ min}^{-1}$) and low transit time ($<12 \text{ sec}$), and the AATH model in the intermediate flow range ($0.1 - 0.4 \text{ min}^{-1}$). However, differences between the three models are small and tracer kinetic model parameter estimates give consistent results between the three models. In conclusion, the three models all give reasonable fits of DCE-CT data from prostate. In view of the small parameter range in which the Tofts and extended Tofts model outperform the AATH model, the latter seems the optimal model for quantification of DCE-CT data of the prostate.

A version of this chapter has been published as:

Tracer kinetic model selection for dynamic contrast-enhanced computed tomography imaging of prostate cancer.

J.G. Korporeal, M. van Vulpen, C.A.T. van den Berg, and U.A. van der Heide
Investigative Radiology 2011; in press, DOI 10.1097/RLI.0b013e31821c0ea7

5.1 Introduction

With dynamic-contrast enhanced (DCE) CT and MR imaging the vascular properties of the prostate can be assessed. Since a high blood flow and vessel permeability are an indication for cancerous prostate tissue, this technique can be used for tumor detection [27, 28, 41]. With tracer kinetic models (TKMs) these vascular properties can be quantified, allowing characterization of the tumor. In general, a TKM describes the rate of accumulation and wash-out of an extracellular contrast medium in the extravascular extracellular space (EES). The delivery of the contrast agent to the prostate is reflected in the arterial input function (AIF). Using the enhancement curves in the prostate as a response on the AIF, an estimation of the tracer kinetic model parameters can be obtained [25, 26].

A number of different TKMs, with varying degrees of complexity, have been used to quantify the vascular properties of the prostate. The three most commonly used TKMs for quantification of DCE data from the prostate are the Tofts [28, 29, 41], extended Tofts [59, 125] and adiabatic approximation to the tissue homogeneity (AATH) model [27, 61, 62, 126], with respectively 2, 3 and 4 model parameters. For tumor detection, an important parameter for the Tofts and extended Tofts model is the volume transfer constant K^{trans} [28, 29, 41], which reflects both blood flow and vessel permeability [25]. The AATH model is a distributed parameter model and therefore able to separate the blood flow and vessel permeability into two single parameters [121].

The question arises which of these three TKMs is the optimal model for quantification of DCE data, under what conditions and how large the differences are. The prostate is an heterogeneous organ and may present a large variety of enhancement curves, reflecting for example healthy tissue, cancerous tissue, calcifications or benign prostate hyperplasia. Ideally, a TKM can describe the entire range of enhancement curves measured in the prostate. At the same time, a TKM should not be overly complex to avoid the calculation of model parameters that contain no information, so called 'overfitting'.

To determine which TKM is the optimal model, a number of simulation studies [122, 127] and patient studies [128, 129] have been performed on DCE-MRI for different tumor sites. However, with DCE-MRI not the contrast agent itself, but its effect on the surrounding water molecules is measured. As a consequence, water exchange effects may influence the signals from the different compartments that are accessible to the contrast agent [39, 40]. Although some studies report good similarity between DCE-MRI and DCE-CT results [63, 106], we chose to avoid potential bias due to water exchange effects and used DCE-CT exams in this study.

In a DCE-CT exam, the signal does not depend on the effective location of the contrast agent within the tissue. This makes it a more suitable technique than DCE-MRI to make a comparison between tracer kinetic models. Therefore, we analyzed in this study the DCE-CT exams from a group of 29 prostate cancer patients. The aim of

this study is to rank the performance of the Tofts, extended Tofts and AATH model for the quantification of DCE-CT exams in prostate cancer and investigate under what conditions each model performs optimally.

5.2 Materials and methods

Patients

The prospective study was approved by the local medical ethical research board and all patients gave written informed consent. We analyzed the data from a previously published DCE-CT repeatability study for prostate cancer [59]. In brief, twenty-nine patients with biopsy proven prostate cancer (T1c-T4, G1-3, Nx/o, Mx/o) underwent two DCE-CT exams on two different days within one week prior to radiotherapy. The first DCE-CT exam of each patient was used for this study. Only patients that did not have a contraindication for the CT contrast agent or fiducial markers in the prostate were included. The patients had a median age of 69 (range 56–80) years, a median Gleason score of 7 (range, 6-9), and a median pre-treatment prostate-specific antigen level of 12.0 (range, 4.3-59.0) ng/mL.

Imaging protocol

DCE-CT imaging was performed on a 64-slice CT scanner (Philips Brilliance, 120kV, 200mAs, reconstruction with moderately smoothing filter B, reconstructed to 32 slices, voxel size 0.68 x 0.68 x 1.25 mm). In each patient 60 ml iopromide (ULTRAVIST 300, Schering AG, Berlin, Germany) was injected with a power injector (6 ml/s), followed by a saline flush (40 ml, 6 ml/s). An exam consisted of acquisitions at 42 time points within a time window of 5 minutes. The first 24 acquisitions were taken at 2.4 s intervals, the next 12 at a 10 s interval and the last 6 at 20 s intervals. The increase in time interval was done to reduce the radiation burden after the first minute.

The effective biological dose was 1.3 mSv per time point, resulting in a total dose of about 54.6 mSv per exam. While this is a high dose for a diagnostic exam, it is negligible compared to the dose delivered in the subsequent radiation therapy treatment. A treatment dose of 77 Gy was given in the prostate with the intensity-modulated (IMRT) technique, which results in a skin dose of about 10 Gy.

Image processing

To remove motion artifacts within a DCE-CT exam, a local soft tissue registration was performed to register the CT acquisitions from all time points to the first. A rigid image registration algorithm was used [60], with a correlation-based similarity measure, which is optimal for prostate registration on CT [111]. To increase the signal-to-noise ratio (SNR), we spatially convolved all volumes after image registration with an isotropic 3D block kernel of 1.35 cm³. At this resolution, an average noise level of less than 1 H.U. was obtained [59]. To avoid boundary effects at the border of the prostate, only voxels where the entire kernel was located inside the prostate were used for the model comparison.

Tracer kinetic model fitting

The Tofts model yields two parameters and is defined as [25]:

$$C_{tissue}(t) = K^{trans} \int_0^{t-\Delta} AIF(\tau) e^{\frac{-K^{trans}}{v_c}(t-\tau-\Delta)} d\tau \quad [5.1].$$

For each voxel the volume transfer constant K^{trans} [min^{-1}] and the volume of extravascular extracellular space (EES) per unit volume of tissue v_c ($0 \leq v_c \leq 1$) were calculated. For all models, the delay (Δ) between the contrast bolus arrival in the artery and the tissue was determined by fitting the data with a range of delay values and choosing the delay with the best fit. This delay parameter is not considered part of the TKMs and its values are not reported.

The extended Tofts model is obtained when a parameter is added to the Tofts model to account for the blood volume:

$$C_{tissue}(t) = v_p \cdot AIF(t - \Delta) + K^{trans} \int_0^{t-\Delta} AIF(\tau) e^{\frac{-K^{trans}}{v_c}(t-\tau-\Delta)} d\tau \quad [5.2],$$

with v_p ($0 \leq v_p \leq 1$) as the fractional blood plasma volume.

Both the Tofts and extended Tofts model assume instantaneous mixing of the contrast agent over all compartments that are accessible for the contrast agent (v_c and v_p). In contrast, the adiabatic approximation to the tissue homogeneity (AATH) model is a distributed parameter model and defines the tracer concentration within v_p as a function of both the transit time (t_c) and the distance along the length of the capillary [121]. Therefore the AATH model separates the time course into a vascular phase ($t < t_c$) and a leakage phase ($t \geq t_c$). It is defined as:

$$C_{tissue}(t) = F_p \int_0^{t_c} AIF(t - \tau - \Delta) d\tau + E \cdot F_p \int_{t_c}^{t-\Delta} AIF(\tau) e^{\frac{-E \cdot F_p}{v_c}(t-\tau-t_c-\Delta)} d\tau \quad [5.3],$$

It has the theoretical advantage that the plasma flow (F_p) can be distinguished from the extraction fraction E ($0 \leq E \leq 1$). As described by others [62, 127, 130], we increased the stability of the fitting algorithm by using 15 discrete values for t_c ($5 < t_c$ [s] < 75), after which the best fit was chosen. All model parameters were calculated by minimizing the objective value (objValue), which is defined as:

$$objValue = \sqrt{\sum_{i=1}^n \frac{(y_i - f(\theta_i))^2}{n}} \quad [5.4].$$

The number of time points n is 42, y_i is a vector with the 42 data points of voxel i , and $f(\theta_i)$ is the model fit for voxel i with the parameters of the corresponding model defined in θ_i . All data points were weighted equally. Voxels with an evidently poor fit, e.g. in regions of a transurethral resection of the prostate (TURP), were excluded from the analysis.

In each patient an arterial input function (AIF) was derived from the non-convolved dataset, by averaging the AIF measured in the left and right femoral arteries. To correct for differences in large and small vessel hematocrit, the AIF was multiplied by a factor 1.18, based on a hematocrit of 0.38 and a small to large vessel ratio of 0.7 [26, 61].

All models were fitted with in-house developed computer programs, written in the C++ programming language, using the C code for Feasible Sequential Quadratic Programming (FQSQP) package [113]. This algorithm has been extensively tested and proved to be insensitive to the initial starting values of the nonlinear regression. All data were weighted equal and the regression was stopped 1) when the stepsize was smaller than the machine precision, 2) when a new iterate was essentially identical to the previous iterate or 3) when no solution was found within the maximum of 100 iterations. Although we did not keep track of the third case in which no solution was found, we did not find any inconsistencies in the objective value maps.

Model comparison

For the comparison of the three TKMs, we used the same approach as described by Brix *et al* [131]. The three tracer kinetic models described above form a set of candidate models to quantify DCE data. We consider the optimal model as the model with the smallest possible number of parameters for adequate representation of the data. Therefore, for each voxel Akaike's information criterion (AIC) was calculated and corrected for small sample sizes (AICC) [132]:

$$AICC = n \cdot \ln(objValue^2) + 2K + \frac{2K(K+1)}{n-K-1} \quad [55].$$

In this equation n is the number of time points per enhancement curve and K the number of parameters per model. K yields values of 3, 4 and 5 for the Tofts, extended Tofts and AATH model respectively, including one parameter for the variance [132]. The first term takes the goodness of fit into account, the second adds a penalty term for every additional parameter and the third is the correction for small sample sizes, which is advocated in cases where the ratio $n/K < 40$ [132]. Based on the AICC values, for each voxel the optimal model was chosen by selecting the minimum AICC ($AICC_{min}$).

To assess the relative likelihood of a model, we calculated the AICC differences between models, Δ_m , as:

$$\Delta_m = AICc_m - AICc_{\min} \quad [5.6],$$

with $AICc_m$ being the AICC value of candidate model m . For each model out of the set of R candidate models the Akaike weight, w_m , was calculated from Δ_m [132]:

$$w_m = \frac{\exp(-\Delta_m / 2)}{\sum_{r=1}^R \exp(-\Delta_r / 2)} \quad [5.7].$$

The values of w_m represent the weight of evidence in favor of a certain model compared to the other candidate models.

In clinical practice, a single model will be chosen to analyze the data. To assess the impact of a particular choice, we investigated the interchangeability of the K^{trans} values between the different models. If one would use the AATH model for analysis, a K^{trans} value can be derived from the parameters F_p and E or a combination of both. Similarly, when using one of the Tofts models, parameter K^{trans} reflects F_p , E or a combination of both. This depends on the conditions under which the contrast agent leaks out of the vessels into the EES. Under flow-limited conditions K^{trans} equals F_p , under permeability-limited conditions K^{trans} equals $ps (= -F_p * \ln(1-E))$, and in the mixed flow- and permeability condition in between, K^{trans} equals $E * F_p$ [26]. We chose to analyse all three conditions for the subset of voxels in which each of the three candidate models performed best. In this way, we determined how a K^{trans} value should be derived from the TKM parameters of the AATH model and how K^{trans} values from the Tofts models should be interpreted.

To assess the linearity between the parameter estimates of v_e between the three models, we calculated Pearson's correlation coefficients and calculated the average differences in v_e between the models.

Statistical analysis

With the addition of parameters to a model, the fit should become better. To verify this, we compared the objValues of the three models with a paired Wilcoxon signed rank test and report the number of voxels in which this was not the case. Because of the restricted parameter range of v_e , v_p and E we quantified the percentage of voxels that has the minimum or maximum value of the parameter range, so called 'clipping'. For each voxel, the optimal TKM was selected based on the minimum AICC value. We calculated the percentage of voxels in which the Tofts, extended Tofts and AATH model yielded the minimum AICC. These percentages were calculated for all voxels together and for the individual patients. To verify that each model parameter represents a different property, Spearman's rho was calculated between the model parameters of the single models.

5.3 Results

Figure 5.1 shows an overview of all parameter maps that were analyzed for a single patient. The objValue maps were converted into AICc maps with the use of Equation 5.5. Based on these AICc maps, an $AICc_{min}$ map could be calculated, reflecting which model yields the lowest AICc value per voxel.

In total 446,219 voxels were analyzed for the model comparison. Table 5.1 summarizes the parameter values observed in these voxels when calculated with each of the models. The paired differences in AICc between the Tofts and extended

Figure 5.1

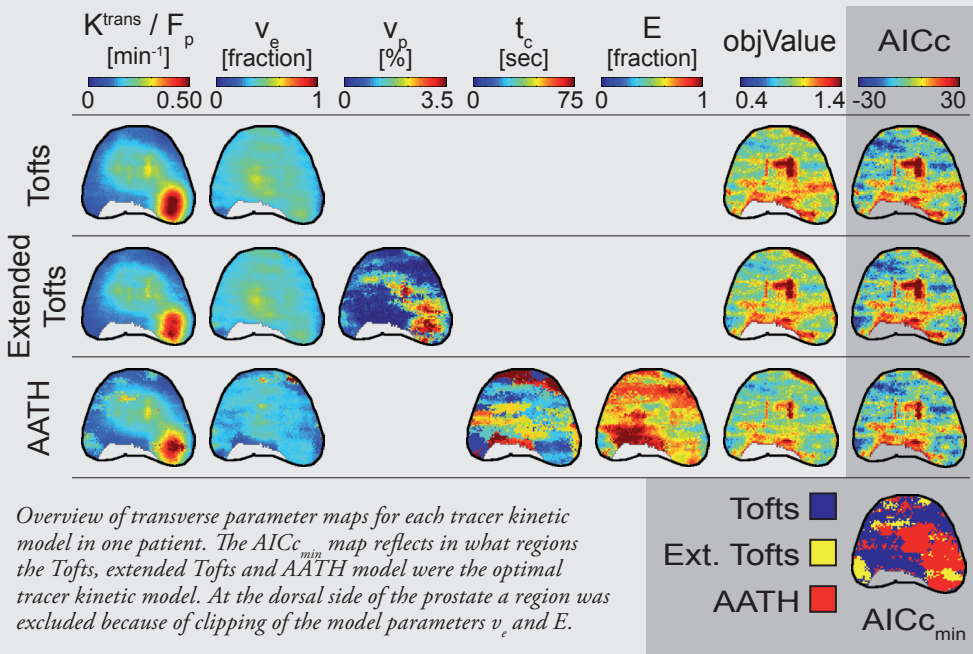


Table 5.1 Median with 95% CI of the TKM parameters of all analyzed voxels

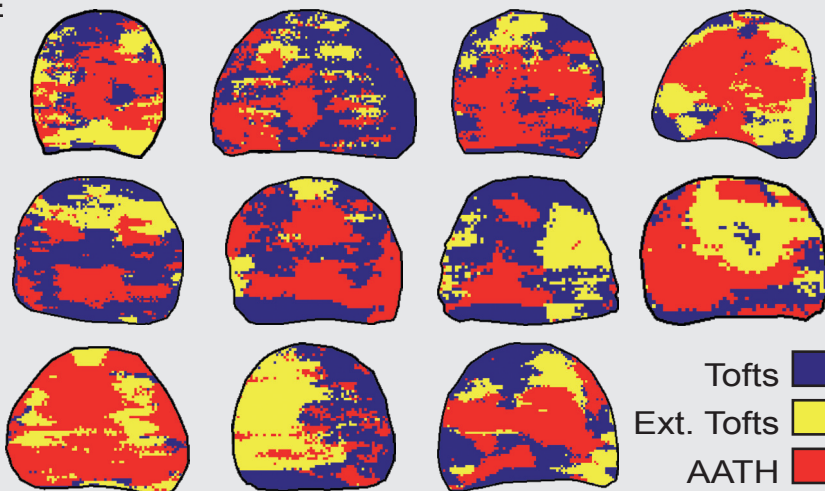
(N=446,219)	K^{trans} / F_p [min^{-1}] ^p	v_e [fraction]	v_p [%]	t_c [sec]	E [fraction]	objValue	AICc
Tofts	0.20 (0.08-0.37)	0.46 (0.25-1.00)				1.271 (0.766-2.277)	26.8 (-15.7-75.7)
Ext. Tofts	0.19 (0.07-0.34)	0.46 (0.25-1.00)	0.7 (0.0-3.4)			1.212 (0.750-2.136)	25.2 (-15.0-72.8)
AATH	0.19 (0.08-0.47)	0.42 (0.21-1.00)		30 (5-75)	0.70 (0.34-1.00)	1.119 (0.703-1.984)	21.1 (-18.0-69.2)

Tofts model, as defined in Equation 5.6, have a median of -1.7 (range $-7.7 - 94.2$). The paired differences in $AICc$ between the Tofts and AATH model have a median of 1.9 (range $-5.9 - 81.5$) and between the extended Tofts and AATH model a median of 1.8 (range $-32.4 - 76.8$).

The paired Wilcoxon signed-rank test showed significantly better fitting of the extended Tofts model compared to the Tofts model ($p < 0.001$) and for the AATH model compared to the extended Tofts model ($p < 0.001$). So, as expected, the objValue became better with the addition of model parameters. In 10.8% of all voxels the extended Tofts model had a worse fit than with the Tofts model. The AATH model had in 0.1% a worse fit than the Tofts model and in 9.9% a worse fit than the extended Tofts model. In theory, a more complex TKM should only give better fits than a less complex model. However, the fitting algorithm has finite accuracy. Furthermore, the differences in objValue in these cases were extremely small with a median of 0.005 , which is insignificant with respect to the observed objValues (Table 5.1) and the size of the penalty term (Equation 5.5) for each additional model parameter. Therefore, this did not lead to bias in the $AICc$ values based on which the optimal model was selected.

For the Tofts and extended Tofts model, respectively 5.0% and 5.7% of the voxels clipped to the maximum v_c value. This occurred in voxels with low K^{trans} values, yielding a median (with 95% CI) of 0.13 ($0.04 - 0.20$) min^{-1} and 0.12 ($0.03 - 0.20$) min^{-1} respectively. For the AATH model, 7.8% of all voxels clipped to the maximum v_c value, 3.2% clipped to the maximum E value and 2.8% clipped to both the maximum v_c and maximum E value. This occurred in low flow voxels with a median (with 95% CI) of 0.12 ($0.06 - 0.22$) min^{-1} . In 42.8% of the voxels that clipped to the maximum E value, the Tofts model yielded the lowest $AICc$ value.

Figure 5.2

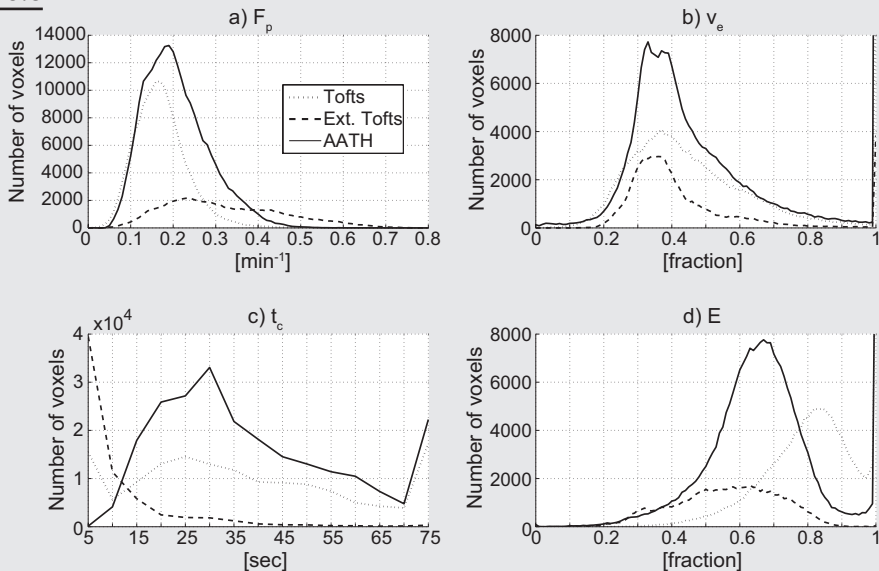


Examples of transverse slices of $AICc_{min}$ maps in 11 patients.

Even though the AIC_{\min} maps were calculated per voxel, in each patient a heterogeneous pattern of contiguous regions was observed, as illustrated in Figure 5.2. In none of the patients, one single model was the optimal model. The AATH model was optimal in 53.6% of all voxels, and Tofts in 33.3% and extended Tofts in 13.2%. For individual patients, in a range of 25.9 – 88.9% of the prostate the enhancement curves were optimally fitted with the AATH, in 2.7 – 71.8% with the Tofts and in 0.7 – 68.7% with the extended Tofts model. In the voxels where the Tofts, extended Tofts and AATH model were the optimal model, they yielded median Akaike weights (with 95% CI) of 59.9%, (42.3 – 71.7%), 66.1% (40.8 – 99.6%) and 89.1% (44.2 – 100.0%) respectively. Within the single models, the correlations between parameters are weak with a Spearman's rho between -0.35 and 0.28, except for the AATH parameters flow and t_c , with a Spearman's rho of -0.67.

As shown before, in none of the patients one of the three models is the optimal model in all voxels. Therefore, it is useful to investigate under which circumstances each model performs best. Figure 5.3 shows for each parameter of the AATH model the number of voxels in which the Tofts, extended Tofts and AATH model were the optimal model. Voxels with a high flow value ($>0.4 \text{ min}^{-1}$) and a low t_c ($<12 \text{ sec}$), are in most cases best fitted with the extended Tofts model. This is consistent with the Spearman's rho of -0.67 between flow and t_c . From all voxels with a midrange flow value ($0.1 \text{ min}^{-1} < \text{flow} < 0.4 \text{ min}^{-1}$), about 60% is best fitted with the AATH model, whereas for the very low flow values the Tofts model fits most voxels best. For parameter E, most voxels with an E value higher than 0.8 are best fitted with the Tofts model.

Figure 5.3

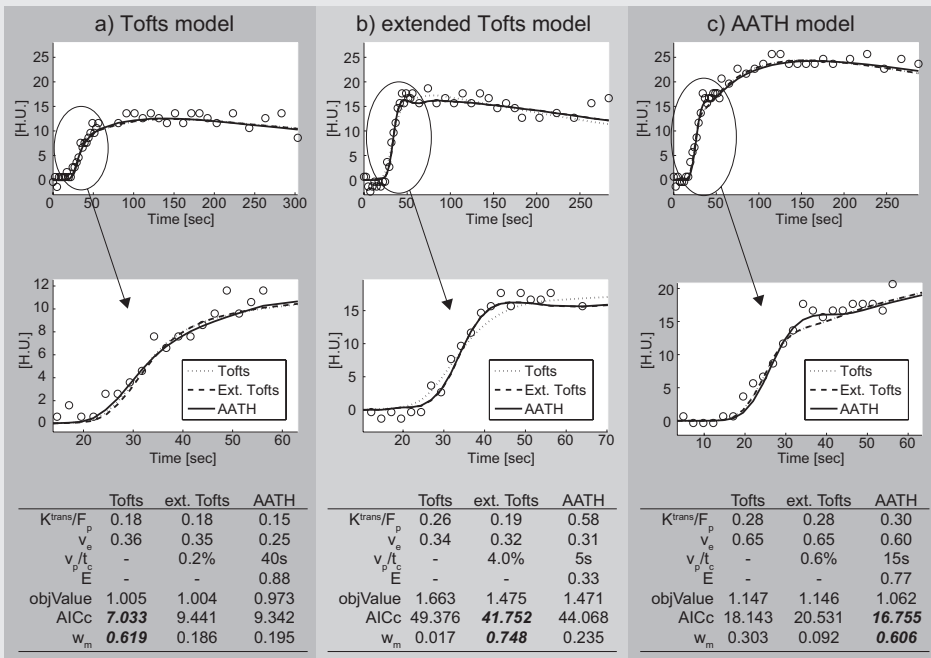


Histograms showing for every parameter value of the AATH model what the number of voxels is that is best fitted with the Tofts, extended Tofts and AATH model.

Based on the results of Figure 5.3, three example curves that are characteristic for the circumstances under which each model is the optimal model are presented in Figure 5.4. In the first case, all three models give about the same fit as reflected by the small differences in objValue (Figure 5.4a). Although the 4-parameter AATH model gives the best objective value, the Tofts model has only 2 parameters and has therefore the lowest AICC. In the case where the extended Tofts model is the optimal model (Figure 5.4b), the fits of the extended Tofts model and AATH model are essentially the same. Again, because of less parameters in the extended Tofts model, the corresponding AICC is lower than for the AATH model. Note that the Tofts model is unable fit the steep upslope. In Figure 5.4c the AATH model is the optimal model, whereas the Tofts and extended Tofts model give essentially the same fit. The gain in objValue is apparently that large, that the use of a 4-parameter model is justified.

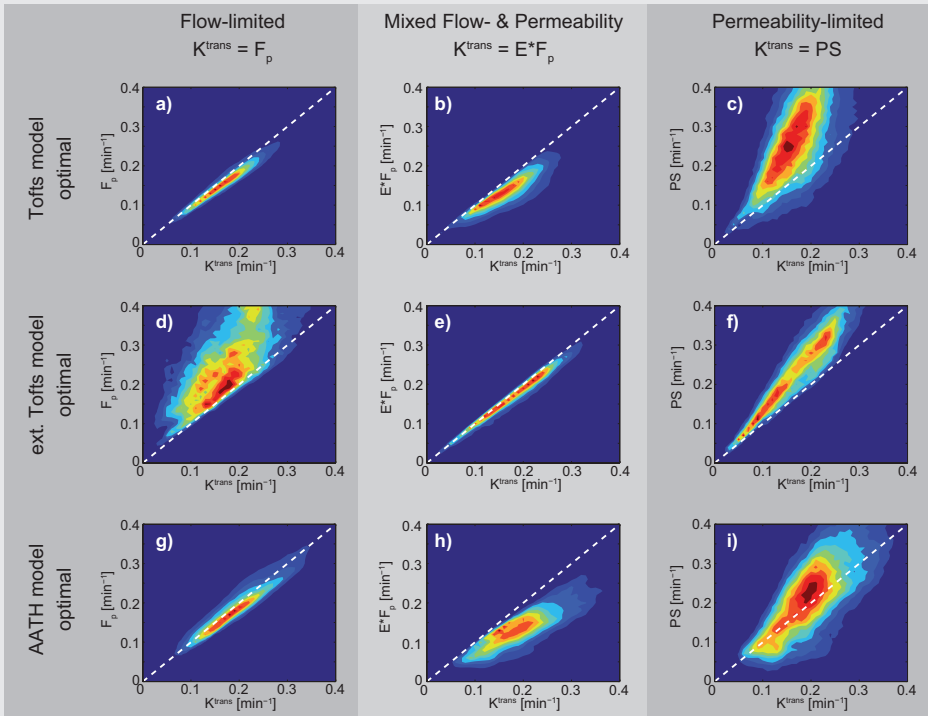
In clinical practice, a single model will be chosen to analyze the data. To assess the interchangeability of K^{trans} , Figure 5.5 shows the distributions of the calculated and derived K^{trans} values, based on the possible flow- and permeability conditions in the prostate tissue. In voxels where the Tofts and AATH model are optimal, 86.9% in total, the flow-limited condition is appropriate (Figure 5.5a and 5.5g). For voxels where the extended Tofts model is optimal, 13.2% in total, the tissue is under the mixed flow- and permeability condition (Figure 5.5e).

Figure 5.4



Example curves that represent the particular conditions under which the Tofts (a), extended Tofts (b) and AATH model (c) perform best.

Figure 5.5



Distributions of the calculated and derived K^{trans} values, under the three different flow- and permeability conditions. In the voxels where the AATH model was optimal (g-i), the derived K^{trans} values were compared with the calculated K^{trans} values from the Tofts model in the same voxels.

The estimates of parameter v_e were almost identical between the two Tofts models, with a Pearson's correlation larger than 0.94 and a mean difference less than 0.005. The v_e estimates of the AATH model had in general lower Pearson's correlations ($0.67 < r < 0.86$) and gave an average underestimation of 0.04 compared to the Tofts models. This underestimation is about 10% of the mean v_e value (Table 5.1).

5.4 Discussion

For quantification of dynamic contrast-enhanced (DCE) data, different tracer kinetic models (TKMs) have been used. This study addresses the question which of three TKMs is the optimal model for quantification of DCE data, under what conditions and how large the differences are. A trade-off was made between the increase in goodness-of-fit and the addition of model parameters, as quantified with ΔICC . We have shown that neither the Tofts, extended Tofts or the adiabatic approximation to the tissue homogeneity (AATH) model can be regarded as the optimal model. However, differences between the three models are small and tracer kinetic model parameter estimates give consistent results between the three models. Therefore, the choice for one or the other TKM does not seem critical in clinical practice.

All investigated TKMs performed as expected: the addition of model parameters resulted in a better goodness-of-fit in a majority of voxels. Clipping of model parameters mainly occurred in low flow and low K^{trans} regions. This is presumably a result of a lower signal-to-noise ratio (SNR) in these enhancement curves. Clipping could have been avoided by increasing the parameter range for v_c and E , but we chose to restrict the parameter range between 0 and 1 to circumvent the calculation of physically incorrect parameter values.

The AIC_{min} maps in all patients reflected a heterogeneous pattern with contiguous regions in which one of the models outperformed the others. This suggests that the heterogeneity is not caused by noise, but that it reflects the underlying properties of the vasculature. To investigate this further, we determined how the model with minimal AIC depended on the parameter values of the AATH model. In the limit of a low flow ($<0.1 \text{ min}^{-1}$), the enhancement curves are best described by the Tofts model. Here the signal enhancement is relatively low and AATH model parameters such as v_c and E clip frequently against their maximum boundaries. The slightly better fit of the more complex models is not justified by AIC.

In the limit of a high flow ($>0.4 \text{ min}^{-1}$) and short t_c ($<12 \text{ sec}$), the enhancement curves are best described by the extended Tofts model. It was observed in this study as well as earlier [62], that flow and t_c are negatively correlated. This is consistent with the central volume principle, by which flow and transit time are necessarily correlated. At high flow levels, the transit time t_c becomes short. As a result, the approximation of instantaneous mixing in the extended Tofts model becomes valid.

In the intermediate flow range ($0.1 - 0.4 \text{ min}^{-1}$), the AATH model is the optimal model because most voxels are fitted optimally with this TKM. These findings show, that while the AATH model is well capable of fitting the enhancement curves in all observed flow ranges, its complexity is not required in low- and high-flow regions. This is in agreement with a theoretical study on the interpretation of the Tofts models. It was shown that the Tofts and extended Tofts models are only accurate in weakly vascularised tissues with a small v_p , and that the extended Tofts model is additionally accurate in highly perfused tissues with a high blood flow [133].

We found that the majority of voxels is under flow-limited conditions. This is in accordance with studies that found the prostate to be hypoxic, whether in benign or cancerous tissue [134]. In contrast, the voxels that were optimally fitted with the extended Tofts model are under the mixed flow- and permeability condition. This difference may be directly related to the higher flow values found in these voxels (Figure 5.3a). This implies, that when using the AATH model, K^{trans} equals $F_p * E$ in voxels with high flow and low t_c values. In other voxels, K^{trans} can be interpreted as F_p .

Similar to our results, Naish *et al* found in a DCE-MRI study of lung tumors that the AATH model in most cases gave the best description of the data [128]. In that study however, the temporal resolution of 4 seconds was insufficient to separate the

flow and extraction parameters from the AATH model. This is in agreement with a simulation study on the temporal resolution of DCE-MRI data in combination with the AATH model [135]. Donaldson *et al* report that in a group of 30 cervical cancer patients a 2-compartment exchange model is better suited for the analysis than the extended Tofts model [129]. They report a correlation for v_e between the extended Tofts and AATH model of 0.72, which is lower than our finding. Whereas the correlation they report between flow and K^{trans} is high (0.94), they found substantial differences between the flow and K^{trans} values. This may be related to the complex relation between contrast agent and DCE-MRI signal or to differences in flow and permeability conditions at other tumor sites.

This study has some limitations. First, we ranked the three TKM according to their AIC values, but other considerations than the goodness-of-fit and the number of model parameters may play a role when selecting an appropriate TKM. For example, the increased calculation time with more model parameters may be an important issue in clinical practice. However, methods have been developed to reduce the calculation time of the TKM parameters [136, 137]. Second, the fixed kernel size that was chosen in this study directly influences the noise levels in the enhancement curves and the corresponding AIC values and thus the outcome of this study. For clinical practice, smaller kernel sizes may be preferred to increase the spatial resolution, but this comes at a cost of increased noise levels [59]. Jeukens *et al* studied the impact of image noise on the fitted model parameters. They found that for a noise below 4 Hounsfield units (H.U.), the parameters of the AATH model could be well determined for flow values above 0.15 min^{-1} [62]. In the data presented in this study, we have a noise level of about 1 HU. Third, the parameter space of the TKMs investigated in this study are limited to the enhancement curves that were found in the prostate. For other tumor sites, e.g. cervix, breast and head-and neck tumors, the choice for a particular TKM may be more critical. Fourth, with the data presented in this study, it would be possible to calculate model-averaged parameters using multimodal inference, as described by Brix *et al* [131]. In view of the consistent results in model parameters between the three TKMs, we did not perform this analysis.

In conclusion, we showed that none of the three models is consistently the optimal model in any patient. All models give reasonable fits and the differences in fits between the Tofts, extended Tofts and AATH model are small. Strong correlations exist between the tracer kinetic model parameters of the three models. Therefore, the choice for one or the other model is not critical for clinical practice. In view of the small parameter range in which the Tofts and extended Tofts model outperform the AATH model, the latter seems the optimal model for quantification of DCE-CT data of the prostate.

6

Chapter 6

The use of probability maps to deal with the uncertainties in prostate cancer delineation

Abstract

The use of dynamic contrast-enhanced (DCE) imaging for delineation of prostate tumors, requires that decisions are made on a voxelwise basis about the presence of tumor. While the sensitivity and specificity of this technique are high, we propose a probabilistic approach to deal with the intrinsic imaging uncertainty. Twenty-nine patients with biopsy-proven prostate cancer underwent a DCE-CT exam prior to radiotherapy. From a logistic regression on K^{trans} values from healthy and diseased appearing prostate regions we obtained a probability function for the presence of tumor. K^{trans} parameter maps were converted into probability maps and a stratification was applied at the 5% and 95% probability level, to identify low-, intermediate- and high-risk areas for the presence of tumor. In all patients, regions with high, intermediate and low risk were identified, with median volume percentages of 7.6%, 40.0% and 52.1% respectively. The contiguous areas that resulted from the voxelwise stratification can be interpreted as GTV, high-risk CTV and CTV. In conclusion, K^{trans} parameter maps from a DCE-CT exam can be converted into probability maps for the presence of tumor. In this way, the intrinsic uncertainty that a voxel contains tumor can be incorporated into the treatment planning process.

A version of this chapter has been published as:

The use of probability maps to deal with the uncertainties in prostate cancer delineation.
J.G. Korporaal, C.A.T. van den Berg, G. Groenendaal, M.R. Moman, M. van Vulpen, and U.A. van der Heide
Radiotherapy and Oncology 2010; 94: 168-172

6.1 Introduction

Dynamic contrast-enhanced (DCE) imaging is frequently used for the detection of prostate tumors [27-29, 41, 108, 114, 138-140] and is beginning to be used within the context of a radiotherapy treatment and follow-up [81, 82, 141]. After injection of a bolus of contrast agent into the blood stream, the behavior of the contrast agent in the prostate can be measured by repetitive imaging of the prostate. By fitting a tracer kinetic model to DCE data the transfer constant K^{trans} can be calculated, which reflects blood flow and vessel permeability. Validation of DCE-MRI with pathology has shown an increase in K^{trans} values in prostate tumors compared to healthy prostate tissue [27, 29, 41, 108, 114]. Reported values for sensitivity and specificity of DCE-MRI for prostate cancer are high and range from 73-93% and from 74-96% respectively [28, 108, 138-140]. Therefore, the DCE technique is particularly attractive for the purpose of tumor delineation for focal therapies, like dose escalation with a micro-boost [13-16].

Delineating a prostate tumor essentially comes down to a voxelwise decision whether a voxel contains tumor or not. There are however two problems that make an accurate tumor delineation difficult. First, the sensitivity and specificity of the DCE technique are not perfect, limiting the predictive power for the presence of tumor. This is for example reflected in an overlap in K^{trans} values between tumor areas and healthy prostate tissue [29, 61, 108]. If a voxel has a K^{trans} value in this overlap range, a reliable decision cannot be made. Second, by definition no detailed spatial verification of imaging with pathology can be obtained from patients scheduled for radiation therapy. In the clinical practice of radiotherapy treatment planning this means that there will never be a ground truth when delineating a prostate tumor.

For this reason, we have to develop methods that deal with these intrinsic imaging uncertainties and the lack of a ground truth for prostate tumor delineation. In this study we propose a method to incorporate the uncertainty that a voxel contains tumor into the tumor delineation process. We convert DCE imaging data into probabilities for the presence of tumor and translate this probabilistic information into GTV and CTV concepts, which are commonly used in radiotherapy treatment planning. To illustrate this approach, we use DCE-CT as functional imaging technique. It has been used to image tumors in the prostate [61, 62] and to monitor radiation therapy treatment response [142, 143].

6.2 Materials and methods

Patients

Twenty-nine patients with biopsy proven prostate cancer underwent a DCE-CT exam and an MRI exam prior to radiotherapy. The study was approved by the local research ethics board and all patients gave their informed consent prior to imaging. The patients had a mean age of 69.1 (range 56–80) years, a mean Gleason score of 7 (range 6–9), a mean pre-treatment PSA of 15.8 (range 4.3–59.0) ng/ml and T-stages varying from T1c to T4. Ten patients started androgen deprivation hormonal therapy (HT) prior to imaging.

Imaging protocol

DCE-CT imaging was performed on a 64-slice CT scanner (Philips Brilliance, 120kV, 200mAs, reconstruction with moderately smoothing filter B, reconstructed to 32 slices, voxel size 0.68 x 0.68 x 1.25 mm). The injection of the iodine contrast agent (Schering Ultravist 300) with a power injector (60 ml, 6 ml/s) was followed by a saline flush (40 ml, 6 ml/s). A total of 42 acquisitions were made, subdivided by 24 time intervals of 2.4 seconds, followed by 12 and 6 acquisitions with time intervals of 10 and 20 seconds respectively, to reduce the radiation burden. The total scan time of 5 minutes was sufficient to measure the wash-out of the contrast agent.

The effective biological dose of the CT protocol was 1.3 mSv per time point, yielding a total dose of 54.6 mSv per exam. While this is a high dose for an exam in a diagnostic setting, it is negligible compared to the dose delivered in the radiation therapy treatment. A treatment dose of 77 Gy was given in the prostate with the intensity-modulated (IMRT) technique, which results in a skin dose of about 10 Gy.

Image processing

To correct for motion during image acquisition a local soft tissue registration was performed with a rigid image registration algorithm [144] using a correlation-based similarity measure, which is optimal for prostate registration on CT [111]. We spatially convolved all volumes after image registration with a nearly isotropic 3D block kernel of 0.15 cc.

The same image registration procedure as described for the prostate was followed for the iliac arteries, before obtaining the arterial input function (AIF). The AIF was derived from the non-convolved dataset, by averaging the AIF measured in the left and right iliac arteries. To correct for differences in large and small vessel hematocrit, the AIF was multiplied by a factor 1.2 as described by Henderson *et al* [61].

For quantitative analysis of the DCE-CT data we used the Generalized Kinetic Model as described by Tofts *et al* [25] with a blood plasma component:

$$C_{tissue}(t) = v_p \cdot AIF(t - \Delta) + K^{trans} \int_0^{t-\Delta} AIF(\tau) \cdot e^{-\frac{K^{trans}}{v_e}(t-\tau-\Delta)} d\tau \quad [6.1].$$

For each voxel the fraction of blood plasma v_p ($0 \leq v_p \leq 1$), the volume transfer constant K^{trans} (min^{-1}), the volume of extravascular extracellular space (EES) per unit volume of tissue v_e ($0 \leq v_e \leq 1$) and the flux rate constant between EES and plasma k_{ep} (min^{-1}) ($k_{ep} = K^{trans}/v_e$) were calculated. The delay (Δ) between the contrast bolus arrival in the artery and the tissue was determined by fitting the data with a range of delay values and choosing the delay with the best fit. Fitting was performed with an in-house developed C++ computer program using the CFSQP package [145].

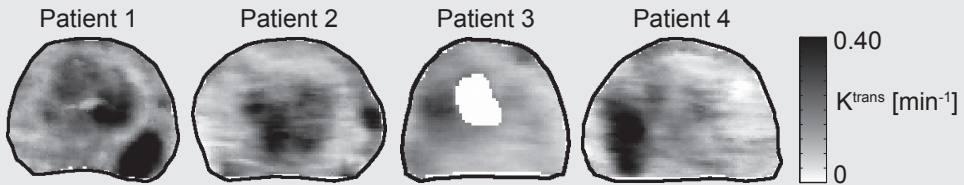
Image analysis

Standardized regions of interest (ROI) of 0.3 cc were placed in the prostate with the aid of all available clinical information including biopsy results. The ROIs were placed in high K^{trans} regions of the peripheral zone (PZ) suspected of tumor tissue (ROI_{susp}), and in regions of the PZ and central gland (CG) that were not suspected of tumor. ROI_{susp} had to match with a low signal intensity on the T_2 -weighted MR scan. With a T_1 -weighted MR scan we ensured that the low intensity of the T_2 -weighted MR scan was not caused by bleedings from the biopsy. To avoid inclusion of high K^{trans} regions containing benign prostate hyperplasia (BPH) [29, 78, 114, 146], we only placed ROI_{susp} in the PZ. For every ROI a mean enhancement curve was calculated and analyzed with the tracer kinetic model (Equation 6.1).

To test for differences in K^{trans} values between healthy tissue and ROI_{susp} and for differences in K^{trans} values and prostate volumes between patients with and without HT, we performed a balanced one-way analysis of variance (ANOVA) test with a significance level of $p < 0.05$.

We performed a logistic regression on the K^{trans} values obtained with the ROI analysis to calculate a probability function for the presence of tumor. For every patient, we considered the average K^{trans} values in the PZ and CG as healthy and the ROI_{susp} as tumor. The resulting probability function was used to convert all parameter maps into probability maps. We applied a stratification at the 5% and 95% level, to identify low-, intermediate- and high-risk areas for the presence of tumor.

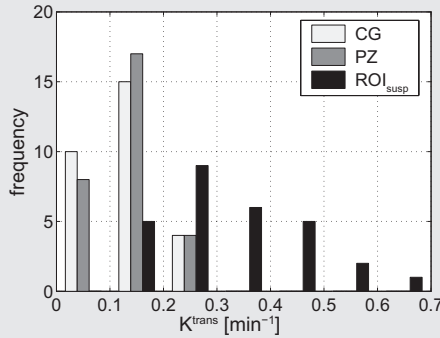
Figure 6.1



Examples of transversal slices of the 3D K^{trans} maps of the prostate. High K^{trans} areas can be found in the peripheral zone (PZ) as well as in the central gland (CG). The white region in patient 3 is the cavity caused by a transurethral resection of the prostate (TURP). Here no K^{trans} values were determined.

Table 6.1 Mean K^{trans} values [min^{-1}] with standard deviation

	Hormone therapy (N=10)	No hormone therapy (N=19)	p-value (ANOVA)
Entire prostate	0.14±0.03	0.15±0.04	0.697
Central gland	0.14±0.06	0.13±0.05	0.798
Peripheral zone	0.12±0.06	0.15±0.05	0.232
ROI_{susp}	0.32±0.17	0.33±0.10	0.870

Figure 6.2

Histogram of K^{trans} values from the ROI analysis in the central gland (CG), peripheral zone (PZ) and regions suspected for tumor (ROI_{susp}).

6.3 Results

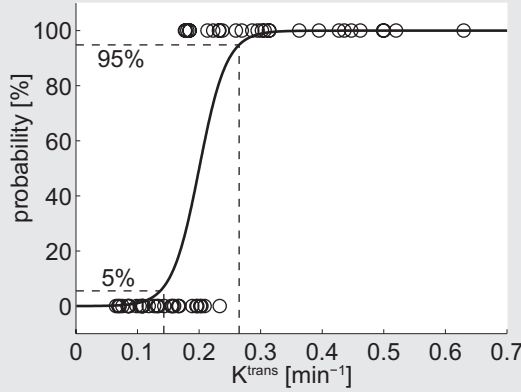
For all patients the 3D tracer kinetic model parameter maps were calculated. We only used parameter K^{trans} for further analysis, since this parameter can discriminate between prostate cancer and healthy prostate tissue [27, 29, 41, 108, 114]. Figure 6.1 shows examples of transversal slices of parameter K^{trans} from four patients. High K^{trans} areas can be observed in the PZ as well as the CG.

Before performing a logistic regression on the ROI data, we searched for differences between the patients with and without hormone therapy (HT). The prostate volumes of patients with HT were significantly smaller ($p = 0.025$) compared to patients without HT, with mean volumes of 36.2 ± 7.8 cc and 44.4 ± 9.4 cc respectively. In one patient with HT no ROI_{susp} could be found. In patients with androgen deprivation HT decreased K^{trans} values are reported [80]. When comparing the K^{trans} values in the CG, PZ, ROI_{susp} and entire prostate for patients with and without HT, no significant differences were found (Table 6.1). We therefore did not analyze the ROI results separately for patients with and without HT and used the ROI information of all patients for the logistic regression.

The mean K^{trans} values in the regions suspected of tumor (ROI_{susp}) of 0.32 ± 0.12 min⁻¹ were significantly higher than in the normal PZ (0.14 ± 0.05 min⁻¹, $p < 0.001$) and normal CG (0.13 ± 0.05 min⁻¹, $p < 0.001$). K^{trans} values in the CG and PZ were not significantly different. ROI_{susp} yields a broader range of K^{trans} values than the PZ and CG and there was an overlap in K^{trans} values between healthy considered CG and PZ tissue and ROI_{susp}, as can be seen in Figure 6.2.

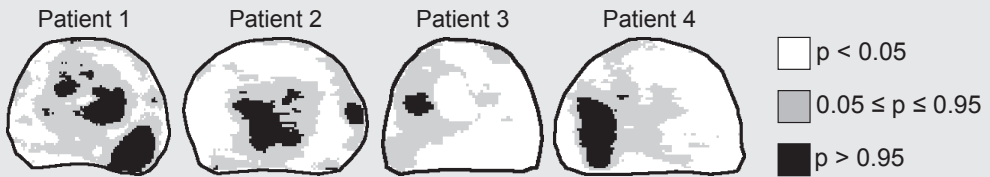
For every patient we considered the average K^{trans} value in the PZ and CG as healthy and the ROI_{susp} as tumor and performed a logistic regression on all patient data (Figure 6.3). Subsequently, all K^{trans} parameter maps were converted into probability maps. We then applied a stratification at the 5% and 95% level, to identify low-, intermediate- and high-risk areas for the presence of tumor. The two threshold values of K^{trans} for the 5% and 95% probability levels were 0.14 min⁻¹ and 0.27 min⁻¹ respectively.

Figure 6.3



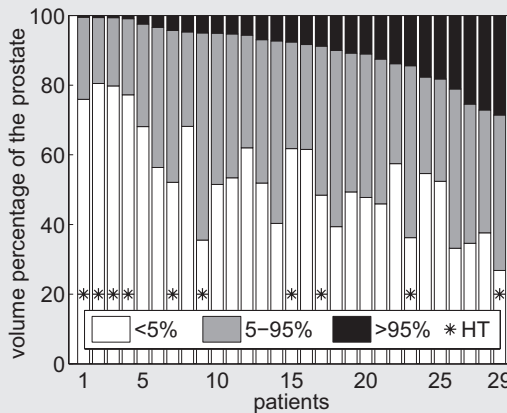
Based on the ROI results (○) a logistic regression was performed to obtain a probability function for the presence of tumor (solid line). A stratification at the 5% and 95% probability level (dashed lines) was applied, to identify low-, intermediate- and high-risk areas for the presence of tumor.

Figure 6.4



These transversal probability maps show the low-, intermediate, and high-risk areas in the prostate, based on the K^{trans} maps shown in Figure 6.1. The stratification is based on the probability function shown in Figure 6.3.

Figure 6.5



Volume fractions of the low-, intermediate en high-risk areas of all patients, sorted by the fractional volume of the high-risk area. Patients with androgen deprivation hormone therapy are depicted with an asterisk (*).

In the probability maps of Figure 6.4, high risk areas (>95%) for the presence of tumor can be observed in the PZ and CG, surrounded by intermediate-risk (5-95%) areas. Large parts of the prostate have a low risk (<5%) for containing tumor. If we now quantify these high-, intermediate- and low-risk regions as a fraction of the total prostate volume, we obtain median volume percentages of 7.6 (range 0.5-28.6), 40.0 (range 18.9-59.4) and 52.1 (range 26.8-80.5) percent respectively for the entire patient group.

By sorting these fractional volumes according to the amount of high-risk volume, we obtain the histogram in Figure 6.5. In patients with HT, a smaller high-risk area ($7.1 \pm 8.8\%$) is found compared to patients without HT ($11.4 \pm 7.4\%$), although not significantly different ($p = 0.176$).

6.4 Discussion

In a radiotherapy treatment setting, intrinsic imaging uncertainties and the lack of a ground truth make an accurate delineation of prostate tumors difficult. We therefore presented a practical approach to deal with the uncertainties of DCE imaging for prostate tumor delineation. In a diagnostic setting, DCE-MRI is often used since no radiation burden is involved with a DCE-MR exam. However, DCE-MRI suffers from a complex relation between the signal intensity and concentration of the contrast agent [46], thereby complicating further analysis. In particular, the determination of the arterial input function (AIF), required for quantitative tracer kinetic modeling, can be unreliable [49, 109, 110]. For that reason, we chose to illustrate our approach with DCE-CT as functional imaging technique. The radiation burden of a DCE-CT exam is small compared to the radiotherapy treatment given afterwards. Furthermore, the quantification of DCE-CT data is robust and straightforward because of a linear relation between Hounsfield units (H.U.) and contrast agent concentration.

Henderson *et al* performed a DCE-CT study for prostate cancer and report blood flow values of 0.37 ± 0.12 ml/min/g in regions suspected of tumor tissue and 0.18 ± 0.05 ml/min/g in healthy prostate tissue. They analyzed their data with a distributed tracer kinetic model, so these blood flow values cannot be directly compared to the K^{trans} values in this study. However, if we assume that K^{trans} is flow-limited as a result of a high permeability of the vasculature [25], they are in the same range. For DCE-MRI a broader range of K^{trans} values is reported for healthy prostate tissue (0.06 - 0.74 min⁻¹) and in tumors (0.47 - 1.26 min⁻¹) [29, 41, 43, 108]. This reflects the difficulties in absolute quantification of DCE-MRI as described above.

We found a significant difference in K^{trans} values between regions suspected for tumor and regions in healthy considered prostate tissue. An overlap in K^{trans} values was observed between ROI_{susp} and the CG and PZ. By performing a logistic regression on these data, we incorporated the intrinsic imaging uncertainties into the voxel wise tumor delineation process. By applying a stratification at the 5% and 95% probability level, we could determine high-, intermediate and low-risk areas for the presence of tumor in the prostate. This stratification resulted in contiguous regions (Figure 6.4),

even though the decision per voxel was made without incorporating information about neighboring voxels.

A practical approach to deal with these contiguous regions with varying risk levels, would be to convert it to the commonly used GTV and CTV concept. Importantly, in older literature of prostate radiotherapy, the GTV is interpreted as the entire prostate, with the CTV often taken equal to the GTV, sometimes with a small margin around the prostate [5-7]. This does not reflect the variations in tumor load. With functional imaging techniques like DCE imaging, the GTV and CTV concept can be refined. The high-risk area within the prostate (>95%) can be defined as GTV and can be used as a target volume within the prostate for dose escalation, similar to the concept of GTV_{MRI} of De Meerleer *et al* [15] and GTV_{PET} of Pinkawa *et al* [147]. The CTV is defined as subclinical disease and can therefore be identified with the low-risk areas (<5%), receiving the regular dose of 78 Gy [148]. The intermediate-risk region (5-95%) in between, could be defined as high-risk CTV, following a concept earlier proposed by the gynaecological GEC-ESTRO Working Group for cervical brachytherapy [149, 150]. The high-risk CTV may function as a margin around the target for further dose escalation.

An example of the use of this approach for planning a micro-boost for dose escalation, can be demonstrated for patient 1 from Figure 6.4. A GTV is found at the left anterior side of the prostate. To deliver the appropriate micro-boost dose to this GTV, one can decide to deliver locally a higher dose to the rectum at the left patient side, and spare the rectum at the right patient side, since no GTV or high-risk CTV is found there.

A different strategy to interpret the probability maps is by converting a particular probability for the presence of tumor into a dose prescription per voxel. This approach is known as dose painting by numbers [151]. Based on DCE-MRI, Vos *et al* developed an automated computerized scheme for determining a likelihood measure of malignancy for regions in the prostate suspicious for cancer [152]. They extracted pharmacokinetic parameters from tumors and regions of healthy prostate tissue in the pZ. With whole mount step-section histopathology as standard of reference, they trained a support vector machine as classifier. It is not known how well their method performs on single voxels, needed for prostate tumor delineation for focal therapies.

The probability maps like in Figure 6.4 should however be interpreted with caution, since it is hard to distinguish benign prostate hyperplasia (BPH) from tumor based on K^{trans} only [29, 78, 114, 146]. It is therefore worthwhile to use clinical information as well as other imaging modalities if available.

The logistic regression performed in this study was based on imaging data and clinical information. If pathology were available, this logistic regression could be further refined. However, pathology will by definition not become available for patients scheduled for radiotherapy.

In conclusion, we present a practical approach to deal with the intrinsic imaging uncertainties and the lack of a ground truth for voxelwise prostate tumor delineation. By converting DCE imaging data into tumor probabilities, we can interpret this information into GTV and high-risk CTV concepts, which can be used for radiotherapy treatment planning.

7

Chapter 7

General discussion

The preceding chapters addressed a number of uncertainties and methodological choices in the quantification of DCE data with tracer kinetic models (TKMs) for tumor delineation in prostate cancer patients. A majority of these studies can be considered as radiology research, but its relevance for radiotherapy treatment has always been kept in mind. Patients that are scheduled for radiation therapy have biopsy proven prostate cancer, so the question whether a patient has prostate cancer has already been answered. Questions that are of specific interest for radiation therapy are for example the detection of the precise boundaries of the tumor within the prostate and the biological characterization of the tissue for treatment monitoring and follow-up [153].

For the purpose of tumor delineation, qualitative measures as the maximum peak height, time to peak, area under the curve and maximum upslope may be sufficient to visualize suspicious areas with anomalous tracer uptake. Although these qualitative measures are very intuitive and easy to calculate, they depend quite heavily on the cardiac output and the injection and acquisition protocols. Therefore, these measures may vary substantially between consecutive measurements in single patients and between institutions. TKMs are less affected by these differences in cardiac output and injection protocols because they take these factors explicitly into account via the arterial input function (AIF). Furthermore, TKMs enable both tumor delineation and biological characterization of the prostate tissue in terms of blood flow and leakage space, which is useful for longitudinal studies. So, the quantification of DCE data with TKMs has a clear advantage for radiation therapy compared to the use of qualitative measures.

7.1 The importance of the arterial input function (AIF)

For tumor delineation based on K^{trans} maps, for each voxel the decision should be made whether it is tumor or not. This way of delineating a tumor can be automatically performed by defining threshold values for healthy and suspicious areas. However, the performance of such a methodology depends on the definition of the right threshold values. Because the AIF is one of the key factors in determining the accuracy of TKM parameters, Chapters 2 and 3 investigated the uncertainties associated with the measurement of an AIF.

In Chapter 2 we found that for DCE-CT exams the measurement of the AIF is hardly dependent on the anatomical location. Furthermore, the reported intra-exam variations may serve as a benchmark for detecting artifacts in the AIF measurements on DCE-MRI. For the quantification of DCE-CT exams, the use of an exam-specific AIF is preferred, since the intra-exam and intra-patient variations are smaller than the observed inter-patient variations. Although this results in an additional post-processing step compared to the use of a population-averaged AIF, the accuracy and precision of the TKM parameters will be better. It is expected that with the use of an exam-specific AIF a threshold approach for tumor delineation, as described in Chapter 6, will be more successful compared to the use of a population-averaged AIF.

In the same Chapter 2, the errors associated with the use of a population-averaged AIF were investigated. Although this problem is particularly relevant for the quantification of DCE-MRI exams, we used DCE-CT exams to determine the inter-patient variations in exam-specific AIFs. We found that the shapes of the exam-specific AIFs were very similar in all patients, but that the amplitudes differed substantially, with a random and a weight-dependent component. This finding stresses the need of measuring an exam-specific AIF in case a fixed amount of contrast agent is injected in all patients.

The inter-patient variations that were neglected with the use of a population-averaged AIF lead to an average deviation of 12.8% in K^{trans} compared to the use of an exam-specific AIF. This has however no consequences for the visibility of tumors within the prostate of single patients, since the K^{trans} values are mainly scaled in a homogeneous way. For robust tumor delineation in a large group of patients however, this additional uncertainty of 12.8% will obscure the differentiation between K^{trans} values in healthy tissue and tumors.

In the Supplement of Chapter 2 we presented a modality-independent population-averaged AIF for an injection time of 10 seconds. This AIF has a number of advantages compared to the population-averaged AIFs at the level of the femoral arteries that have been published earlier, e.g. by Parker [49]. First, it is CT-based and not MRI-based, and therefore not affected by artifacts frequently encountered with DCE-MRI exams. Second, the intra-exam, intra-patient and inter-patient uncertainties associated with this AIF are well-described and give a good indication of the resulting uncertainties in K^{trans} values. Furthermore, it can be easily adapted for contrast agents with other molarities. Its value for DCE protocols with different injection times is however unclear.

We used in Chapter 3 an alternative approach to measure an exam-specific AIF from a DCE-MRI exam, by taking the phase rather than the magnitude signal, as has been described earlier by Akbudak *et al* [88, 89]. In that way, we were able to avoid a number of artifacts that may make a reliable exam-specific AIF measurement from the magnitude signal difficult. We showed that by using a phase-based exam-specific AIF, no differences were observed in K^{trans} maps of both modalities. This means, that DCE exams on CT and MRI give essentially the same K^{trans} values, even with differences in injection protocol, contrast agent and sampling intervals. This finding is promising for the definition of thresholds for tumor delineation, since these will be valid for both DCE-MRI and DCE-CT exams.

A challenge that remains to be solved for the clinical use of phase-based AIFs is the correction for drift of the magnetic field during acquisition. We subtracted the signal from a manually delineated piece of muscle tissue near the femoral arteries. For common clinical application however, more robust correction methods should become available. Still, the measurement consistency of phase-based AIFs between the left and right arteries shows less uncertainty than the inter-patient variations

reported in Chapter 2. Therefore, the use of phase-based exam-specific AIFs should be preferred above the use of a population-averaged AIF for DCE-MRI exams of prostate cancer.

In short, we characterized the reliability of measuring an exam-specific AIF on both CT and MRI and compared it with the use of a population-averaged AIF. There is no doubt, that for DCE-CT exams the use of an exam-specific AIF should be preferred. For DCE-MRI however, some challenges are left to ensure reliable and wide-spread clinical use of phase-based AIFs. For the time being, the use of a well-described population-averaged AIF may also be a good option if major difficulties are encountered with measuring an AIF from the magnitude signal.

7.2 Choices in tracer kinetic model (TKM) analysis

As with all good things in life, there is always ‘the other side of the medal’. In Chapter 4 we demonstrated that a good voxelwise repeatability of DCE-CT exams for prostate cancer can be achieved, but that a better repeatability comes with a lower spatial resolution. For reliable tumor delineation, kernels between 0.05 and 0.3 cc, equal to 3.7 to 6.7 mm cubic kernels, yield an acceptable trade-off between repeatability and spatial resolution. This finding immediately has consequences for the size of the smallest detectable lesions, which is by definition equal to the kernel size [154]. The implications of these results for DCE-MRI exams of the prostate need further investigation. As the signal-to-noise ratio in MRI is expected to be higher than in CT, at least a spatial resolution similar to that found in DCE-CT exams should be achievable.

To validate the minimal detectable lesion size with pathology, a correlation with at least the same spatial resolution as the kernel size would be necessary. Despite the fact that Groenendaal *et al* showed that a registration error of 2-3 mm can be achieved between whole slice prostate specimen and MRI [155], pathological validation of these DCE-CT exams is not feasible because of two reasons. First, it is unacceptable to perform DCE-CT exams in patients that will undergo a prostatectomy, because of the high radiation dose involved. Second, patients that undergo a prostatectomy in the UMC Utrecht generally have low-grade tumors. It is not known whether their pathology and imaging information is representative for high-grade tumors, which are generally treated with external beam radiation therapy. So, direct histopathological validation of DCE-CT exams will remain problematic. Therefore, a good understanding of its interchangeability with DCE-MRI is very valuable. A different matter in this kernel size trade-off is to what spatial resolution dose escalation to the lesion is required and feasible. It is known that prostate cancer is a multifocal disease, but most studies focus on the treatment of the dominant lesions, which are often much larger than 0.3 cc.

A different trade-off is described in Chapter 5, which dealt with TKM selection. We found for all patients that all three TKMs are the optimal model in part of the prostate. Although it is possible to combine these models through multi-modal

inference [131], in clinical practice one model will be used. This poses the problem of choosing a model which is not optimal under all conditions, resulting in under- or overfitting. Differences between the model fits are however small and for tumor delineation this does not pose a problem. In contrast, for tissue characterization the choice for one or the other model may be more crucial, since TKMs try to describe the underlying physiological processes. Additional to this information theoretical approach described in Chapter 5, correlations should be obtained between histological tissue parameters like microvessel density, to understand the underlying factors that determine the contrast enhancement in the prostate tissue.

7.3 Image-guided radiation therapy

Chapter 6 described how imaging uncertainties in DCE exams can be converted into margin concepts that can be used for radiation treatment planning. This study should however be interpreted as a conceptual study rather than the optimal way to plan a micro-boost within the prostate. First, a number of image contrast are available that may give information about the underlying physiology in the prostate. Using DCE imaging as the only functional technique is not recommended because of the low specificity in the central gland. Second, combining DCE exams with DWI exams may lead to conflicting information with regard to the tumor delineation, as described by Groenendaal *et al* [156]. Because whole-slice prostatectomy specimens are lacking in patients scheduled for radiation therapy and the location of a prostate biopsy is only approximately known, it remains unclear whether DWI or DCE images are more reliable and whether they give additional rather than conflicting information.

The results described in Chapter 6 can be combined with other quantitative image contrasts, to enable multimodal tumor delineation and multimodal tumor characterization. For longitudinal studies however, the validation of quantitative imaging parameters with whole-slice pathology is needed, to be able to understand where image contrasts originate from. Furthermore, the effect of pharmaceuticals on imaging parameters like K^{trans} should be investigated, to enable unbiased tumor delineation.

7.4 CT versus MRI

In this thesis, DCE-MRI and DCE-CT were directly compared. It is however debatable whether they are really analogous imaging techniques. As discussed in Chapter 3, in our institution differences exist between the injection protocols of DCE-MRI and DCE-CT exams. We explicitly chose to adopt the injection protocols as they are in use at the Radiology department, rather than adjusting them in order to obtain identical injection protocols. For DCE-MRI examinations, a body weight dependent amount of contrast agent, e.g. 0.1 mmol/kg, is injected, whereas for DCE-CT exams a fixed amount is injected in all patients. For a typical patient of about 80 kg, either 8 ml of a 1M MR contrast agent will be injected or 60 ml of a CT contrast agent. Although this difference in volume seems considerable, it is negligible compared to an average blood volume of 5 to 6 liter. In case identical injection protocols are desired, a

possible solution would be to adjust the injection speed in ml/sec or to dilute the MR contrast agent, to obtain identical injection times and injection volumes for the DCE-MRI and DCE-CT exams. Although this may improve the comparison between CT-based and MR-based AIFs, it was shown in Chapter 3 that with different injection protocols the K^{trans} values were not significantly different between DCE-MRI and DCE-CT exams of the prostate.

When we consider the physical, chemical and pharmacological properties of the contrast agents used in the studies described in this thesis, Gadovist 1M (Schering AG, Berlin, Germany) and Ultravist 300 (Schering AG, Berlin, Germany), the most pronounced difference is observed in the osmolarity (Table 7.1). The differences in molecular weight, pH, viscosity, distribution half life and elimination half life are however much smaller (Table 7.1). This may explain the good correspondence in K^{trans} values between DCE-MRI and DCE-CT as reported in Chapter 3. An obvious solution to eliminate these differences between contrast agents is to use one contrast agent for both DCE exams. In a study with rabbits, the use of Gadovist (1M) as a potential CT contrast agent has been demonstrated, although the contrast enhancement was 1.5-fold lower when compared to an identical dose of Ultravist 300 [157]. The validity of these results for humans is however unknown, and in view of the risks on nephrogenic systemic fibrosis (NSF) [158, 159] and contrast material-induced nephropathy (CIN) [160, 161], the injection of large amounts of MR contrast agent is undesirable.

A topic that needs to be addressed in more detail is the relevance of water exchange effects in DCE-MRI exams. The DCE-MRI signal is related to the effect of the MR contrast agent on the relaxivity of nearby water molecules, rather than the concentration of the contrast agent itself [38-40, 106]. In view of the similar K^{trans} values reported for CT and MRI in Chapter 3, it seems that water exchange effects do not play a major role in our current clinical DCE-MRI acquisition protocol. Bains *et al* [106] found similar results in a group of bladder cancer patients, with no significant differences in blood flow between DCE-MRI and DCE-CT exams. Nevertheless, further research is needed on how acquisition parameters may influence the sensitivity of the DCE-MRI signal to water exchange effects, to facilitate unbiased comparisons with DCE-CT enhancement curves.

Table 7.1 Comparison between the used CT and MRI contrast agents

	Gadovist 1M (gadopentetate dimeglumine)	Ultravist 300 (iopromide)
Molecular weight (u)	604.72	791.12
pH (at 25°)	6.6 - 8.0	6.5 - 8.0
Viscosity (at 37°)	5.0	4.9
Osmolarity (mOsmol/L at 37°)	1603	1117
Distribution half life (h)	0.2	0.1
Elimination half life (h)	1.8	2.3

7.5 Future perspectives

The use of DCE-CT as a benchmark for DCE-MRI can be useful, as demonstrated in this thesis. In the long run however, DCE-MRI will prevail over DCE-CT in the specific case of prostate cancer. Until now, DCE-CT outperforms DCE-MRI when it comes to robust AIF measurements, but it has a relatively low signal-to-noise ratio in the prostate tissue and a high radiation dose. Because of this radiation burden, MRI is the better alternative for treatment monitoring and follow-up. It is expected that a better understanding of water exchange effects and underlying physiology will make the use of CT as imaging modality for DCE exams in prostate cancer needless in the future. For the time being, DCE-CT can be a good reference to validate DCE-MRI measurements. In that light, advanced noise reduction methods for DCE-CT exams may be necessary to facilitate reliable comparisons with DCE-MRI [162, 163].

The recommendations from a European consensus meeting on MRI for prostate cancer state that the DCE technique is one of the key sequences that should minimally be incorporated in a multi-parametric MRI exam for prostate cancer [164]. Nevertheless, a major weakness in the current DCE imaging practice is the lack of standardized injection, acquisition and post-processing protocols. For comparisons between patients or follow-up studies within single institutions this is not a problem. However, when performing multi-center studies or comparing literature values of tracer kinetic model parameters, these differences in data acquisition and analysis may hamper a trustworthy comparison between institutes. This lack of standardization is reflected by the disagreements reported from the aforementioned European consensus meeting with regard to the acquisition and analysis of DCE-MRI data [164]. Although one consensus paper has been published on the definitions and nomenclature of tracer kinetic models (TKMs) [25], specific consensus on DCE imaging, as has been reported for diffusion weighted imaging (DWI) [44], has not been achieved yet.

In conclusion, a number of studies have been performed to facilitate well-founded decision making in the quantification process of DCE-MRI and DCE-CT exams for tumor delineation in prostate cancer. It was shown that 1) with an appropriate AIF measurement repeatable TKM parameters can be obtained from the prostate tissue, 2) that DCE-MRI and DCE-CT give very similar TKM parameter maps and 3) that these TKM parameters can be converted into concepts that are useful for radiation treatment planning.

8

- [1] IKNL. Integraal Kankercentrum Nederland - Kankerregistratie. [online] Available at: <www.ikcnet.nl> [Accessed 25 March 2011].
- [2] Jemal, A, Siegel, R, Xu, J, Ward, E. Cancer statistics 2010. *CA Cancer J Clin* 2010;60:277-300.
- [3] KWF. KWF Kankerbestrijding - Prostaatkanker. [online] Available at: <http://kanker.kwfkankerbestrijding.nl/soorten-kanker/Pages/soorten-kanker-prostaatkanker.aspx> [Accessed 25 March 2011].
- [4] Webb, S. Chapter 43: Conformal and Intensity Modulated Radiotherapy. In: Mayles P, Nahum, Rosenwald J, editors. *Handbook of Radiotherapy Physics - Theory and Practice*, Boca Raton, Florida, USA: CRC Press. 2007.
- [5] Stroom, JC, Storchi, PR. Automatic calculation of three-dimensional margins around treatment volumes in radiotherapy planning. *Phys Med Biol* 1997;42:745-755.
- [6] Hanks, GE, Hanlon, AL, Schultheiss, TE, et al. Dose escalation with 3D conformal treatment: five year outcomes, treatment optimization, and future directions. *Int J Radiat Oncol Biol Phys* 1998;41:501-510.
- [7] Pickett, B, Roach, M, 3rd, Verhey, L, et al. The value of nonuniform margins for six-field conformal irradiation of localized prostate cancer. *Int J Radiat Oncol Biol Phys* 1995;32:211-218.
- [8] Pollack, A, Zagars, GK, Starkschall, G, et al. Prostate cancer radiation dose response: results of the M. D. Anderson phase III randomized trial. *Int J Radiat Oncol Biol Phys* 2002;53:1097-1105.
- [9] Zietman, AL, DeSilvio, ML, Slater, JD, et al. Comparison of conventional-dose vs high-dose conformal radiation therapy in clinically localized adenocarcinoma of the prostate: a randomized controlled trial. *JAMA* 2005;294:1233-1239.
- [10] Peeters, STH, Heemsbergen, WD, Koper, PCM, et al. Dose-response in radiotherapy for localized prostate cancer: results of the Dutch multicenter randomized phase III trial comparing 68 Gy of radiotherapy with 78 Gy. *J Clin Oncol* 2006;24:1990-1996.
- [11] Cellini, N, Morganti, AG, Mattiucci, GC, et al. Analysis of intraprostatic failures in patients treated with hormonal therapy and radiotherapy: implications for conformal therapy planning. *Int J Radiat Oncol Biol Phys* 2002;53:595-599.
- [12] Pucar, D, Sella, T, Schöder, H. The role of imaging in the detection of prostate cancer local recurrence after radiation therapy and surgery. *Curr Opin Urol* 2008;18:87-97.
- [13] Pickett, B, Vigneault, E, Kurhanewicz, J, Verhey, L, Roach, M. Static field intensity modulation to treat a dominant intra-prostatic lesion to 90 Gy compared to seven field 3-dimensional radiotherapy. *Int J Radiat Oncol Biol Phys* 1999;44:921-929.
- [14] Nederveen, AJ, van der Heide, UA, Hofman, P, Welleweerd, H, Legendijk, JJ. Partial boosting of prostate tumours. *Radiother Oncol* 2001;61:117-126.
- [15] Meerleer, GD, Villeirs, G, Bral, S, et al. The magnetic resonance detected intraprostatic lesion in prostate cancer: planning and delivery of intensity-modulated radiotherapy. *Radiother Oncol* 2005;75:325-333.
- [16] van Lin, ENJT, Fütterer, JJ, Heijmink, SWTPJ, et al. IMRT boost dose planning on dominant intraprostatic lesions: gold marker-based three-dimensional fusion of CT with dynamic contrast-enhanced and 1H-spectroscopic MRI. *Int J Radiat Oncol Biol Phys* 2006;65:291-303.
- [17] ClinicalTrials.gov. FLAME: Investigate the Benefit of a Focal Lesion Ablative Microboost in Prostate Cancer. [online] Available at: <http://www.clinicaltrials.gov> [Accessed 25 March 2011].
- [18] Marcus, CD, Ladam-Marcus, V, Cucu, C, Bouché, O, Lucas, L, Hoeffel, C. Imaging techniques to evaluate the response to treatment in oncology: current standards and perspectives. *Crit Rev Oncol Hematol* 2009;72:217-238.
- [19] Rasch, C, Steenbakkers, R, van Herk, M. Target definition in prostate, head, and neck. *Semin Radiat Oncol* 2005;15:136-145.
- [20] Kirkham, APS, Emberton, M, Allen, C. How good is MRI at detecting and characterising cancer within the prostate? *Eur Urol* 2006;50:1163-1174; discussion 1175.

- [21] Fütterer, JJ, Heijmink, SWTPJ, Scheenen, TWJ, et al. Prostate cancer: local staging at 3-T endorectal MR imaging--early experience. *Radiology* 2006;238:184-191.
- [22] DeSouza, NM, Reinsberg, SA, Scurr, ED, Brewster, JM, Payne, GS. Magnetic resonance imaging in prostate cancer: the value of apparent diffusion coefficients for identifying malignant nodules. *Br J Radiol* 2007;80:90-95.
- [23] Haider, MA, van der Kwast, TH, Tanguay, J, et al. Combined T2-weighted and diffusion-weighted MRI for localization of prostate cancer. *AJR Am J Roentgenol* 2007;189:323-328.
- [24] Tanimoto, A, Nakashima, J, Kohno, H, Shinmoto, H, Kuribayashi, S. Prostate cancer screening: the clinical value of diffusion-weighted imaging and dynamic MR imaging in combination with T2-weighted imaging. *J Magn Reson Imaging* 2007;25:146-152.
- [25] Tofts, PS, Brix, G, Buckley, DL, et al. Estimating kinetic parameters from dynamic contrast-enhanced T1-weighted MRI of a diffusable tracer: standardized quantities and symbols. *J Magn Reson Imaging* 1999;10:223-232.
- [26] Parker, GJM, Buckley, DL. Tracer Kinetic Modeling for T1-weighted Dynamic Contrast-Enhanced MRI. In: Jackson A, Buckley DL, Parker GJM, editors. *Dynamic Contrast-Enhanced Magnetic Resonance Imaging in Oncology*, Heidelberg, Germany: Springer-Verlag. 2005.
- [27] Buckley, DL, Roberts, C, Parker, GJM, Logue, JP, Hutchinson, CE. Prostate cancer: evaluation of vascular characteristics with dynamic contrast-enhanced T1-weighted MR imaging--initial experience. *Radiology* 2004;233:709-715.
- [28] Fütterer, JJ, Heijmink, SWTPJ, Scheenen, TWJ, et al. Prostate cancer localization with dynamic contrast-enhanced MR imaging and proton MR spectroscopic imaging. *Radiology* 2006;241:449-458.
- [29] van Dorsten, FA, van der Graaf, M, Engelbrecht, MRW, et al. Combined quantitative dynamic contrast-enhanced MR imaging and (1)H MR spectroscopic imaging of human prostate cancer. *J Magn Reson Imaging* 2004;20:279-287.
- [30] Seitz, M, Shukla-Dave, A, Bjartell, A, et al. Functional magnetic resonance imaging in prostate cancer. *Eur Urol* 2009;55:801-814.
- [31] Carmeliet, P, Jain, RK. Angiogenesis in cancer and other diseases. *Nature* 2000;407:249-257.
- [32] Oostendorp, M, Post, MJ, Backes, WH. Vessel growth and function: depiction with contrast-enhanced MR imaging. *Radiology* 2010;251:317-335.
- [33] de Bazelaire, C, Rofsky, NM, Duhamel, G, et al. Combined T2* and T1 measurements for improved perfusion and permeability studies in high field using dynamic contrast enhancement. *Eur Radiol* 2006;16:2083-2091.
- [34] Roberts, C, Little, R, Watson, Y, Zhao, S, Buckley, DL, Parker, GJM. The effect of blood inflow and B(1)-field inhomogeneity on measurement of the arterial input function in axial 3D spoiled gradient echo dynamic contrast-enhanced MRI. *Magn Reson Med* 2011;65:108-119.
- [35] Cheng, HL. T1 measurement of flowing blood and arterial input function determination for quantitative 3D T1-weighted DCE-MRI. *J Magn Reson Imaging* 2007;25:1073-1078.
- [36] Ivancevic, MK, Zimine, I, Montet, X, et al. Inflow effect correction in fast gradient-echo perfusion imaging. *Magn Reson Med* 2003;50:885-891.
- [37] Cheng, H-LM, Wright, GA. Rapid high-resolution T1 mapping by variable flip angles: accurate and precise measurements in the presence of radiofrequency field inhomogeneity. *Magn Reson Med* 2006;55:566-574.
- [38] Landis, CS, Li, X, Telang, FW, et al. Equilibrium transcytolemmal water-exchange kinetics in skeletal muscle in vivo. *Magn Reson Med* 1999;42:467-478.
- [39] Donahue, KM, Weisskoff, RM, Burstein, D. Water diffusion and exchange as they influence contrast enhancement. *J Magn Reson Imaging* 1997;7:102-110.
- [40] Kim, YR, Rebro, KJ, Schmainda, KM. Water exchange and inflow affect the accuracy of T1-GRE blood volume measurements: implications for the evaluation of tumor angiogenesis. *Magn Reson Med* 2002;47:1110-1120.

- [41] Kozlowski, P, Chang, SD, Jones, EC, Berean, KW, Chen, H, Goldenberg, SL. Combined diffusion-weighted and dynamic contrast-enhanced MRI for prostate cancer diagnosis--correlation with biopsy and histopathology. *J Magn Reson Imaging* 2006;24:108-113.
- [42] Ocak, I, Bernardo, M, Metzger, G, et al. Dynamic contrast-enhanced MRI of prostate cancer at 3 T: a study of pharmacokinetic parameters. *AJR Am J Roentgenol* 2007;189:W192-W201.
- [43] Kershaw, LE, Hutchinson, CE, Buckley, DL. Benign prostatic hyperplasia: evaluation of T₁, T₂, and microvascular characteristics with T₁-weighted dynamic contrast-enhanced MRI. *J Magn Reson Imaging* 2009;29:641-648.
- [44] Padhani, AR, Liu, G, Koh, DM, et al. Diffusion-weighted magnetic resonance imaging as a cancer biomarker: consensus and recommendations. *Neoplasia* 2009;11:102-125.
- [45] Buckley, DL, Parker, GJM. Tracer Kinetic Modeling for T₁-weighted Dynamic Contrast-Enhanced MRI. In: Jackson A, Buckley DL, Parker GJM, editors. *Dynamic Contrast-Enhanced Magnetic Resonance Imaging in Oncology*, Heidelberg, Germany: Springer-Verlag. 2005.
- [46] Schabel, CM, Parker, DL. Uncertainty and bias in contrast concentration measurements using spoiled gradient echo pulse sequences. *Phys Med Biol* 2008;53:2345-2373.
- [47] Kierkels, RGJ, Backes, WH, Janssen, MHM, et al. Comparison between perfusion computed tomography and dynamic contrast-enhanced magnetic resonance imaging in rectal cancer. *Int J Radiat Oncol Biol Phys* 2010;77:400-408.
- [48] Port, RE, Knopp, MV, Brix, G. Dynamic contrast-enhanced MRI using Gd-DTPA: interindividual variability of the arterial input function and consequences for the assessment of kinetics in tumors. *Magn Reson Med* 2001;45:1030-1038.
- [49] Parker, GJ, Roberts, C, Macdonald, A, et al. Experimentally-derived functional form for a population-averaged high-temporal-resolution arterial input function for dynamic contrast-enhanced MRI. *Magn Reson Med* 2006;56:993-1000.
- [50] Wang, Y, Huang, W, Panicek, DM, Schwartz, LH, Koutcher, JA. Feasibility of using limited-population-based arterial input function for pharmacokinetic modeling of osteosarcoma dynamic contrast-enhanced MRI data. *Magn Reson Med* 2008;59:1183-1189.
- [51] McGrath, DM, Bradley, DP, Tessier, JL, Lacey, T, Taylor, CJ, Parker, GJM. Comparison of model-based arterial input functions for dynamic contrast-enhanced MRI in tumor bearing rats. *Magn Reson Med* 2009;61:1173-1184.
- [52] Shukla-Dave, A, Lee, N, Stambuk, H, et al. Average arterial input function for quantitative dynamic contrast enhanced magnetic resonance imaging of neck nodal metastases. *BMC Med Phys* 2009;9:4.
- [53] Meng, R, Chang, SD, Jones, EC, Goldenberg, SL, Kozlowski, P. Comparison between population average and experimentally measured arterial input function in predicting biopsy results in prostate cancer. *Acad Radiol* 2010;17:520-525.
- [54] Rijpkema, M, Kaanders, JH, Joosten, FB, van der Kogel, AJ, Heerschap, A. Method for quantitative mapping of dynamic MRI contrast agent uptake in human tumors. *J Magn Reson Imaging* 2001;14:457-463.
- [55] Ashton, E, Raunig, D, Ng, C, Kelcz, F, McShane, T, Evelhoch, J. Scan-rescan variability in perfusion assessment of tumors in MRI using both model and data-derived arterial input functions. *J Magn Reson Imaging* 2008;28:791-796.
- [56] Horsfield, MA, Thornton, JS, Gill, A, Jager, HR, Priest, AN, Morgan, B. A functional form for injected MRI Gd-chelate contrast agent concentration incorporating recirculation, extravasation and excretion. *Phys Med Biol* 2009;54:2933-2949.
- [57] Yankeelov, TE, Luci, JJ, Lepage, M, et al. Quantitative pharmacokinetic analysis of DCE-MRI data without an arterial input function: a reference region model. *Magn Reson Imaging* 2005;23:519-529.
- [58] Fluckiger, JU, Schabel, MC, Dibella, EVR. Model-based blind estimation of kinetic parameters in dynamic contrast enhanced (DCE)-MRI. *Magn Reson Med* 2009;62:1477-1486.

- [59] Korporaal, JG, van den Berg, CAT, Jeukens, CRLPN, et al. Dynamic Contrast-enhanced CT for Prostate Cancer: Relationship between Image Noise, Voxel Size, and Repeatability. *Radiology* 2010;256:976-984.
- [60] Klein, S, Staring, M, Murphy, K, Viergever, M, Pluim, J. Elastix: a toolbox for intensity-based medical image registration. *IEEE Trans. Med. Imaging* 2009;29:196-205.
- [61] Henderson, E, Milosevic, MF, Haider, MA, Yeung, IWT. Functional CT imaging of prostate cancer. *Phys Med Biol* 2003;48:3085-3100.
- [62] Jeukens, CRLPN, van den Berg, CAT, Donker, R, et al. Feasibility and measurement precision of 3D quantitative blood flow mapping of the prostate using dynamic contrast-enhanced multi-slice CT. *Phys Med Biol* 2006;51:4329-4343.
- [63] Korporaal, JG, Van den Berg, CAT, Van Osch, MJP, Groenendaal, G, Van Vulpen, M, Van der Heide, UA. Phase-based arterial input function measurements in the femoral arteries for quantification of dynamic contrast-enhanced (DCE) MRI and comparison with DCE-CT. *Magn Reson Med* 2011; in press, DOI 10.1002/mrm.22905.
- [64] Conturo, TE, Akbudak, E, Kotys, MS, et al. Arterial input functions for dynamic susceptibility contrast MRI: requirements and signal options. *J Magn Reson Imaging* 2005;22:697-703.
- [65] Kotys, MS, Akbudak, E, Markham, J, Conturo, TE. Precision, signal-to-noise ratio, and dose optimization of magnitude and phase arterial input functions in dynamic susceptibility contrast MRI. *J Magn Reson Imaging* 2007;25:598-611.
- [66] Blomley, MJ, Dawson, P. Bolus dynamics: theoretical and experimental aspects. *Br J Radiol* 1997;70:351-359.
- [67] Bland, JM, Altman, DG. Statistical methods for assessing agreement between two methods of clinical measurement. *Lancet* 1986;1:307-310.
- [68] Bland, JM, Altman, DG. Measurement error. *BMJ* 1996;313:744.
- [69] Korman, M, Partanen, K, Soimakallio, S, Kivimäki, T. Dynamic contrast enhancement of the upper abdomen: effect of contrast medium and body weight. *Invest Radiol* 1983;18:364-367.
- [70] Kim, SM, Haider, MA, Milosevic, M, Yeung, IWT. Interindividual variability of arterial impulse response to intravenous injection of nonionic contrast agent (Iohexol) in DCE-CT study. *Med Phys* 2009;36:4791-4802.
- [71] Mendichovszky, IA, Cutajar, M, Gordon, I. Reproducibility of the aortic input function (AIF) derived from dynamic contrast-enhanced magnetic resonance imaging (DCE-MRI) of the kidneys in a volunteer study. *Eur J Radiol* 2009;71:576-581.
- [72] Galbraith, SM, Lodge, MA, Taylor, NJ, et al. Reproducibility of dynamic contrast-enhanced MRI in human muscle and tumours: comparison of quantitative and semi-quantitative analysis. *NMR Biomed* 2002;15:132-142.
- [73] Padhani, AR, Hayes, C, Landau, S, Leach, MO. Reproducibility of quantitative dynamic MRI of normal human tissues. *NMR Biomed* 2002;15:143-153.
- [74] Alonzi, R, Taylor, NJ, Stirling, JJ, et al. Reproducibility and correlation between quantitative and semiquantitative dynamic and intrinsic susceptibility-weighted MRI parameters in the benign and malignant human prostate. *J Magn Reson Imaging* 2010;32:155-164.
- [75] Kershaw, LE, Cheng, H-LM. Temporal resolution and SNR requirements for accurate DCE-MRI data analysis using the AATH model. *Magn Reson Med* 2010;64:1772-1780.
- [76] van Osch, MJ, Vonken, EJ, Wu, O, Viergever, MA, van der Grond, J, Bakker, CJ. Model of the human vasculature for studying the influence of contrast injection speed on cerebral perfusion MRI. *Magn Reson Med* 2003;50:614-622.
- [77] Aerts, HJWL, Van Riel, NAW, Backes, WH. System identification theory in pharmacokinetic modeling of dynamic contrast-enhanced MRI: influence of contrast injection. *Magn Reson Med* 2008;59:1111-1119.

- [78] Noworolski, SM, Vigneron, DB, Chen, AP, Kurhanewicz, J. Dynamic contrast-enhanced MRI and MR diffusion imaging to distinguish between glandular and stromal prostatic tissues. *Magn Reson Imaging* 2008;26:1071-1080.
- [79] Kiessling, F, Huber, PE, Grobholz, R, et al. Dynamic magnetic resonance tomography and proton magnetic resonance spectroscopy of prostate cancers in rats treated by radiotherapy. *Invest Radiol* 2004;39:34-44.
- [80] Padhani, AR, MacVicar, AD, Gapinski, CJ, et al. Effects of androgen deprivation on prostatic morphology and vascular permeability evaluated with mr imaging. *Radiology* 2001;218:365-374.
- [81] Franiel, T, Lüdemann, L, Taupitz, M, Böhmer, D, Beyersdorff, D. MRI before and after external beam intensity-modulated radiotherapy of patients with prostate cancer: the feasibility of monitoring of radiation-induced tissue changes using a dynamic contrast-enhanced inversion-prepared dual-contrast gradient-tissue echo sequence. *Radiother Oncol* 2009;93:241-245.
- [82] Kershaw, L, Logue, J, Hutchinson, C, Clarke, N, Buckley, D. Late tissue effects following radiotherapy and neoadjuvant hormone therapy of the prostate measured with quantitative magnetic resonance imaging. *Radiother Oncol* 2008;88:127-134.
- [83] van Vulpen, M, van den Berg, CAT, Moman, MR, van der Heide, UA. Difficulties and potential of correlating local recurrences in prostate cancer with the delivered local dose. *Radiother Oncol* 2009;93:180-184.
- [84] Haider, MA, Chung, P, Sweet, J, et al. Dynamic contrast-enhanced magnetic resonance imaging for localization of recurrent prostate cancer after external beam radiotherapy. *Int J Radiat Oncol Biol Phys* 2008;70:425-430.
- [85] Rouvière, O, Valette, O, Grivolat, S, et al. Recurrent prostate cancer after external beam radiotherapy: value of contrast-enhanced dynamic MRI in localizing intraprostatic tumor--correlation with biopsy findings. *Urology* 2004;63:922-927.
- [86] Moman, MR, van den Berg, CAT, Kruger, AEB, et al. Focal salvage guided by T2-weighted and dynamic contrast-enhanced magnetic resonance imaging for prostate cancer recurrences. *Int J Radiat Oncol Biol Phys* 2010;76:741-746.
- [87] Roberts, C, Little, R, Watson, Y, Zhao, S, Buckley, DL, Parker, GJM. The effect of blood inflow and B(i)-field inhomogeneity on measurement of the arterial input function in axial 3D spoiled gradient echo dynamic contrast-enhanced MRI. *Magn Reson Med* 2010;65:108-119.
- [88] Akbudak, E, Conturo, TE. Arterial input functions from MR phase imaging. *Magn Reson Med* 1996;36:809-815.
- [89] Akbudak, E, Norberg, RE, Conturo, TE. Contrast-agent phase effects: an experimental system for analysis of susceptibility, concentration, and bolus input function kinetics. *Magn Reson Med* 1997;38:990-1002.
- [90] de Rochefort, L, Nguyen, T, Brown, R, et al. In vivo quantification of contrast agent concentration using the induced magnetic field for time-resolved arterial input function measurement with MRI. *Med Phys* 2008;35:5328-5339.
- [91] Hoffman, RE. Measurement of magnetic susceptibility and calculation of shape factor of NMR samples. *J Magn Reson* 2006;178:237-247.
- [92] van Osch, MJP, Vonken, E-JPA, Viergever, MA, van der Grond, J, Bakker, CJG. Measuring the arterial input function with gradient echo sequences. *Magn Reson Med* 2003;49:1067-1076.
- [93] Cron, GO, Wallace, JC, Stevens, WD, et al. A comparison of T2*-weighted magnitude and phase imaging for measuring the arterial input function in the rat aorta following intravenous injection of gadolinium contrast agent. *Magn Reson Imaging* 2005;23:619-627.
- [94] Bleeker, EJW, van Buchem, MA, Webb, AG, van Osch, MJP. Phase-based arterial input function measurements for dynamic susceptibility contrast MRI. *Magn Reson Med* 2010;64:358-368.
- [95] Footitt, C, Cron, GO, Hogan, MJ, Nguyen, TB, Cameron, I. Determination of the venous output function from MR signal phase: feasibility for quantitative DCE-MRI in human brain. *Magn Reson Med* 2010;63:772-781.

- [96] Cron, GO, Footitt, C, Yankeelov, TE, Avruch, LI, Cameron, I. A comparison of arterial input functions derived from phase and magnitude for quantitative DCE-MRI of the prostate (abstract no. 2248). *Proc. Intl. Soc. Mag. Reson. Med.* 2009.
- [97] Pintaske, J, Martirosian, P, Graf, H, et al. ERRATUM: Relaxivity of Gadopentetate Dimeglumine (Magnevist), Gadobutrol (Gadovist), and Gadobenate Dimeglumine (MultiHance) in human blood plasma at 0.2, 1.5, and 3 Tesla. *Invest Radiol* 2006;41:859.
- [98] Sharma, P, Socolow, J, Patel, S, Pettigrew, RI, Oshinski, JN. Effect of Gd-DTPA-BMA on blood and myocardial T₁ at 1.5T and 3T in humans. *J Magn Reson Imaging* 2006;23:323-330.
- [99] Fram, EK, Herfkens, RJ, Johnson, GA, et al. Rapid calculation of T₁ using variable flip angle gradient refocused imaging. *Magn Reson Imaging* 1987;5:201-208.
- [100] Hittmair, K, Gomiscek, G, Langenberger, K, Recht, M, Imhof, H, Kramer, J. Method for the quantitative assessment of contrast agent uptake in dynamic contrast-enhanced MRI. *Magn Reson Med* 1994;31:567-571.
- [101] Brookes, JA, Redpath, TW, Gilbert, FJ, Murray, AD, Staff, RT. Accuracy of T₁ measurement in dynamic contrast-enhanced breast MRI using two- and three-dimensional variable flip angle fast low-angle shot. *J Magn Reson Imaging* 1999;9:163-171.
- [102] Köstler, H, Ritter, C, Lipp, M, Beer, M, Hahn, D, Sandstede, J. Prebolus quantitative MR heart perfusion imaging. *Magn Reson Med* 2004;52:296-299.
- [103] Bae, KT. Peak contrast enhancement in CT and MR angiography: when does it occur and why? Pharmacokinetic study in a porcine model. *Radiology* 2003;227:809-816.
- [104] Bhagwandien, R, Moerland, MA, Bakker, CJ, Beersma, R, Lagendijk, JJ. Numerical analysis of the magnetic field for arbitrary magnetic susceptibility distributions in 3D. *Magn Reson Imaging* 1994;12:101-107.
- [105] Yang, C, Stadler, WM, Karczmar, GS, Milosevic, M, Yeung, I, Haider, MA. Comparison of quantitative parameters in cervix cancer measured by dynamic contrast-enhanced MRI and CT. *Magn Reson Med* 2010;63:1601-1609.
- [106] Bains, LJ, McGrath, DM, Naish, JH, et al. Tracer kinetic analysis of dynamic contrast-enhanced MRI and CT bladder cancer data: A preliminary comparison to assess the magnitude of water exchange effects. *Magn Reson Med* 2010;64:595-603.
- [107] El-Sharkawy, AM, Schär, M, Bottomley, PA, Atalar, E. Monitoring and correcting spatio-temporal variations of the MR scanner's static magnetic field. *MAGMA* 2006;19:223-236.
- [108] Ocak, I, Bernardo, M, Metzger, G, et al. Dynamic contrast-enhanced MRI of prostate cancer at 3 T: a study of pharmacokinetic parameters. *AJR Am J Roentgenol* 2007;189:849.
- [109] Zhang, J, Rusinek, H, Bokacheva, L, Chen, Q, Storey, P, Lee, V. Use of cardiac output to improve measurement of input function in quantitative dynamic contrast-enhanced MRI. *J Magn Reson Imaging* 2009;30:656-665.
- [110] Cheng, HL. T₁ measurement of flowing blood and arterial input function determination for quantitative 3D T₁-weighted DCE-MRI. *J Magn Reson Imaging* 2007;25:1073-1078.
- [111] Smitsmans, MHP, Wolthaus, JWH, Artignan, X, et al. Automatic localization of the prostate for on-line or off-line image-guided radiotherapy. *Int J Radiat Oncol Biol Phys* 2004;60:623-635.
- [112] Kerkhof, EM, van der Put, RW, Raaymakers, BW, van der Heide, UA, van Vulpen, M, Lagendijk, JJW. Variation in target and rectum dose due to prostate deformation: an assessment by repeated MR imaging and treatment planning. *Phys Med Biol* 2008;53:5623-5634.
- [113] Lawrence, C, Zhou, JL, Tits, AL. User's Guide for CFSQP Version 2.5: A C Code for solving (Large Scale) Constrained Nonlinear (Minimax) Optimization Problems, Generating Iterates Satisfying All Inequality Constraints. Institute for Systems Research, University of Maryland, Technical Report TR-94-1611, College Park, MD 20742. 1997.
- [114] Franiel, T, Lüdemann, L, Rudolph, B, et al. Evaluation of normal prostate tissue, chronic prostatitis, and prostate cancer by quantitative perfusion analysis using a dynamic contrast-enhanced inversion-prepared dual-contrast gradient echo sequence. *Invest Radiol*. 2008;43:481-487.

- [115] Goh, V, Halligan, S, Hugill, J-A, Bartram, CI. Quantitative assessment of tissue perfusion using MDCT: comparison of colorectal cancer and skeletal muscle measurement reproducibility. *AJR Am J Roentgenol* 2006;187:164-169.
- [116] Bisdas, S, Surlan-Popovic, K, Didanovic, V, Vogl, T. Functional CT of squamous cell carcinoma in the head and neck: repeatability of tumor and muscle quantitative measurements, inter- and intra-observer agreement. *Eur Radiol* 2008;18:2241-2250.
- [117] Roberts, C, Issa, B, Stone, A, Jackson, A, Waterton, JC, Parker, GJM. Comparative study into the robustness of compartmental modeling and model-free analysis in DCE-MRI studies. *J Magn Reson Imaging* 2006;23:554-563.
- [118] Kershaw, LE, Hutchinson, CE, Allen, PD, Buckley, DL. Functional Imaging of the Prostate: Quantitative DCE-MRI and its Repeatability [abstract]. *Proceedings International Society for Magnetic Resonance in Medicine*. 2007;795.
- [119] Lankester, KJ, Taylor, JN, Stirling, JJ, et al. Dynamic MRI for imaging tumor microvasculature: comparison of susceptibility and relaxivity techniques in pelvic tumors. *J Magn Reson Imaging* 2007;25:796-805.
- [120] Alonzi, R, Taylor, J, Hoskin, P, et al. Reproducibility of quantitative and semi-quantitative dynamic and intrinsic susceptibility-weighted parameters of the cancerous human prostate gland [abstract]. *Proceedings International Society for Magnetic Resonance in Medicine*. 2008;164.
- [121] St. Lawrence, K, Lee, T. An Adiabatic Approximation to the Tissue Homogeneity Model for Water Exchange in the Brain: I. Theoretical Derivation. *J. Cereb. Blood Flow & Metab.* 1998;18:1365-1377.
- [122] Cheng, HLM. Investigation and optimization of parameter accuracy in dynamic contrast-enhanced MRI. *J Magn Reson Imaging* 2008;28:736-743.
- [123] Lopata, RGP, Backes, WH, Van den Bosch, PPJ, Van Riel, NAW. On the identifiability of pharmacokinetic parameters in dynamic contrast-enhanced imaging. *Magn Reson Med* 2007;58:425-429.
- [124] Kim, SM, Cho, YB, Haider, MA, Milosevic, M, Yeung, IWT. Multiphasic contrast injection for improved precision of parameter estimates in functional CT. *Med Phys* 2008;35:5921-5933.
- [125] Kozlowski, P, Chang, SD, Meng, R, et al. Combined prostate diffusion tensor imaging and dynamic contrast enhanced MRI at 3T--quantitative correlation with biopsy. *Magn Reson Imaging* 2010;28:621-628.
- [126] Kershaw, LE, Buckley, DL. Precision in measurements of perfusion and microvascular permeability with T1-weighted dynamic contrast-enhanced MRI. *Magn Reson Med* 2006;56:986-992.
- [127] Buckley, DL. Uncertainty in the analysis of tracer kinetics using dynamic contrast-enhanced T1-weighted MRI. *Magn Reson Med* 2002;47:601-606.
- [128] Naish, JH, Kershaw, LE, Buckley, DL, Jackson, A, Waterton, JC, Parker, GJM. Modeling of contrast agent kinetics in the lung using T1-weighted dynamic contrast-enhanced MRI. *Magn Reson Med* 2009;61:1507-1514.
- [129] Donaldson, SB, West, CML, Davidson, SE, et al. A comparison of tracer kinetic models for T1-weighted dynamic contrast-enhanced MRI: application in carcinoma of the cervix. *Magn Reson Med* 2010;63:691-700.
- [130] Henderson, E, Sykes, J, Drost, D, Weinmann, HJ, Rutt, BK, Lee, TY. Simultaneous MRI measurement of blood flow, blood volume, and capillary permeability in mammary tumors using two different contrast agents. *J Magn Reson Imaging* 2000;12:991-1003.
- [131] Brix, G, Zwick, S, Kiessling, F, Griebel, J. Pharmacokinetic analysis of tissue microcirculation using nested models: multimodel inference and parameter identifiability. *Med Phys* 2009;36:2923-2933.

- [132] Burnham, KP, Anderson, DR. Information and Likelihood Theory: A Basis for Model Selection and Inference. In: Burnham KP, Anderson DR, editors. Model selection and multimodel inference - A practical information-theoretic approach - Second edition, New York, USA: Springer Science+ Business Media. 2002.
- [133] Sourbron, SP, Buckley, DL. On the scope and interpretation of the Tofts models for DCE-MRI. *Magn Reson Med* 2011; in press, DOI 10.1002/mrm.22861.
- [134] Stewart, GD, Ross, JA, McLaren, DB, Parker, CC, Habib, FK, Riddick, ACP. The relevance of a hypoxic tumour microenvironment in prostate cancer. *BJU Int* 2010;105:8-13.
- [135] Kershaw, LE, Cheng, H-LM. Temporal resolution and SNR requirements for accurate DCE-MRI data analysis using the AATH model. *Magn Reson Med* 2010;64:1772-1780.
- [136] Murase, K. Efficient method for calculating kinetic parameters using T1-weighted dynamic contrast-enhanced magnetic resonance imaging. *Magn Reson Med* 2004;51:858-862.
- [137] Garpebring, A, Ostlund, N, Karlsson, M. A novel estimation method for physiological parameters in dynamic contrast-enhanced MRI: application of a distributed parameter model using Fourier-domain calculations. *IEEE Trans Med Imaging* 2009;28:1375-1383.
- [138] Hara, N, Okuizumi, M, Kawaguchi, M, Bilim, V. Dynamic contrast-enhanced magnetic resonance imaging (DCE-MRI) is a useful modality for the precise detection and staging of early prostate cancer. *Prostate* 2005;62:140-147.
- [139] Ito, H, Kamoi, K, Yokoyama, K, Yamada, K, Nishimura, T. Visualization of prostate cancer using dynamic contrast-enhanced MRI: comparison with transrectal power Doppler ultrasound. *Br J Radiol* 2003;76:617-624.
- [140] Kim, C, Park, B, Kim, B. Localization of prostate cancer using 3T MRI: comparison of T2-weighted and dynamic contrast-enhanced imaging. *J Comput Assist Tomogr* 2006;30:7-11.
- [141] van Vulpen, M, van den Berg, C, Moman, M, van der Heide, U. Difficulties and potential of correlating local recurrences in prostate cancer with the delivered local dose. *Radiother Oncol* 2009;93:180-184.
- [142] Harvey, C, Blomley, M, Dawson, P, et al. Functional CT imaging of the acute hyperemic response to radiation therapy of the prostate gland: early experience. *J Comput Assist Tomogr* 2001;25:43-49.
- [143] Win, Z, Ariff, B, Harvey, C, et al. Comparative study of experienced vs non-experienced radiologists in assessing parametric CT images of the response of the prostate gland to radiotherapy. *Br J Radiol* 2008;81:572-576.
- [144] Klein, S, Staring, M, Murphy, K, Viergever, M, Pluim, J. Elastix: a toolbox for intensity-based medical image registration. *IEEE Trans. Med. Imaging* 2010;29:196-205.
- [145] Lawrence, C, Zhou, JL, Tits, AL. User's Guide for CFSQP Version 2.5: A C Code for solving (Large Scale) Constrained Nonlinear (Minimax) Optimization Problems, Generating Iterates Satisfying All Inequality Constraints. 1997.
- [146] Padhani, AR, Gapinski, CJ, Macvicar, DA, et al. Dynamic contrast enhanced MRI of prostate cancer: correlation with morphology and tumour stage, histological grade and PSA. *Clin Radiol* 2000;55:99-109.
- [147] Pinkawa, M, Attieh, C, Piroth, M, et al. Dose-escalation using intensity-modulated radiotherapy for prostate cancer - Evaluation of the dose distribution with and without 18F-choline PET-CT detected simultaneous boost. *Radiother Oncol* 2009;93:213-219.
- [148] Al-Mamgani, A, van Putten, WL, Heemsbergen, WD, et al. Update of Dutch multicenter dose-escalation trial of radiotherapy for localized prostate cancer. *Int J Radiat Oncol Biol Phys* 2008;72:980-988.
- [149] Haie-Meder, C, Pötter, R, Van Limbergen, E, et al. Recommendations from Gynaecological (GYN) GEC-ESTRO Working Group (I): concepts and terms in 3D image based 3D treatment planning in cervix cancer brachytherapy with emphasis on MRI assessment of GTV and CTV. *Radiother Oncol* 2005;74:235-245.

- [150] Pötter, R, Haic-Meder, C, van Limbergen, E, et al. Recommendations from gynaecological (GYN) GEC ESTRO working group (II): Concepts and terms in 3D image-based treatment planning in cervix cancer brachytherapy - 3D dose volume parameters and aspects of 3D image-based anatomy, radiation physics, radiobiology. *Radiother Oncol* 2006;78:67-77.
- [151] Bentzen, SM. Theragnostic imaging for radiation oncology: dose-painting by numbers. *Lancet Oncol* 2005;6:112-117.
- [152] Vos, PC, Hambroek, T, Hulsbergen-van de Kaa, CA, Futterer, JJ, Barentsz, JO, Huisman, HJ. Computerized analysis of prostate lesions in the peripheral zone using dynamic contrast enhanced MRI. *Med Phys* 2008;35:888-899.
- [153] Van der Heide, UA, Korporaal, JG, Groenendaal, G, Franken, S, Van Vulpen, M. Functional MRI for tumor delineation in prostate radiation therapy. *Imaging Med.* 2011;3:219-231.
- [154] Smith, SW. *The Scientist and Engineer's Guide to Digital Signal Processing*. 2nd Edition, San Diego, CA: California Technical Publishing. 1999;434.
- [155] Groenendaal, G, Moman, MR, Korporaal, JG, et al. Validation of functional imaging with pathology for tumor delineation in the prostate. *Radiother Oncol* 2010;94:145-150.
- [156] Groenendaal, G, van den Berg, CA, Korporaal, JG, et al. Simultaneous MRI diffusion and perfusion imaging for tumor delineation in prostate cancer patients. *Radiother Oncol* 2010;95:185-190.
- [157] Bonvento, MJ, Moore, WH, Button, TM, Weinmann, H-J, Yakupov, R, Dilmanian, FA. CT angiography with gadolinium-based contrast media. *Acad Radiol* 2006;13:979-985.
- [158] Kuo, PH, Kanal, E, Abu-Alfa, AK, Cowper, SE. Gadolinium-based MR contrast agents and nephrogenic systemic fibrosis. *Radiology* 2007;242:647-649.
- [159] FDA. U.S. Food and Drug Administration. FDA Drug Safety Communication: New warnings for using gadolinium-based contrast agents in patients with kidney dysfunction [online] Available at: <<http://www.fda.gov/Drugs/DrugSafety/ucm223966.htm>> [Accessed 4 April 2011].
- [160] Weinreb, JC. Which study when? Is gadolinium-enhanced MR imaging safer than iodine-enhanced CT? *Radiology* 2008;249:3-8.
- [161] Halvorsen, RA. Which study when? Iodinated contrast-enhanced CT versus gadolinium-enhanced MR imaging. *Radiology* 2008;249:9-15.
- [162] Balvay, D, Kachenoura, N, Espinoza, S, et al. Signal-to-noise ratio improvement in dynamic contrast-enhanced CT and MR imaging with automated principal component analysis filtering. *Radiology* 2011;258:435-445.
- [163] Mendrik, AM, Vonken, EPA, Dankbaar, J-W, Prokop, M, Van Ginneken, B. Noise filtering in thin-slice 4D cerebral CT perfusion scans; abstract nr. 1619. *SPIE Medical Imaging*. 2010.
- [164] Dickinson, L, Ahmed, HU, Allen, C, et al. Magnetic resonance imaging for the detection, localisation, and characterisation of prostate cancer: recommendations from a European consensus meeting. *Eur Urol* 2011;59:477-494.

9

Chapter 9

Summary
Samenvatting
Zusammenfassung

9.1 Summary

Dynamic contrast-enhanced (DCE) MR imaging is frequently used for the detection and localization of prostate tumors. After injection of a bolus of contrast agent into the blood circulation, the behavior of the contrast agent in the prostate can be measured by repetitive imaging of the prostate. Prostate tumors are characterized by abnormalities in the blood flow and vessel permeability, which are reflected in abnormal behavior of the contrast agent. In a radiation treatment setting, accurate quantification of DCE data is needed, to allow for robust tumor delineation, tumor characterization and longitudinal studies.

For the quantification of DCE data with a tracer kinetic model, the measurement of an arterial input function (AIF) is required. However, measuring an AIF directly from the DCE-MRI magnitude signal can be challenging. To prevent large errors in an exam-specific AIF, the use of a population-averaged AIF has been proposed for analysis of DCE-MRI data of the prostate. For a well-founded choice between the two, on the one hand information is required about the inter- and intra-patient variations that are neglected with the use of a population-averaged AIF. On the other hand, the reliability of measuring an exam-specific AIF must be established. To avoid the difficulties with measuring an AIF from the MR magnitude signal, we analyzed in Chapter 2 the AIFs from a DCE-CT repeatability study, to assess the variations in the AIF between patients, between exams, between the left and right femoral arteries and between slices. We found that for longitudinal and multi-center studies of quantitative DCE-MRI, the use of a population-averaged AIF is advantageous when the measurement precision of an exam-specific AIF is considerably worse than 15%.

As an alternative to the magnitude signal, the AIF can also be measured from the DCE-MRI phase signal (AIF_{PHASE}). Although some phantom and simulation studies have been performed, validation of AIF_{PHASE} measurements is lacking. We compared in Chapter 3 AIF_{PHASE} measurements with the AIF as measured on CT (AIF_{CT}) and calculated the corresponding K^{trans} maps in 12 prostate cancer patients. The shape of AIF_{PHASE} and AIF_{CT} are similar, although small differences in the peak height and peak width exist as a result of differences in injection protocol. No significant differences in K^{trans} values were found between the DCE-MRI and DCE-CT exams. Therefore, robust quantification of K^{trans} values from DCE-MRI exams in the cancerous prostate is feasible with the use of AIF_{PHASE} .

For reliable identification of small lesions within the prostate, it is crucial that they are consistently detected when the examination and analysis are repeated. The smallest detectable lesion size, however, depends on the spatial resolution. Therefore, we evaluated in Chapter 4 the relationship between image noise, voxel size, and voxel-wise repeatability of DCE-CT examinations for prostate cancer. We found that there is a high voxel-wise repeatability of the DCE-CT imaging technique for kernel sizes as small as 0.1 cm^3 . With the relationship between kernel size, image noise and voxel-wise repeatability, it becomes possible to estimate for alternative DCE-CT

protocols, e.g. those with a reduced radiation dose, at what kernel size a sufficient repeatability can be obtained.

A number of different TKMs, with varying degrees of complexity, have been clinically used to quantify the microvascular properties of the prostate. The three most commonly used TKMs for quantification of DCE data from the prostate are the Tofts, extended Tofts, and adiabatic approximation to the tissue homogeneity (AATH) model. In Chapter 5 we investigated which of these three TKMs is the optimal model for quantification of DCE-CT data, under what conditions and how large the differences between the models are. The best model was determined for each voxel, based on the corrected Akaike's Information Criterion (AICC), taking into account both the goodness-of-fit and the number of model parameters. The three models all give reasonable fits of DCE-CT data from prostate and differences are small. In view of the small parameter range in which the Tofts and extended Tofts model outperform the AATH model, the latter seems the optimal model for quantification of DCE-CT data of the prostate.

Delineating a prostate tumor essentially comes down to a voxelwise decision whether a voxel contains tumor or not. There are however two problems that make an accurate tumor delineation difficult. First, the sensitivity and specificity of the DCE technique are not perfect. Second, by definition no detailed spatial verification of imaging with pathology can be obtained from patients scheduled for radiation therapy. In the clinical practice of radiotherapy treatment planning this means that there will never be a ground truth when delineating a prostate tumor. In Chapter 6 we propose a method to incorporate the uncertainty that a voxel contains tumor into the tumor delineation process. We converted K^{trans} maps into probabilities for the presence of tumor and translated this probabilistic information into GTV and CTV concepts, which are commonly used in radiotherapy treatment planning. In this way, the intrinsic uncertainty that a voxel contains tumor can be incorporated into the treatment planning process.

In conclusion, a number of studies have been performed to facilitate well-founded decision making in the quantification process of DCE-MRI and DCE-CT exams for tumor delineation in prostate cancer.

9.2 Samenvatting

Dynamische contrastmiddel-versterkte (DCE) MRI is een veelgebruikte techniek om prostaatumoren te detecteren en lokaliseren. Na injectie van een contrastmiddel in de bloedbaan wordt de prostaat herhaaldelijk afgebeeld, om het gedrag van dit contrastmiddel in de prostaat te kunnen meten. Prostaatumoren kenmerken zich door afwijkingen in de bloedstroom en permeabiliteit van de bloedvaten, die weerspiegeld worden in afwijkend gedrag van het contrastmiddel. Een nauwkeurige kwantificering van DCE data is vereist voor toepassing binnen de radiotherapie, om robuuste tumorintekening, tumorkarakterisering en het beschrijven van weefselveranderingen in de loop van de tijd mogelijk te maken.

Voor het kwantificeren van DCE data met een zogenaamd pharmacokinetisch model (PKM) is het meten van een arteriële input functie (AIF) vereist. Een directe AIF-meting uit het DCE-MRI magnitude signaal kan echter moeilijk zijn. Om grote afwijkingen in een meting-specifieke AIF te vermijden, heeft men voorgesteld een populatie-gemiddelde AIF te gebruiken voor de kwantificering van DCE-MRI metingen in de prostaat. Om een weloverwogen keuze te kunnen maken tussen deze beide AIFs, is enerzijds informatie nodig over de inter- en intra-patiënt variaties die worden genegeerd met een populatie-gemiddelde AIF. Anderzijds moet de betrouwbaarheid van het bepalen van een meting-specifieke AIF worden vastgesteld. Om de moeilijkheden bij het bepalen van een AIF uit het MRI magnitude signaal te vermijden, analyseren we in Hoofdstuk 2 de AIFs uit een DCE-CT reproduceerbaarheidsstudie om de fysiologische variaties in de AIF tussen patiënten, tussen metingen, tussen de linker en rechter femoraalarteriën en tussen plakken vast te kunnen stellen. Voor longitudinale en multi-center studies van kwantitatieve DCE-MRI blijkt het gebruik van een populatie-gemiddelde AIF van voordeel te zijn als de meetnauwkeurigheid van een meting-specifieke AIF aanzienlijk slechter is dan 15%.

Als een alternatief voor het magnitude signaal kan de AIF ook gemeten worden uit het DCE-MRI fase signaal (AIF_{FASE}). Alhoewel er een aantal fantoom- en simulatiestudies zijn uitgevoerd, is er een gebrek aan validatie van AIF_{FASE} metingen in patiënten. In Hoofdstuk 3 vergelijken we AIF_{FASE} metingen met de AIFs gemeten op CT (AIF_{CT}), evenals de bijbehorende K^{trans} beelden. De algehele vorm van AIF_{FASE} en AIF_{CT} toont sterke overeenkomsten, maar kleine verschillen in de piekhoogte en piekbreedte zijn aanwezig als gevolg van verschillen in injectieprotocol. Geen significante verschillen zijn gevonden in de K^{trans} waarden tussen DCE-MRI en DCE-CT. Bij DCE-MRI in prostaatkankerpatiënten is een robuuste kwantificering van K^{trans} waarden dus mogelijk met het gebruik van AIF_{FASE} .

Voor een betrouwbare identificatie van kleine tumorlaesies in de prostaat is het cruciaal dat deze consistent worden gedetecteerd als de DCE-meting en analyse worden herhaald. De kleinst detecteerbare laesiegrootte hangt echter af van de spatiële resolutie. Daarom is in Hoofdstuk 4 de samenhang tussen beeldruis, voxelgrootte en reproduceerbaarheid per voxel onderzocht voor DCE-CT metingen van de prostaat. Er blijkt een goede reproduceerbaarheid per voxel te zijn tot een

minimale voxelgrootte van 0.1 cm^3 . Met het vaststellen van deze samenhang tussen beeldruis, voxelgrootte en reproduceerbaarheid per voxel is het mogelijk geworden om voor andere DCE-CT protocollen, met bijvoorbeeld een lagere stralingsdosis, te bepalen bij welke voxelgrootte een voldoende hoge reproduceerbaarheid kan worden behaald.

Een aantal verschillende PKMS, met variërende complexiteit, zijn in klinisch gebruik om de bloedstroom en permeabiliteit van de bloedvaatjes in de prostaat te kwantificeren. De drie meest gebruikte PKMS bij DCE metingen van de prostaat zijn het Tofts, extended Tofts en AATH model. In Hoofdstuk 5 is onderzocht welke van deze drie modellen het optimale model is voor de kwantificering van DCE-CT metingen van de prostaat, onder welke omstandigheden en hoe groot de verschillen tussen de modellen zijn. Per voxel werd het beste model bepaald door middel van het gecorrigeerde Akaike's Informatie Criterium (AICC), dat rekening houdt met zowel de fitkwaliteit als ook het aantal modelparameters. De drie modellen geven allemaal acceptabele fits van DCE-CT data in de prostaat en de verschillen tussen de modellen zijn klein. Gezien het kleine parameter bereik waarin het Tofts en extended Tofts model het AATH model overtreffen, lijkt laatstgenoemde het optimale model voor kwantificering van DCE-CT data van de prostaat.

Het intekenen van een prostaattumor komt in essentie neer op een voxelgewijze beslissing of een voxel tumor bevat of niet. Er zijn echter twee problemen die een nauwkeurige tumorintekening bemoeilijken. De sensitiviteit en specificiteit van de DCE methode zijn niet perfect en er kan per definitie geen gedetailleerde pathologische validatie plaatsvinden van patiënten die radiotherapie ondergaan. Voor de klinische praktijk van de radiotherapieplanning betekent dit dat er nooit een 'ground truth' zal zijn voor tumorintekening in de prostaat. In Hoofdstuk 6 beschrijven we een methode die de onzekerheid dat een voxel tumor bevat meeneemt in de tumorintekening. K^{trans} beelden zijn per voxel omgerekend naar waarschijnlijkheden voor de aanwezigheid van tumorweefsel en vervolgens vertaald naar GTV- en CTV-concepten, die in algemeen gebruik zijn bij de radiotherapieplanning. Op deze manier kan de intrinsieke onzekerheid dat een voxel tumor bevat meegenomen worden in het proces van radiotherapieplanning.

Concluderend is een aantal studies uitgevoerd om weloverwogen keuzes mogelijk te maken bij de kwantificering van DCE-MRI en DCE-CT metingen voor tumorintekening bij prostaatkanker.

9.3 Zusammenfassung

Dynamische kontrastmittelgestützte (DCE) Magnetresonanztomografie (MRT) wird häufig angewendet für den Nachweis und die Lokalisierung von Prostatakarzinomen. Nach Gabe eines Kontrastmittels in den Blutkreislauf kann das Verhalten des Kontrastmittels in der Prostata durch wiederholte Bildgebung der Prostata gemessen werden. Kennzeichnend für Prostatakarzinomen sind Abweichungen im Blutfluss und in der Gefäßpermeabilität, die in einem abweichenden Verhalten des Kontrastmittels reflektiert werden. Eine genaue Quantifizierung von DCE-Daten ist für die Anwendung innerhalb der Strahlentherapie notwendig, um robuste Tumoreinzeichnung, Tumorcharakterisierung sowie das Beschreiben von Gewebeveränderungen im Laufe der Zeit zu ermöglichen.

Zur Quantifizierung von DCE-Daten mit einem sogenannten pharmakokinetischen Modell (PKM) ist die Messung einer arteriellen Inputfunktion (AIF) notwendig. Jedoch kann die Messung der AIF direkt aus dem DCE-MRT-Amplitudensignal eine Herausforderung sein. Um große Fehler in einer untersuchungsspezifischen AIF vorzubeugen, hat man vorgeschlagen, eine populationsdurchschnittliche AIF für DCE-MRT-Analyse der Prostata zu verwenden. Für eine begründete Wahl zwischen beiden AIFs sind einerseits Kenntnisse über Inter- und Intrapatientvariationen gefragt, die in einer populationsdurchschnittlichen AIF vernachlässigt werden. Andererseits sollte die Zuverlässigkeit einer untersuchungsspezifischen AIF-Messung festgestellt werden. Um die Schwierigkeiten beim Messen der AIF aus dem Amplitudensignal zu vermeiden, wurden in Kapitel 2 die AIFs einer DCE-CT- Wiederholbarkeitsstudie analysiert, um AIF-Variationen zwischen Patienten, zwischen Untersuchungen, zwischen den linken und rechten Femoralarterien und zwischen Schichten festzustellen. Für Längsschnitt- und multizentrischen Studien von quantitativer DCE-MRT erwies sich die Verwendung einer populationsdurchschnittlichen AIF als vorteilhaft, wenn die Messgenauigkeit einer untersuchungsspezifischen AIF wesentlich schlechter als 15% ist.

Als Alternative zum Amplitudensignal kann die AIF auch aus dem DCE-MRT-Phasensignal (AIF_{PHASE}) gemessen werden. Obwohl einige Phantom- und Simulationsstudien durchgeführt worden sind, mangelt es an Validierung der AIF_{PHASE} -Messungen. In Kapitel 3 wurden AIF_{PHASE} -Messungen mit AIFs von DCE-CT-Untersuchungen (AIF_{CT}) verglichen und sind die entsprechenden K^{trans} -Bilder in 12 Prostatakarzinompatienten ausgerechnet worden. Die Form der AIF_{PHASE} und AIF_{CT} ist ähnlich, obwohl es kleine Unterschiede in der Spitzenhöhe und Spitzenbreite gibt als Folge von Unterschieden in Injektionsprotokollen. Zwischen den DCE-MRT- und DCE-CT-Untersuchungen wurden keine signifikanten Unterschiede in K^{trans} -Werten gefunden. Folglich ist eine robuste Quantifizierung von K^{trans} -Werten von DCE-MRT-Untersuchungen der krebsartigen Prostata durch die Verwendung von AIF_{PHASE} möglich.

Für zuverlässige Identifizierung von kleinen Läsionen innerhalb der Prostata ist es entscheidend, dass sie konsequent festgestellt werden, wenn die Untersuchung und

die Analyse wiederholt werden. Die kleinst nachweisbare Läsionsgröße hängt aber von der Bildauflösung ab. Deswegen wurden in Kapitel 4 die Zusammenhänge zwischen Bildrauschen, Voxelgröße und voxelweise Wiederholbarkeit von DCE-CT-Untersuchungen der krebsartigen Prostata evaluiert. Es stellte sich heraus, dass es eine hohe voxelweise Wiederholbarkeit der DCE-CT-bildgebenden Technik gibt bis zu einer minimalen Voxelgröße von 0.1 cm^3 . Mit der Feststellung des Zusammenhangs zwischen Bildrauschen, Voxelgröße und voxelweise Wiederholbarkeit ist es möglich geworden, um für alternative DCE-CT-Protokolle, wie zum Beispiel mit einer niedrigeren Strahlendosis, festzustellen, bei welcher Voxelgröße eine ausreichend hohe Wiederholbarkeit erreicht werden kann.

Eine Anzahl verschiedener PKMs, mit unterschiedlicher Komplexität, werden klinisch verwendet, um die mikrovaskulären Eigenschaften der Prostata zu quantifizieren. Die drei meist verwendeten PKMs zur Quantifizierung von DCE-Daten der Prostata sind das Tofts-, extended Tofts- und AATH-Modell. Kapitel 5 handelt darüber, welches von diesen drei Modellen unter welchen Verhältnissen das optimale Modell zur Quantifizierung von DCE-CT Daten ist, und wie groß die Unterschiede zwischen den Modellen sind. Das beste Modell wurde für jedes Voxel, mittels des korrigierten Akaike-Informationskriteriums (AICc) festgestellt, wobei sowohl die Anpassungsgüte als die Anzahl der Modellparameter berücksichtigt werden. Die drei Modelle geben alle ordentlichen Ergebnisse von DCE-CT-Daten der Prostata, und die Unterschiede sind klein. Angesichts des kleinen Parameterbereichs, in dem das Tofts- und extended Tofts-Modell das AATH-Modell übertreffen, erscheint letztgenanntes das optimale Modell zur Quantifizierung von DCE-CT-Daten der Prostata zu sein.

Einzeichnung eines Prostatatumors kommt im Grunde genommen einer voxelweisen Entscheidung, ob ein Voxel Tumor enthält oder nicht, gleich. Es gibt aber zwei Probleme, die eine präzise Tumoreinzeichnung erschweren. Die Sensitivität und Spezifität sind nicht perfekt, und von Patienten, die Strahlentherapie bekommen werden, kann man grundsätzlich keine detaillierte räumliche Überprüfung der Pathologie erhalten. In der klinischen Praxis der Strahlentherapieplanung bedeutet das, dass es bei der Tumoreinzeichnung nie eine ‚ground truth‘ geben wird. In Kapitel 6 schlagen wir eine Methode vor, in der die Ungewissheit, ob ein Voxel Tumorgewebe enthält, in dem Einzeichnungsprozess berücksichtigt wird. Wir wandelten K^{trans} -Bilder in Wahrscheinlichkeiten für die Anwesenheit von Tumorgewebe um und übersetzten diese anschließend in CTV- und GTV-Konzepte, die in der Strahlentherapieplanung gewöhnlich verwendet werden. Auf diese Weise kann die immanente Ungewissheit, ob ein Voxel Tumorgewebe enthält, in das Strahlentherapieplanungsprozess integriert werden.

Dies alles zusammenfassend sind einige Studien ausgeführt worden, um bei der Quantifizierung von DCE-MRT- und DCE-CT-Untersuchungen zur Tumoreinzeichnung des Prostatakarzinoms begründete Entscheidungen treffen zu können.

10

Chapter 10

List of publications

10.1 Scientific articles

Validation of functional imaging with pathology for tumor delineation in the prostate

G. Groenendaal, M.R. Moman, [J.G. Korporaal](#), P.J. van Diest, M. van Vulpen, M.E.P. Philippens, and U.A. van der Heide
Radiotherapy and Oncology 2010;94(2):145-50.

The use of probability maps to deal with the uncertainties in prostate cancer delineation

[J.G. Korporaal](#), C.A.T. van den Berg, G. Groenendaal, M.R. Moman, M. van Vulpen, and U.A. van der Heide
Radiotherapy and Oncology 2010;94(2):168-72.

Simultaneous MRI diffusion and perfusion imaging for tumor delineation in prostate cancer patients

G. Groenendaal, C.A.T. van den Berg, [J.G. Korporaal](#), M.E.P. Philippens, P. Luijten, M. van Vulpen, and U.A. van der Heide
Radiotherapy and Oncology 2010;95(2):185-90.

Dynamic contrast-enhanced CT for prostate cancer: relationship between image noise, voxel size, and repeatability

[J.G. Korporaal](#), C.A.T. van den Berg, C.R.L.P.N. Jeukens, G. Groenendaal, M.R. Moman, P. Luijten, M. van Vulpen, and U.A. van der Heide
Radiology 2010;256(3):976-84.

Functional MRI for tumor delineation in prostate radiation therapy

U.A. van der Heide, [J.G. Korporaal](#), G. Groenendaal, S. Franken, and M. van Vulpen
Imaging in Medicine 2011;3(2):219-231.

Phase-based arterial input function measurements in the femoral arteries for quantification of dynamic contrast-enhanced (DCE) MRI and comparison with DCE-CT

[J.G. Korporaal](#), C.A.T. van den Berg, M.J.P. van Osch, G. Groenendaal, M. van Vulpen, and U.A. van der Heide
Magnetic Resonance in Medicine 2011; in press: DOI 10.1002/mrm.22905.

Tracer kinetic model selection for dynamic contrast-enhanced computed tomography imaging of prostate cancer

[J.G. Korporaal](#), M. van Vulpen, C.A.T. van den Berg, and U.A. van der Heide
Investigative Radiology 2011; in press: DOI 10.1097/RLI.0b013e31821c0ea7.

Uncertainties in the arterial input function (AIF) in dynamic contrast-enhanced (DCE) imaging of the pelvis: when to use a population-averaged or an exam-specific AIF?

[J.G. Korporaal](#), C.A.T. van den Berg, M.J.P. van Osch, M. van Vulpen, and U.A. van der Heide
Physics in Medicine and Biology 2011; submitted.

The effect of hormonal treatment on conspicuity of prostate cancer: implications for focal boosting radiotherapy

G. Groenendaal, M. van Vulpen, S.R. Pereboom, D. Poelma-Tap, [J.G. Korporaal](#), E. Monninkhof, and U.A. van der Heide
Radiotherapy and Oncology 2011; submitted.

10.2 Proceedings and abstracts

Differences between DCE-MR and DCE-CT in prostate cancer and their implications on the choice of a tracer kinetic model – [poster]

J.G. Korporaal, C.A.T. van den Berg, C.R.L.P.N. Jeukens, G. Groenendaal, M. van Vulpen, P. Luijten, and U.A. van der Heide

First Benelux In Vivo MR Methods Symposium, December 12, 2007, Berg en Dal, The Netherlands

Differences between DCE-MR and DCE-CT in prostate cancer and their implications on the choice of a tracer kinetic model – [poster]

J.G. Korporaal, C.A.T. van den Berg, C.R.L.P.N. Jeukens, G. Groenendaal, M. van Vulpen, P. Luijten, and U.A. van der Heide

ISMRM 16th Annual Scientific Meeting & Exhibition, May 3–9, 2008, Toronto, Canada

Delineation for tumor boosting in prostate cancer based on dynamic contrast-enhanced CT – [poster]

J.G. Korporaal, C.R.L.P.N. Jeukens, C.A.T. van den Berg, G. Groenendaal, M. van Vulpen, and U.A. van der Heide

ESTRO27, September 14–18, 2008, Göteborg, Sweden

Tumor delineation with a probability function based on dynamic contrast-enhanced CT – [oral]

J.G. Korporaal, C.A.T. van den Berg, G. Groenendaal, M.R. Moman, M. van Vulpen, and U.A. van der Heide

10th Biennial ESTRO, August 30 – September 3, 2009, Maastricht, The Netherlands

Validation with DCE-CT proves that the DCE-MRI phase signal can be used for robust measurement of the arterial input function (AIF) in the iliac arteries – [oral]

J.G. Korporaal, C.A.T. van den Berg, M.J.P. van Osch, G. Groenendaal, M. van Vulpen, and U.A. van der Heide

Third Annual Meeting of the ISMRM Benelux Chapter, January 19, 2011, Hoeven, The Netherlands

Improving the robustness of quantitative dynamic contrast-enhanced MRI for tumor delineation in prostate cancer – [oral]

J.G. Korporaal, C.A.T. van den Berg, M.J.P. van Osch, G. Groenendaal, M. van Vulpen, and U.A. van der Heide

11th Biennial ESTRO, May 8–12, 2011, London, United Kingdom

Validation with DCE-CT proves that the DCE-MRI phase signal can be used for robust measurement of the arterial input function (AIF) in the iliac arteries – [oral]

J.G. Korporaal, C.A.T. van den Berg, M.J.P. van Osch, G. Groenendaal, M. van Vulpen, and U.A. van der Heide

ISMRM 19th Annual Scientific Meeting & Exhibition, May 7–13, 2011, Montréal, Canada

11

Er staat slechts één naam op de voorkant van dit boekje, maar eigenlijk is dat niet terecht. Er zijn namelijk veel mensen die op een directe of indirecte manier, en misschien wel onbewust, een bijdrage hebben geleverd aan de totstandkoming van dit proefschrift. Laat ik in het UMC Utrecht beginnen.

Jan, het was me een waar genoegen om op ‘jouw’ afdeling Radiotherapie mijn promotieonderzoek uit te voeren. Ook al was je niet direct bij mijn onderzoek betrokken – de vragen die je tijdens de fysica-werkbesprekingen stelde, waren zonder uitzondering relevant. Daarnaast stond je deur altijd open voor allerhande vragen en voor de nodige ‘krabbels’ op declaraties. Je betrokkenheid bij en je steun aan de AiO-groep waren groot, wat ook blijkt uit jouw aansporingen om kamers te bezetten als we het ergens niet mee eens waren (‘net als vroeger’). Gelukkig (of misschien helaas) is het nooit zover gekomen. Hartelijk dank voor een zorgeloos promotietraject!

Uulke, vanaf dag één heb je als co-promotor en dagelijks begeleider een belangrijke en bepalende rol gespeeld bij mijn promotieonderzoek. In de eerste jaren heb jij de grote lijnen uitgezet en me leren focussen op het schrijven van wetenschappelijke publicaties. Dat ging niet zonder slag of stoot: regelmatig verdwaalde ik in zijpaden die niet ‘*on topic*’ waren en regelmatig hebben we manuscripten zitten herschrijven, en herschrijven, en herschrijven. Jouw geduld met mij was in dat opzicht bewonderenswaardig! Maar al deze moeite is gelukkig niet voor niets geweest en heeft uiteindelijk zijn vruchten afgeworpen, met als klinkend sluitstuk het laatste manuscript dat zich in vier weken ontwikkelde van niets tot ‘*submitted*’, en nog eens vier weken later geaccepteerd was. Je deur stond altijd voor me open, ook voor persoonlijke gesprekken. Dat heb ik als enorm prettig ervaren. Dankjewel voor vier onvergetelijke jaren!

Marco, zonder jou had mijn promotieonderzoek niet kunnen slagen. Je hebt voor een groot deel de patiënteninclusie van mijn onderzoeken voor je rekening genomen, waar ik zeer dankbaar voor ben. Ook was jouw aanwezigheid bij het wekelijkse prostaatoverleg van groot belang. Dankzij je kritische en terechte vragen over het klinische nut van de vaak technische en kleine details van de DCE-analyse waar ik mee bezig was, is de klinische relevantie van mijn onderzoek nooit uit het oog geraakt.

Nico, toen ik in 2007 op de afdeling begon, heb je me bekend gemaakt met de verschillende perfusiemodellen, met de fascinerende MRI-wereld en met de programmeeromgeving in C++. Heel veel dank voor deze ‘inwerkhulp’, je altijd kritische kijk naar mijn manuscripten en de prettige samenwerking de afgelopen jaren!

Thijs, met name het laatste jaar hebben we veel contact gehad over (fase-)AIFs. Jouw grote ervaring hiermee en jouw goede suggesties, ook voor de fantoom-experimenten, zijn zeer waardevol geweest!

Alexis, Gijs, Ric, Rob en Kees: dank voor alle pc- en programmeerhulp!

Ik heb het altijd een groot voorrecht gevonden om onderdeel te zijn van een grote en vooral gezellige **AiO-groep**. Niets is leuker, dan om tijdens koffiepauzes, AiO-uitjes, congressen en gewoon tijdens het werk te praten over de dagelijkse perikelen, de (zeldzame) hoogtepunten en de clichés (“*Free food!*”) die kenmerkend zijn voor het AiO-bestaan. **Alexander, Bob, Richard, Ellen, Michiel, Anette, Greetje, Catalina, Ilona, Joana, Astrid, Sjoerd, Mette, Özlem, Anna, Alessandro, Kimmy, Christel, Mariska en Frank**, jullie zijn geweldig!

Greetje, we zijn tegelijkertijd aan het grote avontuur dat ‘promoveren’ heet begonnen. In het begin was veel nog onduidelijk, maar langzamerhand zijn we elk ons eigen onderzoekstraject ingeslagen en hebben we al die jaren op een heel prettige manier samengewerkt, zonder elkaar voor de voeten te lopen. Ik kijk met ontzettend veel genoegen terug op de laatste periode, waarin we op dezelfde kamer zaten. Heel erg veel plezier en succes toegewenst in je verdere carrière als ‘Groenendaal *et al!*’

Anette, na bijna 10 jaar scheiden onze carrièrepaden. Toen ik je in september 2001 bij MNW leerde kennen kon ik niet bevroeden (en jij waarschijnlijk ook niet) dat we elkaar de daaropvolgende jaren bijna dagelijks zouden zien. Dankzij jouw mailtje over een AiO-vacature heb ik in Utrecht vier fantastische jaren gehad. Bedankt! Je was de afgelopen jaren een tóp-studiegenoot en -collega!

Tot slot wil ik **alle andere collega’s van de afdeling Radiotherapie** bedanken die op één of andere wijze hun medewerking aan mijn promotieonderzoek hebben verleend.

Ook buiten het UMC zijn veel mensen de afgelopen jaren bij mijn promotie betrokken geweest. Om te beginnen wil ik alle leden van **Muziekgezelschap De Harmonie Barneveld** bedanken voor de vele gezellige repetities, concerten, buitenoptredens, reizen en borrels de afgelopen vier jaar. Het was heerlijk om elke week muziek te kunnen maken en daarbij mijn hoofd ‘leeg’ te spelen.

Lisette en Marlous, fantastisch dat jullie mijn paranimfen willen zijn! We hebben de afgelopen jaren samen veel ‘producties’ gedaan: van klarinet-kwartet/-kwintet, tot advertenties en drukwerk. We zijn een top-team! Lisette, ‘Mokum, Laguh-Cee en Bass-Buddy’ - *need I say more?!* Thanx voor alle gezelligheid en serieuzigheid de afgelopen vier jaar! Marlous, keep up the good work: *Harmonia forever!*

Lisanne, tijdens de eerste jaren van mijn promotie ben jij mijn grote steun en toeverlaat geweest. Dankjewel - jij hebt je plekje in dit dankwoord meer dan verdiend!

Lieber Opa, liebe Oma! Ich bin unheimlich froh, dass ich auch in den letzten vier Jahren immer wieder nach Iggingen kommen konnte und mit offenen Armen empfangen wurde! Vielen Dank für die vielen Urlaubstage, die ich bei euch verbracht habe, um mich wieder ‚aufzuladen‘, um in Utrecht im Promotionsalltag wieder weitermachen zu können. Ich hoffe, dass wir zusammen noch oft Kaiserschmarrn essen werden!

Lieve Oma, jij mag in dit dankwoord ook niet ontbreken. Regelmatig vroeg je hoe de zaken er in Utrecht voor stonden en je was altijd geïnteresseerd in de dingen die ik tijdens congressen had meegemaakt. En met je leuke grappen en familie-updates heb je me veel zondagen wat afleiding gegeven om mijn werk even te vergeten! Super!

Piet en Annemieke, Paula en Twan: wat zijn jullie leuke stellen! Ik ben maar een geluksvogel met zulke lieve, leuke en grappige mensen om me heen! Jullie hebben me de afgelopen vier jaren regelmatig afleiding gegeven, niet in het minst tijdens de inmiddels traditionele sinterklaasviering en nieuwjaarsscrabble. Ik hoop dat we die evenementen nog lang in stand kunnen houden!

Papa en mama, tot slot mogen jullie uiteraard niet ontbreken. Jullie hebben aan mijn wieg, en daarmee aan de wieg van dit proefschrift gestaan. Ook de afgelopen vier jaar hebben jullie mij mijn eigen weg laten zoeken. Jullie onvoorwaardelijk steun was daarbij ontzettend waardevol. Dank jullie wel!

12



- EN** Johannes (Jan) Georg Korporaal (Ede, *1982) was raised in Barneveld, the Netherlands. In 2001 he graduated from pre-university secondary education at the Johannes Fontanus College in Barneveld and started his bachelor study Medical Natural Sciences at the Faculty of Sciences of the VU University Amsterdam. After finishing a scientific internship on electrical impedance tomography at the Dept. of Physics and Medical Technology of the VU University Medical Center (vumc), he started in 2004 the master track Medical Physics, with a minor specialization in Science Communication. In 2007 he obtained his msc degree after a scientific internship at the earlier mentioned department of the vumc on dynamic contrast-enhanced (DCE) MRI in patients with pulmonary hypertension. Directly after, he started his PhD research at the Dept. of Radiotherapy of the University Medical Center Utrecht on DCE-MRI and DCE-CT of prostate cancer, as described in this thesis. Since July 2011 he is working in Forchheim (Germany) for Siemens AG Healthcare Sector on Physics and Application Development Computed Tomography.
- NL** Johannes (Jan) Georg Korporaal (Ede, *1982) groeide op in Barneveld. In 2001 behaalde hij zijn vwo-diploma aan het Johannes Fontanus College te Barneveld en startte aan de Faculteit der Exacte Wetenschappen van de Vrije Universiteit te Amsterdam de bachelorstudie Medische Natuurwetenschappen. Na een afsluitend wetenschappelijk bachelorproject op het gebied van elektrische impedantietomografie op de afdeling Fysica en Medische Technologie van het vumc, begon hij in 2004 aan de mastertrack *Medical Physics* met een minor specialisatie in de Wetenschaps- en Techniekcommunicatie. In 2007 behaalde hij het msc-diploma na een wetenschappelijke afstudeerstage op eerdergenoemde afdeling van het vumc, op het gebied van *dynamic contrast-enhanced* (DCE) MRI in patiënten met pulmonale hypertensie. Direct aansluitend begon hij zijn promotieonderzoek op de afdeling Radiotherapie van het UMC Utrecht op het gebied van DCE-MRI en DCE-CT van prostaatanker, waarvan de resultaten staan beschreven in dit proefschrift. Sinds juli 2011 is hij in Forchheim (Duitsland) werkzaam bij Siemens AG Healthcare Sector op het gebied van Fysica en Toepassingsontwikkeling van Computer Tomografie.
- DE** Johannes (Jan) Georg Korporaal (Ede, *1982) wurde in Barneveld (Niederlande) erzogen. 2001 machte er das Abitur am Johannes Fontanus College in Barneveld und fing an der Fakultät der Naturwissenschaften der VU Universität in Amsterdam sein Bachelorstudium Medizinische Naturwissenschaften an. Nach einer wissenschaftlichen Bachelorabschlussarbeit im Bereich der elektrischen Impedanztomographie in der Abteilung Physik und Medizinische Technologie der VU Universitätsklinik (vumc), startete er 2004 das Masterprogramm Medizinische Physik mit einer Beifachspezialisierung in der Wissenschafts- und Technikkommunikation. 2007 erhielt er das msc-Diplom nach einer wissenschaftlichen Abschlussarbeit auf letztgenannter Abteilung des vumc, im Bereich der dynamischen kontrastmittelgestützten (DCE) MRT in Patienten mit pulmonaler Hypertension. Direkt anschließend fing er mit seinem Promotionsvorhaben in der Abteilung der Strahlenonkologie der Universitätsklinik Utrecht an, im Bereich der DCE-MRT und DCE-CT des Prostatakarzinoms, dessen Ergebnisse in dieser Doktorarbeit beschrieben worden sind. Seit Juli 2011 ist er in Forchheim (Deutschland) bei Siemens AG Healthcare Sector im Bereich der Physik und Applikationsentwicklung der Computertomografie beschäftigt.

Notes



A series of horizontal dotted lines for writing notes.

